Doctoral Dissertation
Doctoral Program in Materials Science and Technology (35th Cycle)

Graphene-based mixed matrix membranes for CO_2 separation.

By

Alberto Martis

******

Supervisor(s):
Prof. Fabrizio Pirri Supervisor
Prof. Sergio Bocchini Co-supervisor

Doctoral Examination Committee:
Prof. Alberto Frache, Referee , Politecnico di Torino
Prof. Annalisa Chiappone , Referee, Universita di Cagliari.
Prof. Iuliana Cota , Referee, Eurecat Centro Tecnológico de Cataluña
Prof. Samuele Porro, Referee, Politecnico di Torino
Prof. Mattia Bartoli, Referee, IIT Istituto Italiano Tecnologie

Politecnico di Torino
2023

Declaration

I hereby declare that the contents and organization of this dissertation constitute my own original work and do not compromise in any way the rights of third parties, including those relating to the security of personal data.

Alberto Martis

2023

* This dissertation is presented in partial fulfillment of the requirements for **Ph.D. degree** in the Graduate School of Politecnico di Torino (ScuDo).

So Long, and thanks for all the fish...

Douglas Adams

Ad Alessandro e Alberto.

Acknowledgment

Abstract

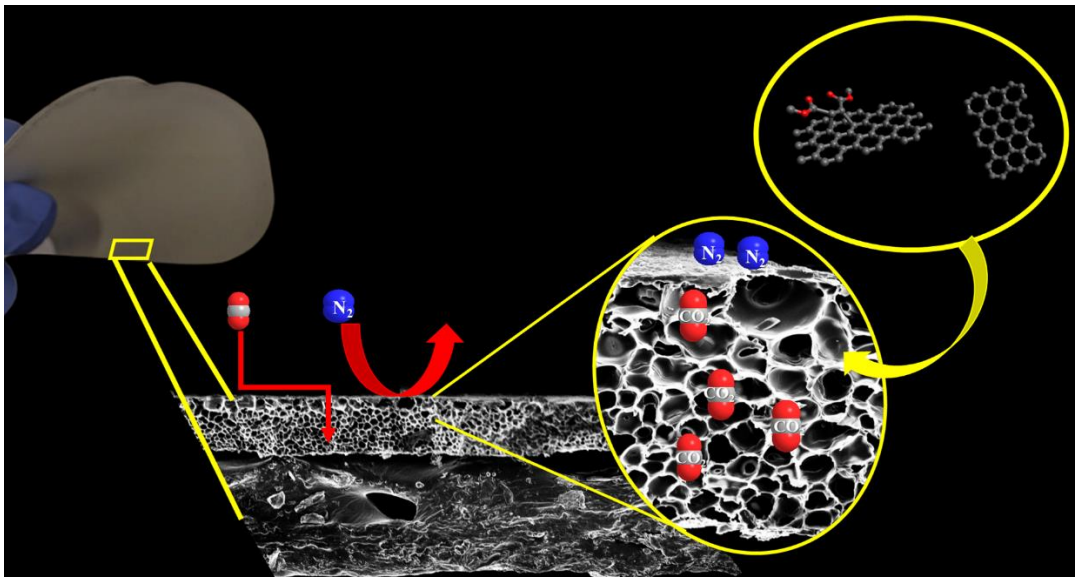

The relentless progress of human society, coupled with globalization, escalating emissions, and the apathy of political and economic forces, has brought our world to the brink of catastrophe. As signs of climate change become increasingly evident, institutions are finally recognizing the urgency and pushing for solutions before our familiar world undergoes irreversible transformation. In light of this, my thesis project is dedicated to exploring innovative materials for efficient separation of CO_2 from other pollutants, aligning with the overarching concept of a Circular Economy.

To achieve this objective, I conducted an in-depth study on Mixed Matrix Membranes (MMMs), focusing on the functionalization of graphene-based fillers. This involved both adapting existing methods from the literature and developing novel functionalization approaches. Over the course of my research, I successfully developed two new inorganic fillers: one containing Diethyl maleate (GEM) and

the other containing acetyl dicarboxylate (M). These fillers exhibited remarkable chemical and physical properties, such as ethanol dispersibility (GEM) and light emission upon stimulation (M60).

Simultaneously, I investigated the optimal concentration of exfoliated graphene in glassy polymer, specifically PSU, and an ionic liquid (BMIM Succ.) for enhanced CO_2 separation. Additionally, I explored the application of the highly innovative polymer PIM-1, which demonstrated exceptional CO_2 permeability. In this context, I examined the impact of functionalized graphene, namely tetra-cyan ethylene, on the performance of PIM-1.

Furthermore, I delved into the structural aspects of the membranes themselves, devising a multilayer configuration. This design featured a central body of PSU covered with either graphene materials or PIM-1, thereby creating distinct pore types. These specialized pores facilitated the concentration of CO2 on the membrane surface, enabling efficient separation.

Throughout this three-year endeavor, I meticulously documented the comprehensive scope of my research, presenting both remarkable and less favorable outcomes. This body of work serves as a valuable foundation for further development in this field.

List of acronyms

EPA: U.S. Environmental Protection Agency

CO_2: carbo dioxyde.

N_2: Nitrogen.

H_2O: Water.

CH_4: Methane.

BP: British Petroleum Company.

ILs: Ionic Liquids.

RTILs: room temperature ionic liquids.

TSIL: task specific ionic liquids

SILM: supported ionic liquids membrane

PIL: poly ionic liquids

MMM: Mixed Matrix Membrane.

MOF: Metal Organic Framework.

SWCNT: Single Wall Carbo Nano Tube.

MWCNT: Multy Wall Carbo Nanotube.

PSU: Polysulfone.

PIM-1: Polymers with Intrinsic Micro porosity.

BMIM Succ: 1-Butyl-3-methylimidazolium Succimidate.

BMIM Ac: : 1-Butyl-3-methylimidazolium acetate.

THF: Tetrahydrofuran.

$CHCl_3$: Chloroform.

$CHCl_2$: dichloro methane.

NMP: 1-methyl-2 pyrrolidone.

DMSO: dimethyl sulfoxide.

GO: graphene oxide.

rGO: reduced graphene oxide.

EG: exfoliated graphene.

GEM: graphene diethyl maleate.

MW: microwave

M(temperature): graphene functionalized with acetyl dicarbossilate at different temperature. *Example M60= graphene functionalized at 60°C with acetyl dicarboxylate*

RT: Room Temperature.

Dio: dioxane.

DSC: Differential scanning calorimetry

TGA: Thermogravimetric analysis

FTIR: Fourier-transform infrared spectroscopy

TGA-IR: Thermogravimetric analysis coupled with infrared spectroscopy

DVS: Dynamic Vapor Sorption vacuum experimental apparatus

FESEM: Field Emission Scanning Electron Microscopy

ESEM: Environmental scanning electron microscope

XPS: X-ray photoelectron spectroscopy

XRD: X-ray Powder Diffraction

TCNE: tetracyano ethylene.

GTCNE: graphene funtionalizad with tetracyano ethylene.

PIM(GTCNE): MMM with PIM-1 and GTCNE.

PIM(GTCNE)IL: MMM with PIM-1 GTCNE and BMIM Succ.

PSU1G: PSU with 1% of EG.

PSU2G: PSU with 2% EG.

PSU5G : PSU with 5% of EG.

PSU2GIL: PSU with 2% EG and BMIM Succ.

PSU5GIL: PSU with 5% of EG and BMIM Succ.

GEM[PSU]: PSU covered with GEM on the surface

PIM[PSU]: PSU containing the surfaces covered by PIM-1

PIMGTCNE[PSU]: PSU containing the surfaces covered by PIM-1 with GTCNE.

PSU/PIM: Membrane with 75% of PSU and 25% of PIM-1

.

Contents

List of Figures

List of Tables

Chapter 1

Introduction

1.1 Climate change and Greenhouse gases.

Years ago, the famous popularizer of science, David Attenborough, said this sentence, "There is no doubt that climate change is happening; the only debatable point is the role man is playing in it." [1]

The topic of climate change has been around the world for years, various distinguished figures, scientists, politicians, philosophers, and economists over the years have tried to warn that action was needed before we reach a point of no return, with irreparable damage to the planet, and consequently to the life forms on it.

Only in recent years does it seem that more political and economic forces have realized that time is limited and that it is necessary to act as soon as possible.

Excessive consumption of single-use materials, transportation of goods, intensive production, computer networks, and social media, as well as agribusiness strategies, are all contributing factors to the current climate emergency. These practices lead to economic growth but also result in a significant amount of waste and pollution that is difficult to dispose of and reuse [2].

Now more than ever, the scientific world, with more support from the political class, is focused on countering the climate emergency.

The focus of current studies it to improve the use of renewable energy sources and manage waste disposal in the environment.

Current studies include the goal of decreasing the concentration of greenhouse gases in the atmosphere.

The intensive production brought about by globalization has led to a significant increase in greenhouse gas concentration in the atmosphere over the years [3].

A greenhouse gas is defined as any gas that can absorb the infrared radiation emitted by the earth's surface, transmit it back to the earth's surface, thus contributing to the greenhouse effect.

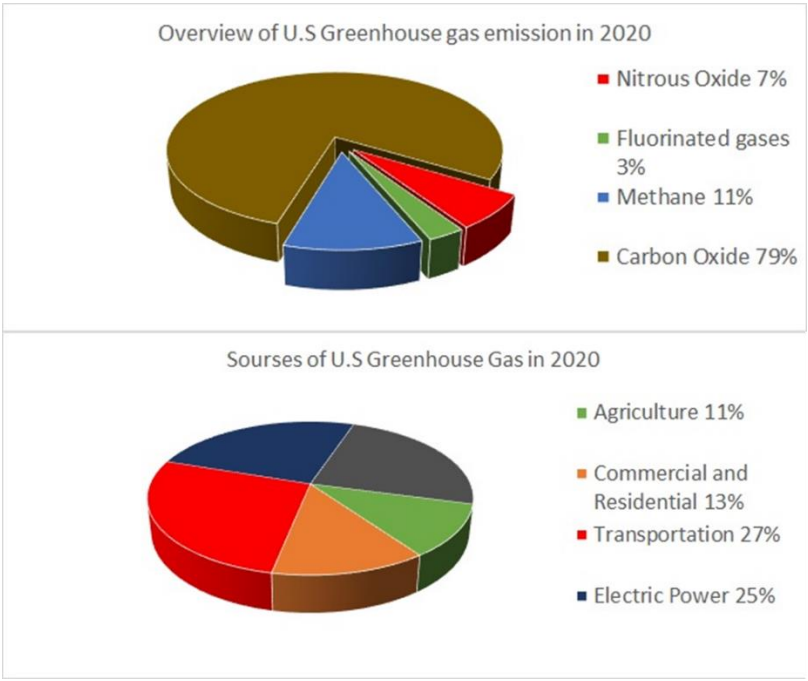

Figure 1 The percentage composition data of Greenhouse Gas produced in the U.S. to 2020 made by EPA[4].

Carbon dioxide has the highest concentration among greenhouse gases, followed by methane, nitrous oxide, and fluorinated species. [5]. According to EPA analysis, in 2022 the U.S. emits 79% of its greenhouse gases as carbon dioxide [4]. The transportation, energy, and industrial sectors emit about 75% of anthropogenic CO_2.

Since the signing of the Kyoto Protocol to date 41 nations and the European Union have committed to reducing their greenhouse gas emissions and atmospheric concentration. [6]

All branches of science are necessary to solve this dramatic problem. This is why over the years various methods for capturing and reusing CO_2 have been developed [7]: in fact, the goal is not only to eliminate these harmful gases but also

to be able to find alternative reuse, from energy reuse to the production of new materials.

During my Ph.D., I worked on developing new membranes to separate CO2 from flue gases. Separation is different from capture which involves developing materials that can capture and release CO_2 with minimal energy expenditure. Separation can be achieved by creating membranes that allow non-harmful gaseous species to pass through while retaining CO_2 or vice versa.

1.2 Gas separation with membranes

In technology, the general definition of the selective membrane means “a macroscopic formation characterized by the prevalence of surface area over thickness capable of regulating the passage of different molecular or ionic species, between two solutions/gas mixtures” [8]. Defining necessary parameters is important for assessing a membrane's quality and performance.

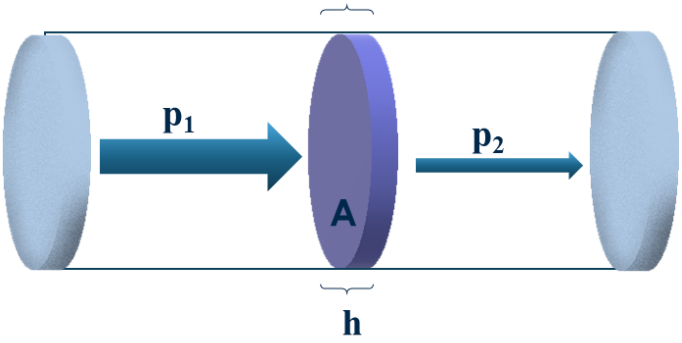

Figure 2: General and schematic model of the passage of a gas through a membrane

A generic membrane can be defined by its unit thickness 'h' and surface area 'A'. A membrane with such properties will present a specific Permeability ‘P’.

P is defined as the gas flow rate, Q, through a membrane of unit thickness, h, and surface area, A, caused by a pressure difference, Δp [9]. The flow rate is usually expressed as the volume at standard temperature and pressure and thus indicated as Q(stp)

$$P = \frac{Q(stp) * h}{A * \Delta p}$$

Eq 1

At the same time, permeability could be written also as the product of the diffusion coefficient D with the solubility coefficient K of a specific gas for a specific membrane.

$$P = DK$$

Eq 2

The SI unit of permeability is equivalent to m^3 (s^{-1} Pa^{-1}) but traditionally is commonly measured it in Barrer a not-SI unit of measurement defined as:

$$1Barrer = 10^{-10} * \frac{cm^3 * cm}{cm^2 * s * cmHg}$$

To understand the derivation of permeability equation is derived, we begin with the definition of permeation flux J, this parameter represents the volume flowing through the membrane per unit area per unit time.

$$J = \frac{V(g)}{A * t}$$

Eq 3

$$Q = \frac{V(g)}{t}$$

Eq 4

The flow rate Q is defined as the ratio of the volume of gas passing through the membrane in a unit of time (Eq 4). Hence, J can be re-expressed as:

$$J = \frac{Q}{t}$$

Eq 5

The passage of a specific volume of gas through the membrane depends on the solubility of the gas in the membrane and its diffusion through it. The movement of gas through the membrane is also dependent on the pressure difference that is created, the flow of gas will move from the area with greater pressure to the area where the pressure is less. Based on these parameters J can also be expressed as the product between the solubility and diffusion coefficients, multiplied by the pressure change and divided by the thickness of the membrane.

$$J = \frac{DK * \Delta p}{h}$$

Eq 6

Combining this equation with (Eq 2) and making the appropriate substitutions we derive Eq 1.

$$P = DK$$

$$DK = \frac{Q(stp)h}{A\Delta p}$$

$$P = \frac{Q(stp) * h}{A\Delta p}$$

The perm selectivity, represented by the dimensionless parameter α, is another important parameter necessary to evaluate a membrane for a specific gas.

This dimensionless parameter is used to assess the discriminatory ability of a membrane for two gas species. Is represented by the ratio of the permeabilities of two specific gases [10].

$$\alpha = \frac{P(a)}{P(b)}$$

Eq 7

By combining with equation P=DK:

$$\alpha = \frac{D(a)K(a)}{D(b)K(b)}$$

The ratio of diffusion constants D(a)/D(b) can be defined as the selectivity of one molecule over another in terms of diffusion, when gases cross a membrane without chemical interactions, this ratio reflects the different sizes of the molecules constituting the pure gases studied.

The ratio of the solubility constants of two gases K(a)/K(b), represents the adsorption selectivity, or solubilization of a specific gas in the membrane, again if no chemical interactions are present within the pores of the membrane, this ratio can be viewed as the difference in condensation capacity of two gases for a given membrane.

Permeability and selectivity are two critical parameters with a strong interdependence for membrane evaluation.

Llyod Robeson analyzed the relationship between these two parameters by plotting the data of known membranes and placing them on a Cartesian axis, with selectivity on the y-axis and permeability on the x-axis [11–13]. It was then deriver an empirical relationship: "to increase the permeability of a membrane it is necessary to sacrifice selectivity and vice versa". By entering each data of permeability and selectivity Robeson drew a boundary line defining it as a limit beyond which existing membranes are unable to cross.

These constrains were illustrated theoretically by Freeman [9,14]with the following equation:

$$\ln \alpha_{A/B} = -\lambda_{A/B} \ln D_A + \left\{ \ln\left(\frac{S_A}{S_B}\right) - \lambda_{A/B}\left(b - f\left(\frac{1-a}{RT}\right)\right)\right\}$$

Eq 8

Where the parameter $\alpha_{\frac{A}{B}}$ is the permselectivity of gas A concerning gas B the term $\lambda_{\frac{A}{B}}$ is defined as:

$$\boldsymbol{\lambda_{\frac{A}{B}} = \left(\frac{D_B}{D_A}\right)^2 - 1}$$

Eq 9

D is the kinetic diameter characterized as the smallest zeolite window through which a penetrant molecule can fit [15] and a and b are constants absolute or depending on the polymers while f depends on the polymer state and increases by

increasing polymer stiffness and interchain packing [14]. From equation 8 thus the diffusivity determines the upper bound selectivity of polymers for gas separation. The solubility selectivity term is believed to change little from polymer to polymer, while the term $\lambda_{A/B}$ B is constant for a given gas pair and polymer class. Based on the agreement of the theory with experimental data, polymers with high glass transition temperature and a rigid backbone that have large interchain spacings are believed to lie on or near the upper bound lines for many gas pairs.

The most effective approach to improve the performance of polymeric membranes is to enhance solubility selectivity, increase chain stiffness, and/or expand interchain spacing. While greater interchain separation can boost permeability, it must be accompanied by increased chain stiffness to achieve both higher permeability and selectivity. However, the asymptotic endpoint in the performance of polymeric membranes would be reached when the interchain separation becomes too large, and polymer segmental motion no longer governs penetrant diffusion. To achieve higher selectivity/permeability combinations, it may be necessary to explore materials that do not conform to these basic principles.

Attempts have been made over the years to surpass that boundary line, referred to as the Robeson upper limit, by designing new membranes that would allow facilitated gas transport by increasing the permeability for a specific gas, without having a change in the selectivity ratio.

Membranes made from glassy polymers, such as polysulfone (PSU) or polymers with intrinsic microporosity (PIMs) have exhibited enhanced selectivity towards specific gaseous species [13,16,17].

The rigid structure of these polymers enables the formation of highly porous membranes, with selectivity arising from the size of the gaseous molecules. Only a limited range can cross the membrane, leading to physical selectivity.

The incorporation of ionic liquids in the membrane can enhance permeability towards gaseous species such as CO_2. [18] These materials can be either liquids where CO_2 has high solubility compared to other gaseous species, or chemical reactions can occur between the ionic liquid and CO_2 e.g. the reported between primary/secondary amines and CO_2 itself:

$$2RNH_2 + CO_2 \longrightarrow RNHCOO^- + RNH_3^+$$

In the following sections, various types of membranes created using ionic liquids will be briefly analyzed. Additionally, certain types of membranes prepared with glassy polymers, such as PIM-1 and PSU, will also be briefly presented. Finally, we will explore Mixed Matrix Membranes (MMM) in depth, which are distinguished by the inclusion of inorganic particles within their matrix.

1.2.1 Ionic liquids applied for gas separation.

Ionic liquids offer a promising solution for capturing and releasing CO_2 with minimal energy expenditure [19]. Ionic liquids are composed of charged organic molecules bound by ionic bonds and exhibit liquid properties also below 100 °C while possessing a high boiling point. With various types of ionic liquids available, they have generated significant interest in the scientific community and gas separation field due to their ability to dissolve CO_2 and exhibit negligible vapor pressure.

In recent years, researchers have developed various types of membranes that incorporate ionic liquids or their polymeric derivatives, known as poly ionic liquids (PILs), to enhance membrane properties and surpass the Robeson limit [20]. Unlike ionic liquids, PILs remain in the rubbery or in the glass state, at room temperature [21].

Ionic liquids can be classified based on their interaction with CO_2, with room temperature ionic liquids (RTILs) capable of facilitating the physisorption of CO_2 and exhibiting high solubility for this gas (Figure 3). This unique interaction has enabled the design of several membranes that demonstrate high CO_2 permeability. [20,22,23].

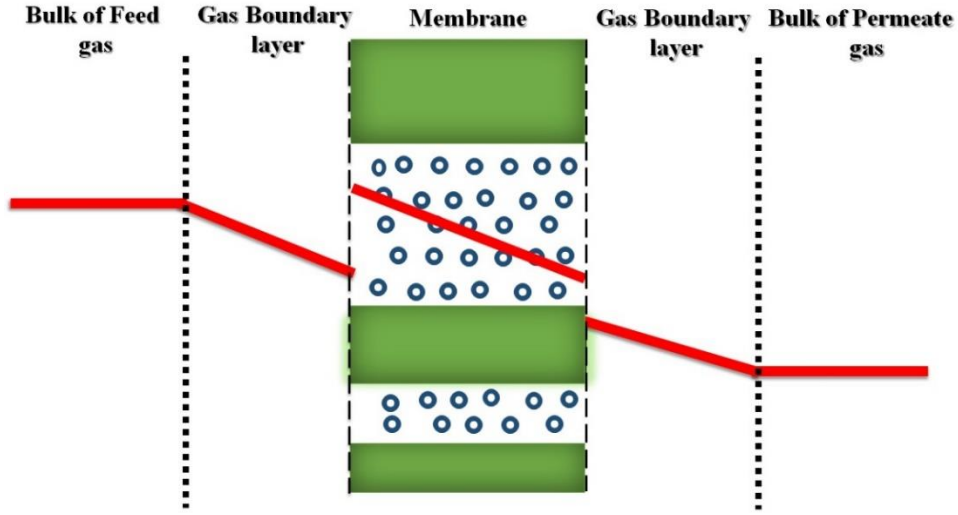

Figure 3: Membrane contains RTILs, pore dissolution mechanism. The red line indicates the concentration of CO_2.modify by Zeng et all [19]

Task-specific ionic liquids (TSILs) [20,24] are ionic liquids that can chemically interact with CO_2 by binding with the gas to form a complex molecule. This interaction is reversible, enabling the CO_2 to be easily released from the complex with minimal energy requirements (Figure 4).

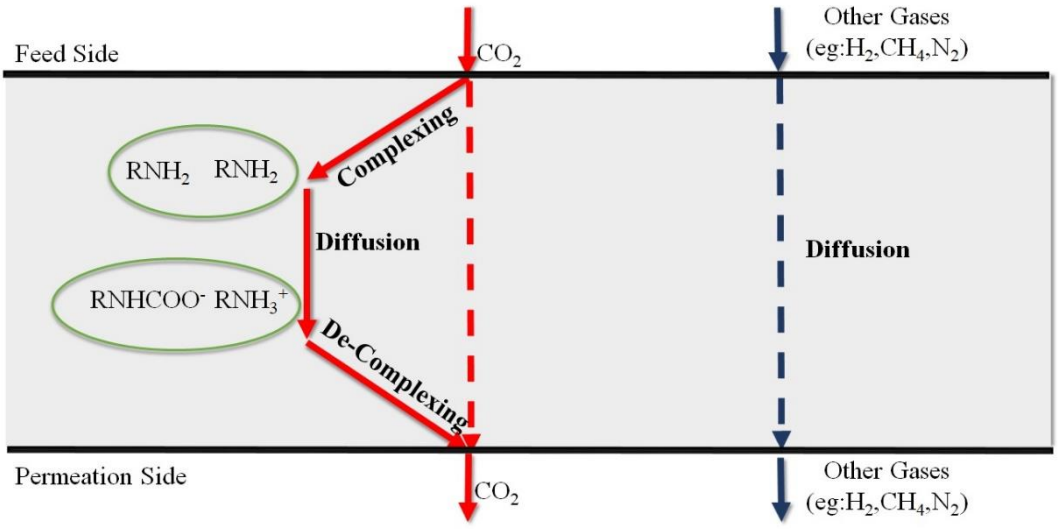

Figure 4: Mechanism of CO_2 diffusion into membranes containing task specific ionic liquids.[19]

Several types of membranes containing ionic liquids can be distinguished: *supported ionic liquid membranes (SILMs), poly-ionic liquid membranes (PILM),*

ionic liquid-polymer composite membranes (ILs-P), mixed matrix membranes (MMM), ionic liquid-gel membranes (ILs-G).

SILMs, or supported ionic liquid membranes, are porous polymer membranes that are infused with ionic liquid through a soaking process. Typically, these membranes contain pores with an average size ranging between 100-200 nm.

SILMs that incorporate room-temperature ionic liquids have demonstrated enhanced CO_2 permeability. When prepared with hydrophobic support, these membranes exhibit greater mechanical and material aging stability than those produced with hydrophilic supports. By utilizing ionic liquids with lower molecular size and viscosity, both permeability and selectivity have been observed to increase. Despite these improvements, these membranes do not exceed the Robeson limit. [25]

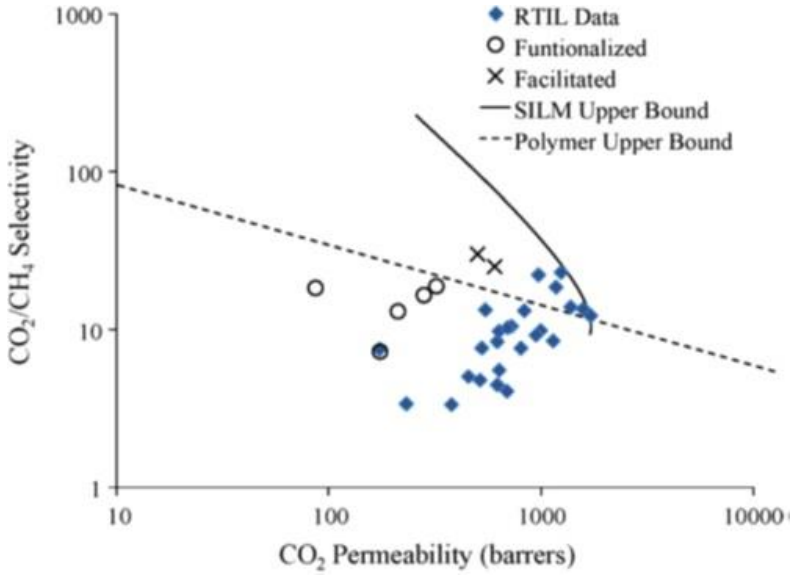

Figure 5: SILMs breaking the Robeson limit[25]

However, it has been observed that as the temperature increases, ionic liquids CO_2, solubility decreases significantly decreasing permeability and selectivity. Therefore, while these membranes may be useful for separating atmospheric CO_2, their application for separating CO_2 from combustion gases is limited due to their temperature sensitivity [26].

Amino acid ionic liquids have been employed to create SILMs that are suitable for post-combustion gases. Nevertheless, these membranes are sensitive to changes in

both CO_2 partial pressure and temperature. It has been observed that as the CO_2 partial pressure increases, both CO_2 permeability and CO_2/N_2 selectivity decrease. At relatively low CO_2 partial pressure and temperature not too high, these membranes exhibit high gas permeability and CO_2/N_2 selectivity values.

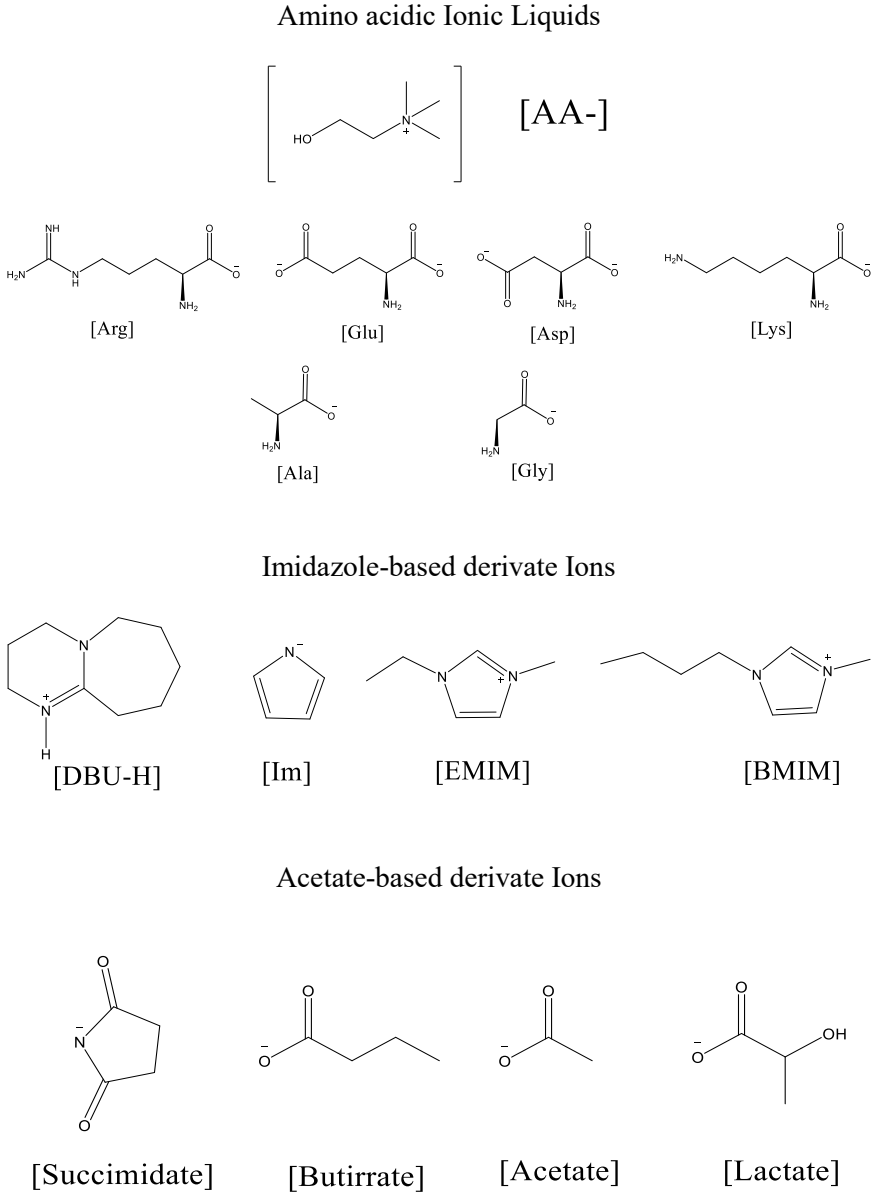

Figure 6: Task-specific ionic liquids

These membranes, containing carboxylate-derived ionic liquids, are promising for the separation of syngas due to their affinity for acidic gases and their low molar volume. However, one issue with these membranes is the potential formation of a pseudo-polymeric ionic network when certain ionic liquids are used, leading to an increase in viscosity and reduced CO_2 diffusion through the membrane. [27].

Poly-ionic liquid membranes are a class of membranes that are formed by polymerizing ionic liquids, resulting in charged chains [28]. These polymers exhibit a greater capacity for capturing and releasing CO_2 compared to the monomers they are derived from. This class of membranes can be further categorized into three subfamilies: *PILs homopolymers, PILs copolymer membranes, and PILs-IL composite membranes.*

The presence of charged functional groups on the chain induces the formation of a thinner, stiffer, and more stable matrix, which gives the membrane high strength, prevents excessive swelling, and allows it to maintain gas separation performance even under high temperature and pressure conditions [29].

PILs homopolymers consist of a single monomer that can be prepared, for example, by light-induced radical reactions.

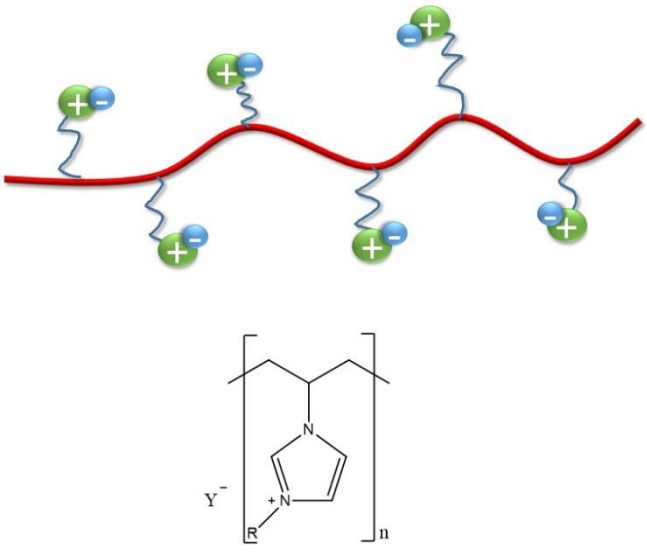

Figure 7: Homo PILs model

This class of membranes is known to have low mechanical performance and high brittleness, small CO_2 permeability but good CO_2/N_2 selectivity [30]

PILs copolymer membranes can be further divided into block copolymers and ABC triblock copolymers, which are mechanically more resistant and have a higher density and lower fractional free volume, leading to higher CO_2 selectivity. [31] Liquid grafting onto the polymer chain using atom transfer radical polymerization (ATRP) has shown promising results, with some membranes achieving a permeability of 2340 Barrers and CO_2/N_2 and CO_2/H_2 selectivity of 10.2 and 3.2, respectively [32,33]. Recently, the effect of water vapor on these membranes has been investigated, revealing that the membrane that usually exhibits a hydrophobic nature has instead a hydrophilic response influencing the transport properties of the membrane [34].

Finally, PIL-based membranes containing free ILs in their matrix have been developed [35]. These membranes have demonstrated superior resistance and flexibility compared to PIL-only membranes due to the plasticizing properties of the ionic liquids [36]. The PIL provides stabilization, preventing the leakage of the IL from the membrane. The interaction between PIL and IL is considered stronger than that between IL and a conventional polymer [37].

These characteristics make these membranes highly resistance to high-pressure operation although, the concentration of the ionic liquid within the membrane must be carefully balanced to optimize both permeability and selectivity [38]

Other types of membranes incorporating ionic liquids include IL-Gel Membranes and polymer-IL composite membranes. IL-Gel Membranes are prepared by adding a small amount of low molecular weight organic gelling agents (LMOG) to the IL, which retains the transport properties of a gas in a liquid and has possible industrial applications. However, increasing the amount of LMOG in the mixture results in a trade-off between mechanical stability and permeability [38,39].

Polymer-IL composites consist of uncharged polymers and ionic liquids that are mixed and then solidified via solvent removal. The addition of ionic liquid has a plasticizing effect which increases the flexibility of the polymers and reduces the risk of leakage when compared with SILMs. Several studies have investigated these membrane types, including one notable example involving the use of polyvinyl difluoride (PVDF) with 70% of the total membrane weight composed of ionic liquid

[C_6MIM][Tf_2N][41]. The membranes have demonstrated a thousand-fold increase in CO_2 permeability, and The presence of the ionic liquid in the polymer matrix leads to a 100-fold increase in the permeability capacities of the ionic liquid compared with pure polymer and neat ionic liquid, from a nanoscale study it was observed the presence at the level of the membrane matrix of nanodomains built by the aggregation of neutral alkyl tails of the polymer, surrounded by charges, causing uniform spatial distribution is determined by the strong electrostatic interactions. [19,42].

Mixed-matrix membranes are a class of polymer matrix membranes that incorporate both an ionic liquid and a solid inorganic filler, which can significantly impact the membrane's selectivity. The subsection 1.2.3 Mixed Matrix Membranewill provide a more comprehensive discussion of these materials.

1.2.2 Glassy Polymers PSU and PIM-1

Glassy polymers are polymers that possess rigid molecular structures, which are formed from the presence of cyclic, polycyclic, and aromatic monomers. The unique structures of glassy polymers, [17], coupled with their non-crystalline amorphous nature, result in high stiffness and dimensional selectivity, which creates intrinsic pores that permit the passage of specific molecules. Moreover, glassy polymers are highly resistant to mechanical stresses. In this section, we will focus on two noteworthy members of this class: polysulfone (PSU) and PIM-1.

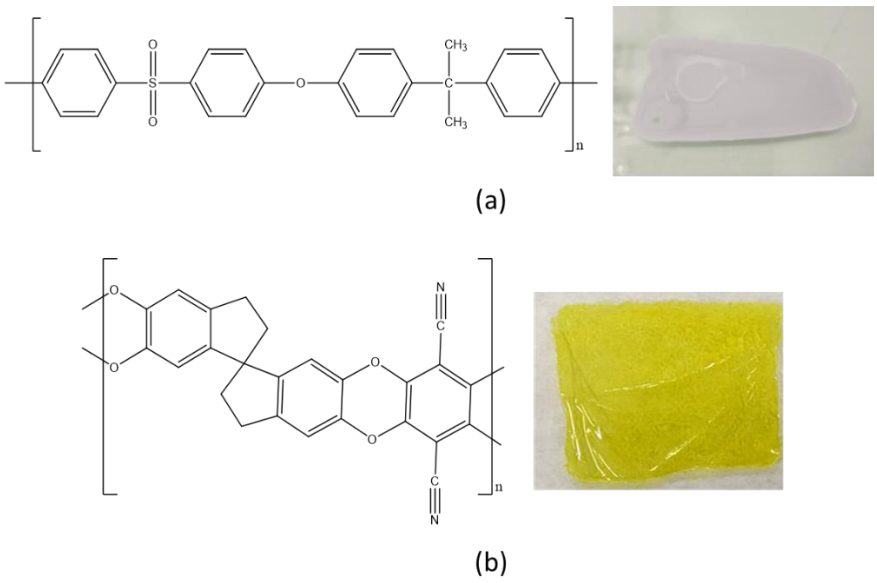

Figure 8 The molecular structures of PSU (a) and PIM-1 (b) and their corresponding membrane appearances.

Polysulfone (PSU) is a highly versatile synthetic polymer that finds wide application in membrane design [43] due to its exceptional properties. PSU exhibits several desirable properties, including resistance to the entire pH range, high mechanical strength against bending, torsion, and fracture, and a high glass transition temperature of 150-170°C. Furthermore, PSU is highly resistant to compressive stress, which makes it a promising material for demanding applications. PSU is also an inexpensive polymer, and this has pushed much toward its use for CO_2 separation.

PSU is an excellent material for membrane applications, owing to its outstanding physical and mechanical properties, as well as its ease of production. Over the years several studies have been focused on improving the permeability and selectivity of PSU membranes. One effective strategy is to incorporate PSU into composite membranes containing other polymers, either as a matrix in mixed matrix membranes (MMMs) or by adding inorganic fillers to the membrane. For example, a PSU composite membrane with a 2:1 ratio of polyethylene glycol exhibits a permeability of 7644 Barrer, which can be further enhanced by incorporating silica nanoparticles. A PSU membrane containing 20% silica nanoparticles demonstrates remarkable permeability of 13359 Barrer [44]. In addition, there has been a significant increase in the pure selectivity of CO_2/N_2 from

32,125 to 45,763. Later on, we will delve deeper into this topic, specifically focusing on MMMs.

Recent studies have explored various approaches to enhance the performance of composite membranes beyond the use of inorganic nanoparticles. one such approach is the incorporation of ionic liquids which has been shown to significantly increase CO_2 permeability at room temperature compared to pure PSU membranes. Farrokara et al. reported an almost 100-fold increase in CO_2 permeability with the presence of the [Emim][BF_4] in composite membranes. [45] Additionally, the incorporation of ionic liquids has been demonstrated to improve CO_2/CH_4 selectivity, with a 40% concentration of [Emim][BF_4] in the membrane increasing selectivity from around 8 to 21.

Another class of polymers that has gained significant interest is polymers with intrinsic microporosity (PIMs), which consist of a rigid polycyclic function. PIMs have a continuous, interconnected network of pores with a size less than or equal to 2nm [46], and PIM-1 is one of the most important members of this class. Produced by condensing 5,5,6,6-tetrahydroxy-3,3,3,3-tetramethyl-1,1-spirobisindane with tetrafluoroterephtalonitrile [47]. These polymers are of significant interest due to their high gas permeability [12].

Extensive research has been conducted on the gas separation characteristics of PIMs and the impact of different pretreatments on their separation performance. [12,47].PIMs have the highest solubility coefficient among glassy polymers, and untreated PIM-1 has a CO_2 solubility similar to that of PTSMP. However pre-treated PIM-1 by heating or exposure to polar solvent vapors like methanol can triple its permeability, compared to a maximum of 300($10^3 cm^3(stp)\ cm^{-3} cmHg^{-1}$) of treated PTSMP [16,48,49]. The permeability in these membranes is strongly affected by the pre-treatment of the material with preheating or the use of methanol vapors [46]. Fox example, the permeability of dry PIM increases from 150 Barrer to 1650 Barrer after pretreatment with methanol. Despite exhibiting high permeability, PIM membranes show varying selectivities for different gases such as CO_2/CH_4 and CO_2/N_2. While there is a slight increase in selectivity in the former case, CO_2/N_2 selectivity decreases [47]. Nevertheless, PIM membranes are capable of surpassing the Robeson limit in terms of comparing CO_2 permeability and CO_2/N_2 selectivity, as well as in terms of selectivity between CO_2 and CH_4 and CO_2 permeability [16].

1.2.3 Mixed Matrix Membrane

Mixed matrix membranes (MMM) have attracted considerable attention in recent years due to their ability to combine the advantages of both organic and inorganic materials. MMMs consist of an organic polymer matrix in which an inorganic material is dispersed (Figure 9). While organic membranes typically exhibit a tradeoff between permeability and selectivity, membranes with inorganic materials have shown excellent gas separation performances, often surpassing the Robeson limit. Common inorganic materials used in MMMs include silicones, palladium, silver, or titania [50] which also provide the added benefits of being highly resistant to pressure, mechanical forces, and high temperatures.

However, the main drawback of inorganic membranes is their high cost and difficult preparation, which poses challenges for industrial applications. Therefore, researchers have focused on developing MMMs that combine the advantages of organic and inorganic materials. These membranes have the potential to achieve high separation performance while also being cost-effective and easy to prepare.

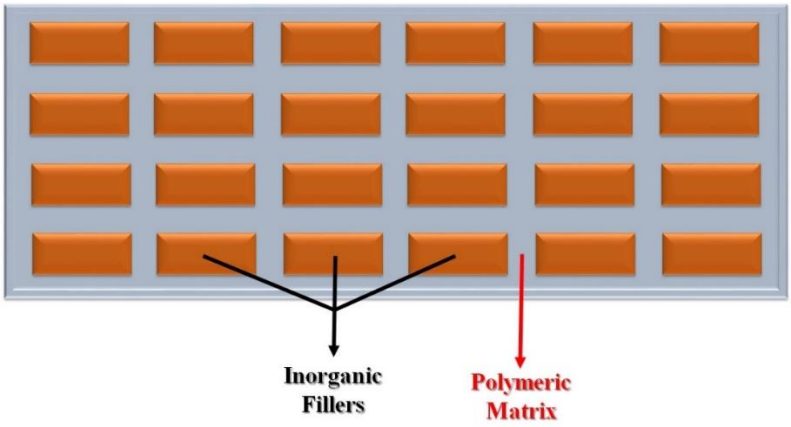

Figure 9 shows a schematic representation of a mixed matrix membrane (MMM) composed of an organic polymer matrix and inorganic particles.

MMMs incorporating inorganic nanomaterials into the organic matrix have been found to exhibit excellent permeability and higher selectivity compared to membranes made solely with the organic starting matrix. However, the preparation of MMMs presents challenges [51], including the compatibility of the polymer matrix with the organic filler, aggregation, and sedimentation of the fillers on one side of the membrane. Therefore, the study of MMMs focuses on the preparation methodology and overcoming these problems. Factors affecting the performance of

these membranes include the size of the nanoparticles, their concentration in the matrix, and the stiffness of the polymer chain.

Various methods have been developed to address these challenges: For example, plasticizers like dibutyl phthalate can be used to decrease the stiffness of the matrix, fillers can be dispersed in low-boiling solvents and subsequently cast on the membrane at the polymer glass transition temperature (Tg), chemical modification of the filler can be done to improve compatibility with the organic matrix [52], or copolymers can be used to decrease the surface tension of the nanomaterials with the organic surface.

Different inorganic materials have been used as fillers for the mixed-matrix membranes. Among the first fillers used are metal oxides such as alumina (Al_2O_3) and Titania TiO_2. In a study, by Nematollahi et al. [53], the insertion of varying concentrations, in weight percent, of Al_2O_3 nanoparticles into a poly(4-methyl-1-pentyne) (PMP) polymer matrix was shown to significantly enhance the permeability for CO_2 as the concentration of alumina nanoparticles in the matrix increases. The presence of this metal oxide leads to an increase in the free volume, with an ideal concentration of 30% of the total mass of the membrane being necessary to achieve good CO_2/N_2 selectivity.

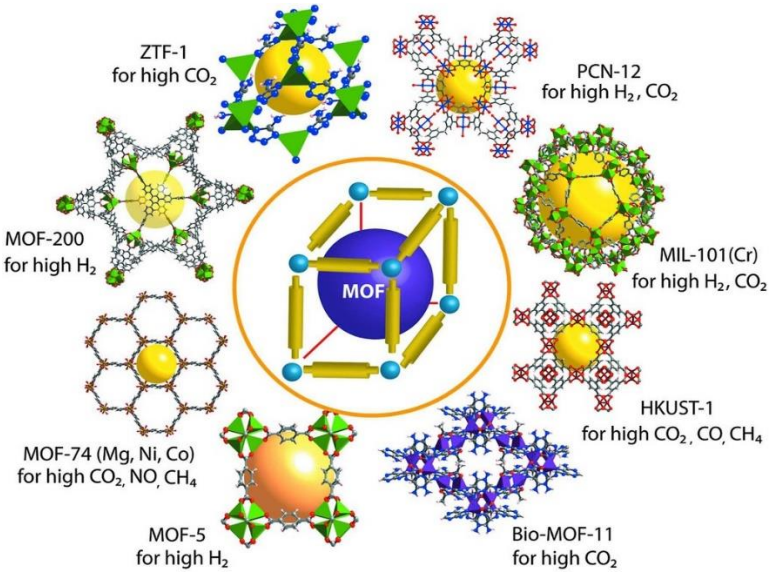

Figure 10 Three-dimensional structures of various Metal-Organic Frameworks (MOFs) showing the size of pores. [54]

Metal-organic frameworks (MOFs) are another group of inorganic materials that have attracted significant attention in MMMs research. These materials are known for their low density, high surface area, tunable porosity, and chemical functionality. Various studies have been conducted on MMMs incorporating MOFs, and some have shown high permeability and increased selectivity for specific gases. For example, Nik et al. investigated the use of five different MOFs, including UiO-67, NH2-UiO-66, MOF-119 (Cu-BTC), NH2-MOF-199, embedded in a Matrimid polymer matrix [55]. Among these, MMMs prepared with UiO-66 exhibited the highest CO_2 permeability, while MOFs with amine functional groups such as NH2-UiO-66, showed not only high permeability but also increased CO_2/CH_4 selectivity. In another study, Bi et al. reported the use of co-benzo carboxylate MOF nano-sheets (CBMNs) embedded in 6FDA-durene-DAB [56] polymer matrix, achieving a selectivity of 33.6 for CO_2/CH_4 and 42.0 H_2/CH_4, respectively.

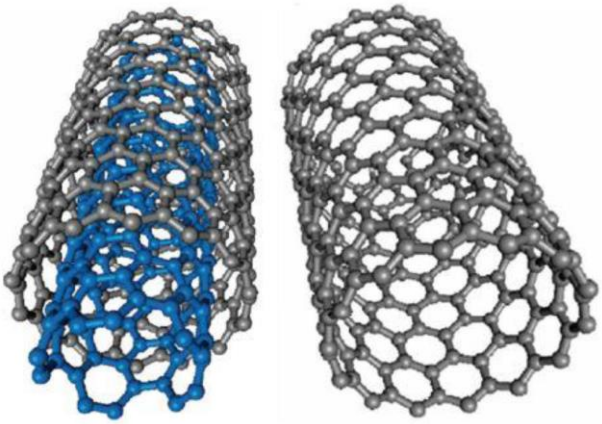

Figure 11 structure of multiwall (left) and single-wall (right) carbon nanotubes[57].

Carbon nanotubes (CNTs) are highly desirable filler materials for mixed-matrix membranes (MMMs) because of their remarkable flexibility, elasticity, tensile strength, and thermal conductivity [58,59]. Depending on their structure, CNTs can be classified as single-wall CNTs (SWCNTs) or multi-wall CNTs (MWCNTs) [60]. Simulation studies by Skoulidas et al. suggested that CNTs could exhibit exceptional permeability and selectivity compared to other organic fillers [61]. In line with this, Kim and his research group were the first to successfully incorporate

SWCNTs into a polyimide siloxane copolymer matrix, confirming Skoulidas' predictions [62].

Khan et al. prepared MMMs based on polyimide (PIM-1) and functionalized multi-wall carbon nanotubes (MWCNTs) with polyethylene glycol (PEG), which exhibited an impressive CO_2/N_2 selectivity of about 33 [63]. Jiang et al. developed an MMM using single-wall carbon nanotubes (SWCNTs) and graphene oxide (GO) as fillers, demonstrating improved membrane permeability attributed to the synergistic effect of the two carbon nanomaterials [64] Additionally, incorporating ionic liquids within MMMs have shown the potential to enhance the MMM selectivity and improve the interfacial wettability between the filler and inorganic matrix [65].

1.2.4 Graphene as Filler applied to gas separation.

Graphene is a two-dimensional allotrope of carbon composed of a single layer of atoms, possessing the strength characteristics of the diamond, high thermal and electrical conductivity, and remarkable chemical stability. [66,67]

Given these exceptional properties, researchers have shown significant interest in graphene and have explored its potential applications in various technological fields, such as electronics and thermal management in circuits [67,68]. In recent years, numerous composites containing graphene nanoparticles have been developed to improve the physical properties of materials. These composites have shown promising results in enhancing mechanical, thermal, and electrical properties.

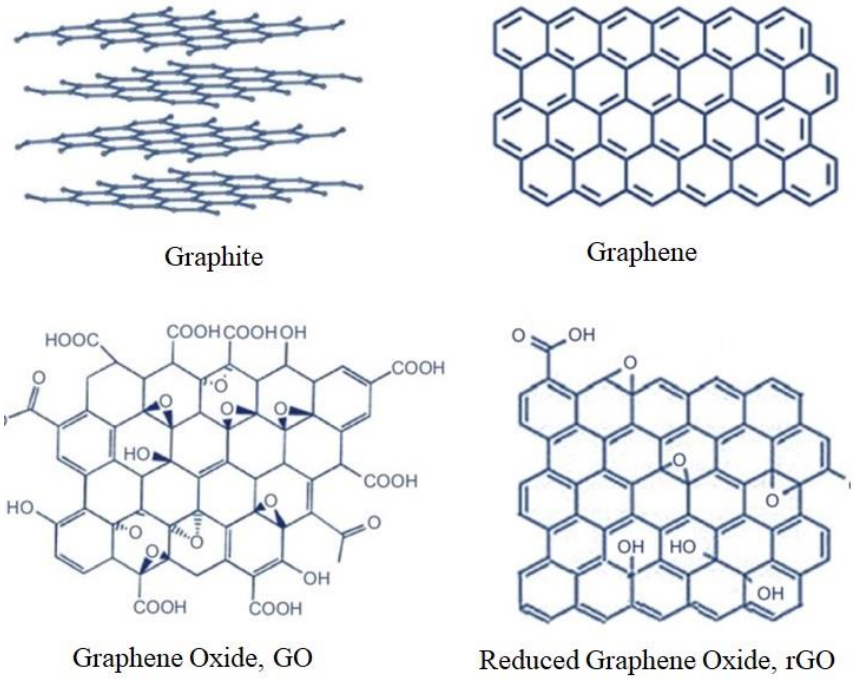

Figure 12: Comparison of the structures of (a) graphite, (b) graphene, (c) graphene oxide (GO), and (d) reduced graphene oxide (rGO). Graphene is a single layer of graphite, while GO is an oxidized form of graphene with oxygen-containing functional groups on its surface. rGO is obtained by reducing GO through chemical or thermal treatments, resulting in the removal of some of the oxygen groups. [69]

Extensive scientific research has focused on the synthesis and scalability of graphene for industrial production. In addition to pristine graphene, graphene oxide (GO) has garnered significant attention. GO is produced through the oxidation-exfoliation reaction of graphite, resulting in a highly oxidized mono-layer of graphene. It possesses a large number of epoxy, carboxylic, and other oxidized forms of carbon groups on its surface, making it more reactive compared to exfoliated graphene [70,71]. Although pristine graphene obtained through graphite exfoliation [72] is commonly used, the reduced form of oxidized graphene, known as rGO, is preferred in certain applications despite having a higher number of electronic defects on its surface [73]. Interactions between these forms of graphene and various gases have been observed. For instance, a modeling study by Du et al. demonstrated that nanoporous graphene, which lacks a continuous surface, can separate H_2 and N_2. This separation is partly attributed to the Van der Waals interactions between graphene and N_2, which impede the gas passage through the pores. GO exhibits a surface rich in carboxy-derivative groups, and studies have shown that these groups confer CO_2-philicity to the material, enabling its

application as a CO_2 capturer [74]. It is, therefore, unsurprising that graphene-based materials have garnered significant interest in mixed matrix membrane (MMM) design.

The presence of graphene or graphene oxide in the membrane matrix significantly impacts gas separation performance. For example, Yousef et al. studied a PEBA-based membrane with porous graphene as a filler, and when the membrane contained 0.4% of graphene by mass, an increase in permeability for CO_2 and CH_4 were observed, with a value of 387 Barrer and a CO_2/CH_4 selectivity of 32 at a temperature of 55°C. In the case of the Pebax and GO nanocomposite with a 0.02% GO concentration, an increase in CO_2 permeability from 364 Barrer (pristine Pebax) to 371 Barrer was observed. However, at a GO concentration of 1%, a decrease in CO_2 permeability with a value of 51 Barrer was noted [75]

Functionalizing the filler with GO has been shown to enhance its affinity to the polymer matrix and CO_2. For instance, by inserting GO functionalized with aminosilane, the permeability of Pebax increased to 913 Barrer, and the CO_2/N_2 selectivity rose to 71, surpassing Robeson's limit [76].

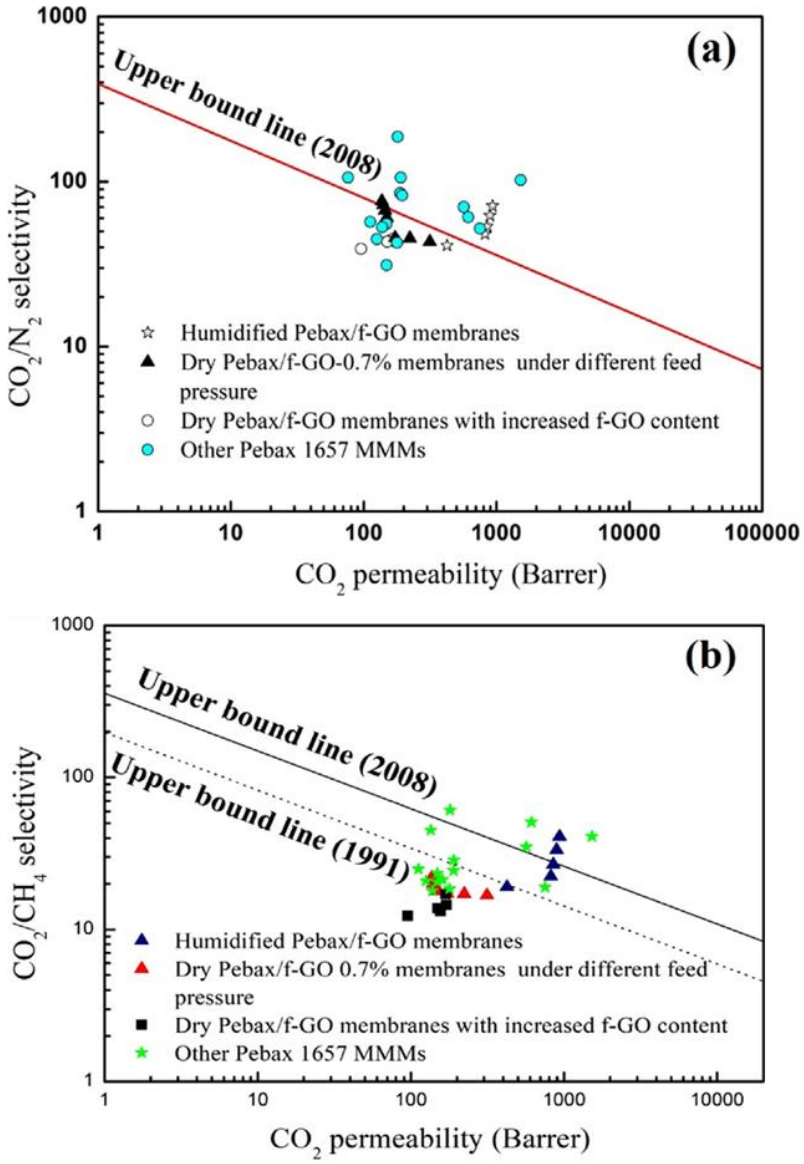

Figure 13 (a) CO_2/N_2, (b) CO_2/CH_4 separation performances of membranes in Robeson upper bound plot. [76]

Sainath et al. investigated the performance of hollow fiber PSU membranes containing 0.25% GO in the matrix. They reported a CO_2 permeability of 38.76 Barrer, which was 135% higher than that of pure hollow fiber PSU. However, the CO_2/CH_4 selectivity was only 6.42 [77].

PIM-1-based MMMs containing graphene and GO have also been developed. Chen et al. at Xiamen University prepared and studied the performance of PIM-1 containing GO as a filler. They obtained high permeability values of 6169 Barrer

and CO_2/N_2 selectivity values of 123.5, which were higher than the performance of their synthesized PIM-1 [78]

Furthermore, the addition of only 0.05% by volume of few-layer graphene into the PIM-1 matrix was sufficient to achieve an impressive increase in permeability of PIM-1 to 12700 Barrer and a CO_2/CH_4 selectivity of 123.5. [79]

1.3 My project

This project focused on the design of membranes capable of efficiently separating CO_2 from flue gases by achieving high permeability and selectivity that surpass the Robeson limit. To achieve this goal, mixed-matrix membranes containing graphene as an inorganic filler were developed.

1.3.1 Idea

The design process of the mixed-matrix membranes began with a study of pristine graphene, which was obtained by sonication of graphite in NMP. Various functionalization techniques were explored to enhance the CO_2-philicity of graphene and its compatibility with the polymer matrix.

On the one hand during these years of research, I focused on the study and development of polymeric membranes based on PSU and PIM-1 containing exfoliated graphene, or ionic liquid of BMIM nature, how the presence of these components affects the performance of the membrane. by developing, with PSU, different membranes with different concentrations of EG and successively adding the ionic liquid to the formulation. In parallel, a study of PIM-1-based membranes containing, different concentrations of BMIM Succimidate or BMIM acetate ionic liquid was done, studying the variation of permeability, diffusion and solubility to CO_2 and N_2 according to the concentration and different nature of these two ionic liquids.

Also during doctoral research, it was studied how to increase the interactions related to graphene filler with the gaseous molecules under study , to do so, new graphene-based materials functionalized by cycloaddition were developed.

Graphene can be described as a continuous polycyclic structure consisting of hexagonal aromatic rings, exhibiting remarkable chemical stability due to the delocalization of electronic charges on its surface. The presence of conjugated

double bonds creates a continuous electron orbital on both sides of the graphene surface, contributing to its excellent thermal and electrical conductivity characteristics.

However, the covalent functionalization of pristine graphene is limited due to its inherent stability. One method that can be employed for covalent functionalization is cycloaddition via the Diels-Alder reaction.

Overall, this study aims to develop mixed-matrix membranes that can surpass the Robeson limit by achieving high permeability and selectivity for CO_2 separation from flue gases.

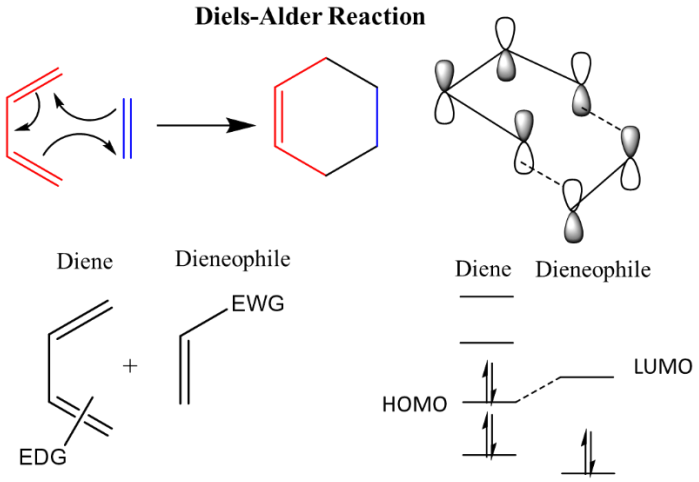

Figure 14 Diels-Alder reaction mechanism between a diene and a dienophile, showcasing the interaction between their frontier orbitals.

The Diels-Alder reaction is a condensation reaction that involves a conjugated diene and an unsaturated molecule, known as a dienophile, containing electron donor groups on the unsaturated carbons. This reaction mechanism relies on the fusion of the frontier orbitals of these molecular species, specifically the highest occupied molecular orbital (HOMO) of the electron-rich diene with the lowest unoccupied molecular orbital (LUMO) of the electron-poor dienophile [80]

In their comprehensive research, Sarkar et al. conducted a thorough investigation into the chemical properties of graphene and its potential for Diels-Alder type cycloaddition reactions [81]. Graphene exhibits a dual nature in its electronic structure, enabling it to act as either a diene or a dienophile depending on the reaction conditions. However, the covalent functionalization of pristine

graphene is limited due to its high chemical stability. Nonetheless, methods such as cycloaddition via the Diels-Alder reaction have demonstrated promising results in functionalizing graphene.

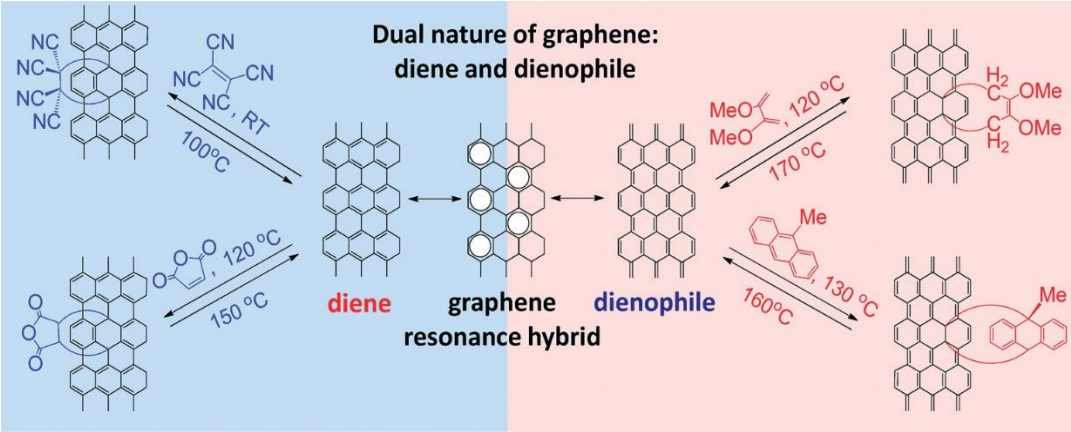

Figure 15 Dual nature of graphene such as diene and dienophile[81].

Graphene exhibits diene-like behavior when it undergoes reactions with molecules like maleic anhydride or ethylene tetracyano, and these reactions do not require excessive energy [81–83]. The reaction between graphene and maleic anhydride occurs at 120 degrees Celsius, while at 150 degrees Celsius, the reaction is reversed, leading to the cleavage of the covalent bond. This reversed reaction is commonly referred to as retro Diels-Alder. On the other hand, ethylene tetracyano exhibits a higher degree of dienophilicity compared to maleic anhydride, enabling the reaction to occur at room temperature. In contrast, retro Diels-Alder takes place at 100 degrees Celsius.

During my Ph.D. thesis, the functionalization of graphene was carried out using diethyl maleate and acetylene dicarboxylate, which are ester derivatives of maleic anhydride. We selected these compounds due to their enhanced malleability and improved storage properties compared to maleic anhydride. Diethyl maleate, being less reactive, less toxic, and less hygroscopic than maleic anhydride, was chosen. Acetylene dicarboxylate, on the other hand, offered easier handling and storage along with excellent reactivity. Our objective was to achieve surface functionalization of graphene-like graphene oxide, which has demonstrated exceptional results in membrane design. Furthermore, the Diels-Alder reaction employed in our study resulted in fewer electronic defects on the graphene surface compared to graphene oxide.

Additionally, we functionalized graphene with ethylene tetracyano to enhance its compatibility with Polymer PIM-1, which incorporates cyano groups in its chemical structure. The inclusion of cyano groups increases the polarity of the polymer, thereby enhancing its affinity for CO_2 and improving the selectivity of the membrane. Overall, our primary aim was to develop a mixed-matrix membrane utilizing graphene as an inorganic filler. The intended outcome was a membrane that efficiently separates CO_2 from flue gases, surpassing the Robeson limit, and exhibiting superior performance in terms of both permeability and selectivity.

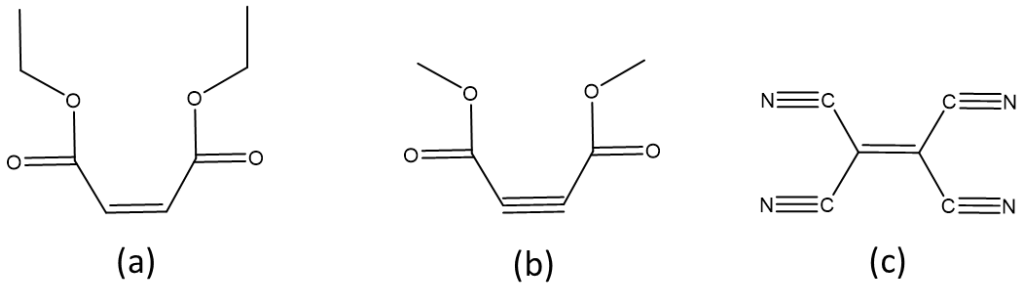

Figure 16 Molecules used to functionalize graphene, diethyl maleate (a); acetylene dicarboxylate (b); tetracyano ethylene (c).

1.3.2 Development

The functionalization of graphene with derivatives of maleic anhydride was extensively studied using a microwave reactor, leading to different outcomes that will be presented in the following paragraphs [81,82]. Notably, diethyl maleate exhibited a distinct behavior, deviating from the anticipated Diels-Alder reaction and instead forming an ethanol-dispersible nanocomposite [84]. This finding holds significant implications not only for membrane design but also for the dispersion of graphene, which conventionally relies on polar aprotic solvents like dimethylformamide (DMF), N-methyl pyrrolidone (NMP), and dimethyl sulfoxide (DMSO). However, these solvents often have high boiling points and potential toxicity, rendering them environmentally unfriendly. In this context, the use of ethanol as a dispersant emerges as a promising alternative.

In contrast, acetylene dicarboxylate successfully underwent the Diels-Alder addition reaction, allowing its investigation at various temperatures using microwave irradiation and at room temperature over an extended period. Within the scope of this thesis project, novel graphene fillers were obtained, some of which were employed in the development of mixed-matrix membranes (MMMs others

need further characterization, and have not been considered in membrane preparations. Additionally, the study explored different concentrations of graphene in PSU and incorporated an ionic liquid called butyl methyl imidazolium Succimidate (BMIM Succ) into the matrix due to its known reactivity towards CO_2.

To enhance the compatibility of graphene with PIM-1, a polymer that incorporates cyano groups in its chemical structure, graphene functionalized with ethylene tetracyano was introduced into the PIM-1 matrix. Subsequently, BMIM Succ was also incorporated. This approach aimed to amplify the membrane's affinity towards CO_2 by leveraging the polarity of the cyano groups present in PIM-1, thereby augmenting the selectivity of the membrane. Table **1** provides an overview of the different materials prepared and the MMM membranes designed in this study.

Table 1 Materials and Membranes developed in the project.

Fillers	
Exfoliated Graphene, **EG** Graphene diethyl maleate, **GEM** Graphene acetyl dicarboxylate **M(temperature °C)** Graphene Tertracyano ethylene **GTCNE**	
Polymers	
Polymer of intrinsic microporosity **PIM-1** Polysulphone **PSU** commercial	
Ionic Liquid	
Buthyl Methyl Imidazolium Succimidate ,**BMIM Succ** commercial Buthyl Methyl Imidazolium Acetate **BMIM Ac** commercial	
Membranes	
	PSU+1% EG, **PSU1G**

PSU+EG+IL	PSU+2% EG, **PSU2G** PSU+5% EG, **PSU5G** PSU+2% EG + 15% BMIM Succ, **PSU2GIL** PSU+5% EG + 15% BMIM Succ, **PSU5GIL**
PIM-1+GTCNE+IL	**PIM-1** PIM-1+ 2% GTCNE, **PIM(GTCNE)** PIM-1+ 2%GTCNE+ 15% BMIM Succ,**PIM(GTCNE)IL**
Multilayer membranes (Wafer) *And PIM-1 PSU composite*	PSU+ GEM Coated, **GM[PSU]** PSU+ PIM-1 Coated, **PIM[PSU]** PSU+ PIM(GTCNE) Coated, **PIM(GTCNE)[PSU]** 75% PSU+ 25%PIM-1 , **PSU/PIM**

Chapter 2

Materials and methods

2.1 Materials

This chapter describes the synthesis and preparation of graphene-based materials employed as fillers for mixed matrix membranes, along with their comprehensive characterization. The research encompassed the development of two novel materials: a graphene-based nanocomposite and ethylene dimaleate. A wide range of analytical techniques was utilized to analyze and assess the synthesized materials. These techniques include thermogravimetry coupled with infrared spectrometry, X-ray diffraction, ultraviolet spectrophotometry, field scanning emission microscopy and transmission electron microscopy. The graphene-based nanocomposite, functionalized through the cycloaddition of dimethyl acetyl dicarboxylate, underwent further analysis utilizing fluorometric spectrophotometry to elucidate its properties. Additionally, the graphene-based nanocomposite, functionalized with tetracyano ethylene, was subjected to characterization using thermogravimetric analysis coupled with infrared spectrometry.

2.1.1 Synthesis of exfoliated graphene (EG).

Exfoliated graphene (EG) was prepared using the methods developed by Hernandez et al. and Coleman et al. [85,86]. Natural graphite flakes with a purity ≥99% and particle size of -325 mesh (99% carbon basis) were obtained from Carlo Erba Reagents, along with N-methyl-2-pyrrolidone (NMP) of ≥99.8% purity.

The preparation of exfoliated graphene involved the use of a sonicator bath. In a glass bottle, 1.000 g of graphite and 20 mL of NMP were combined to form a suspension, which was stirred thoroughly. To maintain a temperature below 10 °C, the glass bottle was placed in the sonication bath filled with ice and water. The solution was sonicated for 40 min and then further diluted with an additional 30 mL

of NMP to achieve a 2% weight-on-volume solution of graphite in NMP. Sonication continued for another 60 min, ensuring that the temperature remained below 15 °C.

After sonication, the solution was subjected to centrifugation at a speed of 4200 rpm for 60 min. Following centrifugation, the supernatant was carefully separated and stored in a glass bottle. To ensure consistency and uniformity of the material, all exfoliated graphene samples were stored in a two-liter bottle. This approach ensured that any variations in the material prepared during each sonication were consistent throughout the entire material. Consequently, this enabled the use of uniformly equal graphene for subsequent reactions. The resulting graphene solution in NMP had an estimated concentration of 0.15 mg mL^{-1} of EG.

2.1.2 Synthesis of nanocomposite graphene-based with diethyl maleate.

Two different methods were employed to synthesize the diethyl maleate-based nanocomposite. The first method involved the use of a microwave reactor to ensure constant and uniform temperature by varying the energy of the emitted microwaves. The second method utilized azobisisobutyronitrile (AIBN) as the radical initiator.

The content set forth in this paragraph has been published as a scientific article[84].

2.1.2.1 Microwave-assisted synthesis of nanocomposite graphene-based with diethyl maleate.

The graphene and diethyl maleate-based nanocomposite synthesis was conducted using two different methods. Diethyl maleate (97%), ethanol (99.8%), chloroform (≥99%), and toluene (99.8%) were supplied by Merck, while nylon alumina membranes (Whatman Anodisc inorganic filter membrane supported, diam. 25 mm, pore size 0.02 μm) were also provided by Merck. The synthesis was performed in a Monowave 400 Anton Paar microwave reactor.

To prepare the graphene, the previously synthesized EG was sonicated for 30 min to ensure better dispersion and break up any graphene nanoparticle aggregations that may have formed during storage. After sonication, 200 mL of the EG solution was filtered using a vacuum filtration system with a nylon membrane having a pore size of approximately 0.2 microns. The filtrate was then washed with 50 mL of ethanol, resulting in the isolation of 30 mg of graphene.

Subsequently, the graphene-coated nylon membrane was placed in a glass sample reactor specifically designed for the Anton Paar microwave reactor, which had a capacity of 30 mL and a soft silicone septum cap capable of withstanding pressures up to 5 bar. To disperse the exfoliated graphene in toluene, 10 mL of toluene and a magnetic anchor were added to the reactor. The sample was then placed in a sonicator bath for 10 min. After this step, the membrane was removed from the reactor, leaving the graphene dispersed in the toluene.

Since graphene is not soluble in toluene and tends to precipitate, the solution was kept under continuous stirring. N_2 gas was introduced into the solution to remove traces of air and maintain an inert atmosphere within the system. After 10 min, 1.0 g (0.0058 mmol) of diethyl maleate, which had been previously distilled and stored in the freezer, was added. Following the addition of diethyl maleate, the N_2 flow was discontinued, and the reactor was placed in the Anton Parr microwave reactor for 60 min at 125°C.

The synthesis of the graphene-ethylene dimaleate (GEM) nanocomposite using the microwave reactor is illustrated in Figure **17**:

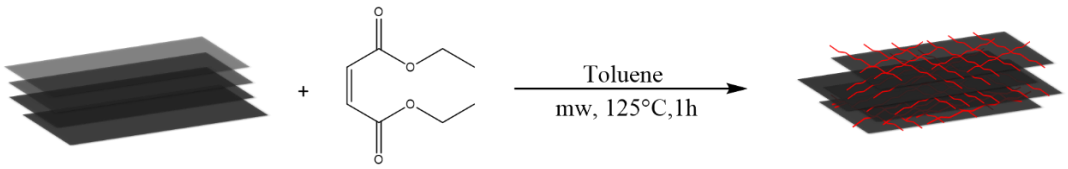

Figure 17 Reaction scheme of GEM synthesis.

Once the reaction was completed, the solution was filtered using a vacuum filtration system with an alumina membrane having an average pore size of 0.02 microns. The filtrate was washed first with ethanol and then with chloroform to remove unbound polymers from the graphene surface and excess diethyl maleate. The filtrate, along with the filter, was dried overnight in a vacuum oven.

2.1.2.2 Synthesis of nanocomposite graphene-based with diethyl maleate AIBN assisted.

To synthesize the GEM nanocomposite using the AIBN radical initiator and transfer agent, the procedure was repeated with the addition of 0.190 g (0.00116 mol) of AIBN. Initially, the graphene was washed with 50 ml of ethanol and then redispersed in toluene. Subsequently, 1.0 g (0.0058 mmol) of diethyl maleate was added to 10 ml of the toluene solution containing exfoliated graphene (EG) under a

N_2 atmosphere. The amount of AIBN added was 20% mol relative to the diethyl maleate. Once again, the graphene was washed with 50 ml of ethanol and redispersed in toluene for further processing.

2.1.3 Synthesis of graphene functionalized with dimethyl acetyl dicarboxylate (M).

Different routes were studied for the preparation of the following material, including room temperature overnight and the use of a microwave reactor with varying temperatures and solvents. In the following paragraphs, the method processed in a microwave and the method at room temperature will be presented separately.

2.1.3.1 Synthesis of microwave-assisted graphene functionalized with dimethyl acetyl dicarboxylate (M).

Dimethyl acetyl dicarboxylate (97%), ethanol (99.8%), chloroform (≥99%), and toluene (99.8%) were supplied by Merck, while nylon membranes (Whatman membrane filters nylon pore size 0.2 μm, diam. 25 mm) and alumina membranes (Whatman Anodisc inorganic filter membrane supported, diam. 25 mm, pore size 0.02 μm) were also provided by Merck. The synthesis was performed in a Monowave 400 Anton Paar microwave reactor

The starting point for all reactions was a solution of 200 mL of EG that was filtered. After filtration, the solution was washed with 50 mL of ethanol and 50 mL of chloroform, and the graphene was allowed to dry overnight, yielding 30 mg of the material. 30 mg of graphene and 0.015 mol of methyl acetyl dicarboxylate were dispersed in 10 mL of toluene with the help of 10 min of sonication in a glass vial designed for use in the Anton Parr microwave reactor. N_2 was then insufflated into the system to create an inert atmosphere. The Diels-Alder cycloaddition reaction was carried out using the microwave reactor and is represented by the following reaction Figure **18**.

The microwave reactor was studied at different temperatures bu at the same time 1.00 h,

Table 2 lists the reactions done in the microwave.

Table 2 reaction with microwave reactor.

Name	**Solvent**	**Temperature**	**Time**
M60	Toluene	60°C	1h
M125	Toluene	125°C	1h
M135	Toluene	135°C	1h
M175	Toluene	175 °C	1h

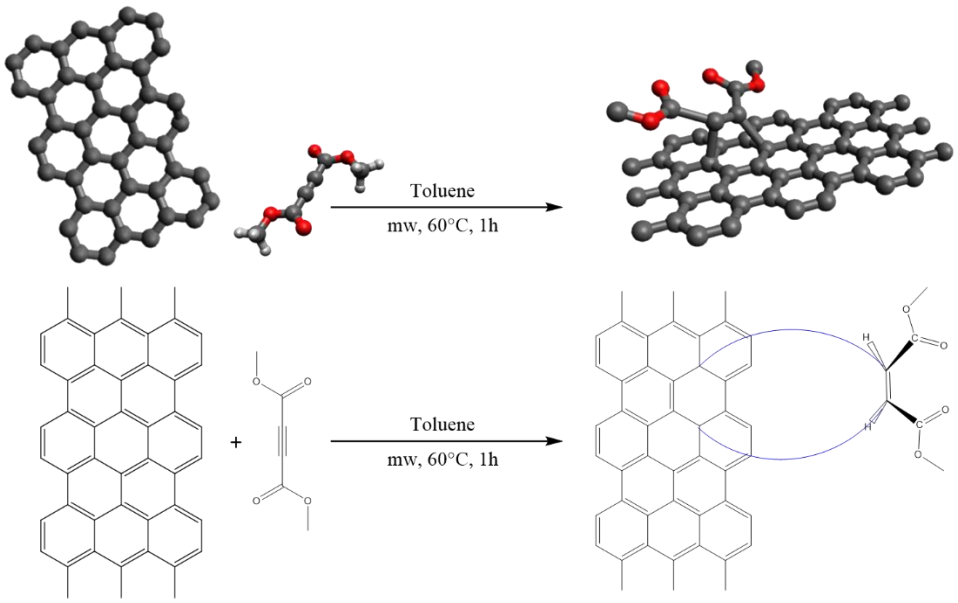

Figure 18 Diels Alder reaction between graphene and acetyl dicarboxylate

2.1.3.2 Synthesis of graphene functionalized with dimethyl acetyl dicarboxylate at room temperature.

Dimethyl acetyl dicarboxylate (97%), ethanol (99.8%), chloroform (≥99%), and Dichloromethane (99.8%), Dioxane(≥99%), were supplied by Merck, while nylon membranes (Whatman membrane filters nylon pore size 0.2 μm, diam. 25 mm) and alumina membranes (Whatman Anodisc inorganic filter membrane supported, diam. 25 mm, pore size 0.02 μm) were also provided by Merck.

The following reactions were done at room temperature using two different types of solvents, one in CH_2Cl_2/Dioxane, the other using Toluene as the solvent, and the same one used in the microwave reactions. below will be presented the reaction done with the CH_2Cl_2/Dioxane 50:50 mixture, the two reactions, excluding the solvent, appear to be identical in reaction conditions such as time, and temperature. Table **3**

200 mL of exfoliated graphene was filtered with the use of a filtration system and a holder in a filter after the solution was filtered 50 mL of ethanol was poured in, followed by 50 mL of chloroform. after the washes with the two solvents, the graphene was allowed to dry overnight, eventually obtaining 30 mg of graphene.

30 mg of graphene was dispersed in 10 mL of dioxane and dichloromethane 50:50 to the solution were added 0.015 mol of dimethyl acetyl dicarboxylate. the solution was left to stir overnight. the next day the reaction was stopped, and the solution was filtered using an alumina filter on a vacuum filtration system, washed the filtrate with 50 mL of chloroform, and put the filtrate to dry.

Table 3 lists reactions made at room temperature.

Name	Temperature	solvent	time
Mrt	RT	Toluene	8-12 h
Mrt_cd	RT	CH2Cl2/Dioxane 50:50	8-12 h

2.1.4 Synthesis of graphene functionalized with tetracyanoethylene.

Tetracyano ethylene (97%), ethanol (99.8%), chloroform (≥99%), and Dichloromethane (99.8%), Dioxane(≥99%), were supplied by Merck, while nylon membranes (Whatman membrane filters nylon pore size 0.2 μm, diam. 25 mm) and

alumina membranes (Whatman Anodisc inorganic filter membrane supported, diam. 25 mm, pore size 0.02 μm) were also provided by Merck.

The synthesis of graphene functionalized with tetracyanoethylene (TCNE) is based on the studies conducted by Sarkar et al. [82].

Initially, 200 mL of exfoliated graphene was filtered using a filtration system with a filter media. After filtration, 50 mL of ethanol was added, followed by 50 mL of chloroform for thorough washing. The washed graphene was then left to dry overnight, resulting in the production of 30 mg of graphene.

Next, 30 mg of the filtered and dried graphene was dispersed by sonication in a sonicator bath for 10 min, using a mixture of 50% dioxane and 50% dichloromethane (10 mL). The Diels-Alder reaction that occurred is represented in Figure 19.

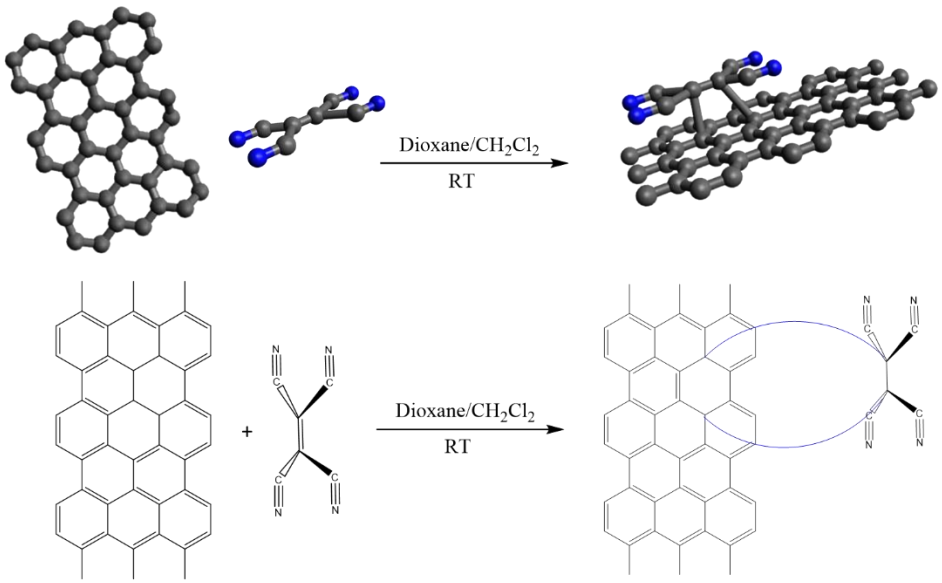

Figure 19: Diels-Alder reaction between TCNE and Graphene.

To the solution containing the dispersed graphene, approximately 0.0016 mol of tetracyanoethylene equivalent to 200 mg, was gradually added. N_2 was then fluxed into the solution for 10 min.

The solution was left to stir overnight. After completing the stirring process, the dispersion was filtered using a vacuum filtration system with an alumina membrane, which had an average pore size of 0.02 micrometers. The filtered

graphene was washed with chloroform and ethanol to ensure the removal of any unreacted dioxane and tetracyanoethylene impurities. Following filtration, the graphene was dried in a vacuum oven at a temperature of 40°C overnight, while the filtrate was easily separated from the alumina membrane.

2.1.5 Synthesis of PIM-1

3,3,3′,3′-Tetramethyl-1,1′-spirobiindane-5,5′,6,6′-tetraol (97%), dimethyl formamide (≥99%), anhydrous K_2CO_3, were supplied by Merck, were purchased from FluoroChem.

PIM-1 polymer synthesis was conducted following the procedure developed by Budd et al. [87] , as depicted in Figure 20.

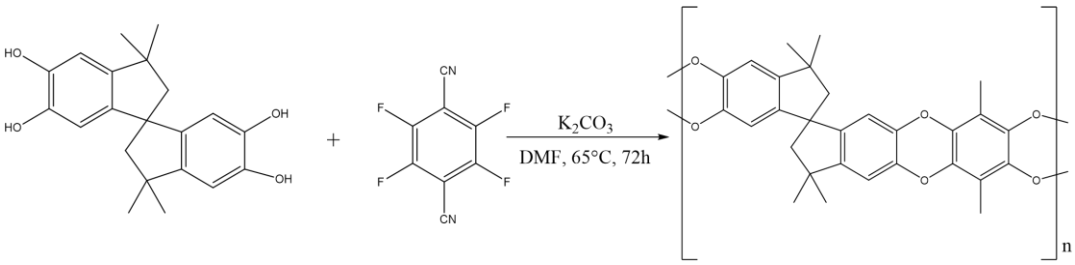

Figure 20 PIM-1 synthesis

60 mL of dimethyl formamide (DMF) was combined with 0.008813 moles of 3,3,3′,3′-Tetramethyl-1,1′-spirobiindane-5,5′,6,6′-tetraol (340.41 g mol^{-1}), which is equivalent to 3 g, and 0.008813 moles of 2,3,5,6-Tetrafluoroterephthalonitrile (200.096 g mol^{-1}), equivalent to 1.76 g.

Subsequently, 5.53 g of anhydrous K_2CO_3 was added to the mixture, and the system was purged with N_2 to establish an inert atmosphere. The prepared mixture was then stirred for 72 h at 65°C under a N_2 environment.

After 72 h, 400 mL of distilled water was introduced into the solution, causing the polymer to precipitate. The solution containing the precipitate was subjected to centrifugation and underwent multiple cycles of centrifugation and dispersion. In each cycle, the supernatant was removed, and water followed by methanol was used for washing.

Following the washing cycles, the precipitate was dried in a vacuum oven overnight at 40°C.

Upon drying, the polymer appeared as a bright yellow solid powder. Notably, this polymer exhibits solubility in chloroform, DMF, and NMP.

2.1.6 Preparation of PSU membrane with EG and BMIM Succ.

PSU average Mw ~35,000 by LS, average Mn ~16,000 by MO, pellets (Transparent), N-methyl-pyrrolidone (99.7%) were purchased by Merck [BMIM] [Succ] were received from Iolitec. The exfoliated graphene was prepared such as the paragraph 2.1. Membranes were stretched by the use of an Automatic film applicator, ATX, Neurtek, presetting the thickness to 200 μm on a glass support.

PSU membranes were prepared by incorporating 1%, 2%, and 5% BMIM Suc concerning total membrane weight. Additionally, two membranes were prepared with 2% and 5% EG of the total membrane weight, along with 5% of the total membrane weight (PSU:IL: EG) of BMIM Suc. The amount of NMP solvent was calculated to achieve a 25% PSU polymer-to-solvent solution ratio (PSU: NMP = 25:100) as shown in (Table 4).

Table 4 quantity as a percentage of the individual components of a membrane.

Membrane	**Weight % of the compound in the polymeric solution**			
	PSU % (w/v) (PSU: NMP)	**IL % (w/w) (PSU:IL:EG)**	**Graphene % (w/w) (PSU:IL: EG)**	**NMP % (w/v) (PSU: NMP)**
PSU	25%	5%	0	75%
PSU1G	25%	0	1%	75%
PSU2G	25%	0	2%	75%
PSU5G	25%	0	5 %	75%
PSU2GIL	25%	5%	2%	75%
PSU5GIL	25%	5%	5%	75%

The membranes were prepared using the solvent evaporation technique, wherein the polymer is dissolved in a solvent, applied onto a specific substrate, and left to evaporate, resulting in solidification.

To begin, 3.0 mg of graphene was dispersed in 2 mL of NMP using a sonication bath. After 5 min of sonication, 500.0 mg of PSU and 3.0 mg of BMIM Suc were added to the NMP-graphene solution. The solution was stirred until the polymer completely dissolved in the solvent. Once the polymer was fully dissolved, the stirring was stopped, and the solution was allowed to rest overnight to eliminate any microbubbles.

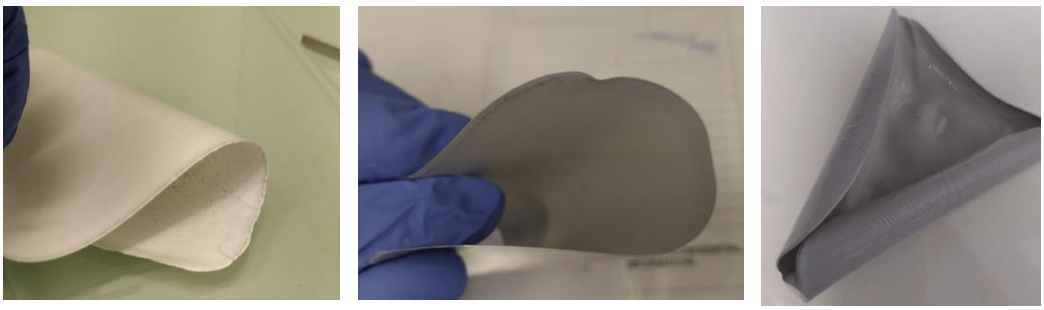

(a) (b) (c)

Figure 21 PSU Membrane with 1% (a), 2%(b), and 5%(c) of EG

The following day, the solution was sonicated for 30 to 40 min to ensure uniform dispersion of graphene and minimize the presence of graphene aggregates within the polymer matrix. After sonication, the polymer solution was spread onto a glass plate using an automatic spreader. A spreading thickness of 200 microns was maintained by using a blade, and the spreading was performed at a moderate speed. Once the viscous solution was evenly spread on the glass substrate, it was placed under a fume hood to allow for slow solvent evaporation, promoting orderly solidification of the polymer. When the membrane was completely solidified, it spontaneously detached from the substrate.

2.1.7 Preparation of PIM-1 membrane with G(TCNE) and BMIM Suc.

PIM-1 and GTCNE were previously synthesized as reported in section 2.4 2.5; [BMIM] [Succ] were received from Iolitec. Membranes were stretched by the use of an Automatic film applicator, ATX, Neurtek, presetting the thickness to 100 μm.

Based on the results obtained with PSU, it was determined to incorporate 2% by weight of TCNE in the total membrane composition. Additionally, a PIM-1 membrane was prepared with 5% of the total membrane mass consisting of an ionic liquid. However, it was not feasible to combine BMIM Suc and G(TCNE) due to the precipitation of G(TCNE) (and other types of graphene) caused by the presence of the ionic liquid. The prepared membranes are summarized in Table 5.

Figure 22 PIM-1 GTNE BMIM Scu membrane.

Table 5 description of the composition of different membranes based on PIM-1.

Membrane	**Weight % of the compound in the polymeric solution**			
	PIM-1 % (w/v) (PIM-1:$CHCl_3$)	**IL % (w/w) (PIM-1:IL:EG)**	**EG % (w/w) (PIM-1:IL:EG)**	**$CHCl_3$ % (w/w) (PIM-1:$CHCl_3$)**
PIM-1	50%	0%	0	50%
PIM(GTCNE)	50%	0	2%	50%
PIM(GTCNE)IL	50%	5%	2%	50%

The preparation of membrane containing PIM-1, 2% G(TCNE), and 5% BMIM Succ is described below.

500 mg of PIM-1 was dissolved in 500 mg of $CHCl_3$ under stirring. Unlike the solutions prepared with PSU, this solution is not very viscous. Next, 27.0 mg of BMIM Suc was added to the solution. Once the solution became homogeneous, 10.0 mg (2% of the total membrane) of G(TCNE) was added. The solution containing G(TCNE) was sonicated in a sonication bath for 1 h. Since graphene disperses poorly in chloroform, a longer sonication time is required to achieve a homogeneous dispersion of the carbonaceous nanomaterial in the polymer matrix.

After completing the sonication-assisted dispersion, the solution was applied to a glass substrate using an automatic blade, ensuring a thickness of 200 micrometers.

Due to the lower viscosity of the solution compared to the PSU-NMP solution, there is no need to allow the solution to rest and eliminate microbubbles caused by stirring.

The rapid evaporation of chloroform facilitates quick membrane formation, while also maintaining excellent dispersion of graphene. The resulting membranes exhibit an average thickness of about 22 micrometers.

2.1.8 Preparation of Multilayer membranes and PSU/PIM-1 composites.

PSU average Mw ~35,000 by LS, average Mn ~16,000 by MO, pellets (Transparent) were purchased by Merck, PIM-1, GEM, and PIMGTCNE was previously synthesized as reported in sections2.2, 2.4, 2.5, The airbrush was recovered from Wiltec with a 10 mL tank and connected to inert gas N_2.

Multilayer or wafer membranes, composed of PSU membranes coated with a layer of polymer or graphene, were developed to investigate the mutual influence of the two layers on permeability, diffusion, and solubility. Three types of these membranes were prepared: PSU/PIM-1, PSU/GEM, and PSU/PIM-1_GTCNE, each representing a different combination of layers.

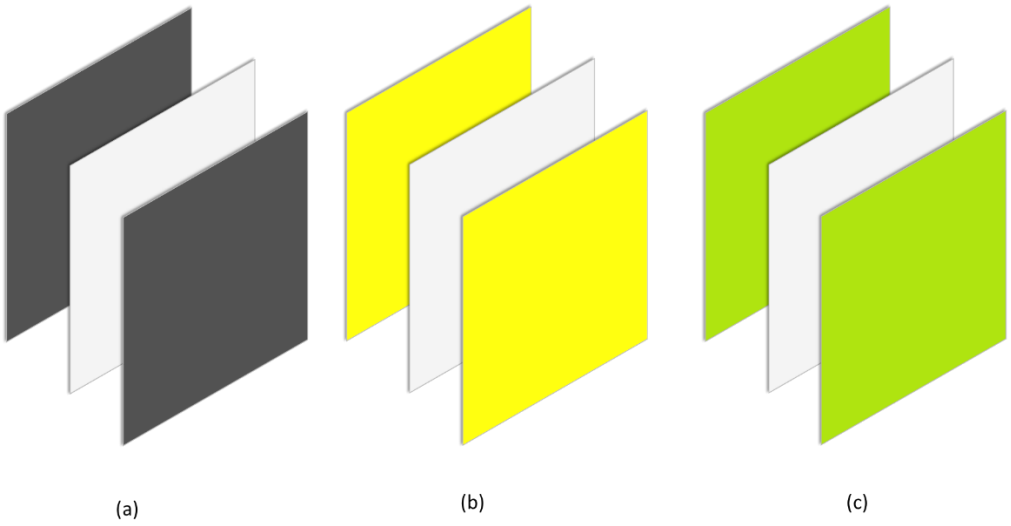

Figure 23 Models of multilayer membrane coated with GEM (a) with PIM-1(b) and PIMGTCNE(c).

Membranes comprising PSU and PIM-1 or PIM-1 GTCNE were prepared by layering a PSU membrane, following the previously described procedure. Using an airbrush, a layer of PIM-1 or PIM-1 GTCNE was applied to the membrane. A solution of 50 mg of PIM-1 or PIM-1 GTCNE in 10 mL of chloroform was used for the coating. Since PSU is soluble in chloroform, the PSU membrane was first washed with ethanol and then treated with the solvent in a controlled manner. The chloroform was sprayed at regular intervals, allowing sufficient time for evaporation between sprays to prevent excessive accumulation and damage to the PSU membrane.

Figure 24 PSU coated with GEM using the airbrush.

To apply the graphene maleate coating, 30 mg of GEM was dispersed in 10 mL of ethanol using 10 min of sonication. Since the PSU membrane is inert to ethanol, the spraying process was easily performed without any adverse effects on the membrane. The graphene coating remained stable on the membrane surface.

For the preparation of a PSU/PIM-1 composite membrane weighing 500 mg, a solution was made using 375 mg of PSU and 125 mg of PIM-1 dissolved in 1.84 mL of NMP. This composition resulted in a composite membrane with 25% PIM-1 and 75% PSU. The amount of NMP was calculated to achieve a PSU concentration of 20% in the solution.

After ensuring the complete dissolution of the polymers in the solution, it was left to rest overnight to allow the dissipation of any microbubbles that may have formed during mixing. The following day, the solution was spread onto a glass

substrate using a mechanical blade set at a thickness of 200 microns. The spread membrane was then left to dry overnight under a fume hood.

2.1.9 Preparation of Composite membrane PIM-1 with Ionic liquids BMIMSucc and BMIM acetate

The content set forth in this paragraph has been published as a scientific article[88].

PIM-1 was previously synthesized as reported in section 2.5; ILs [BMIM] [Ac] and [BMIM] [Succ] were received from Iolitec. All the other reagents and solvents were purchased from Merk-Sigma-Aldrich.

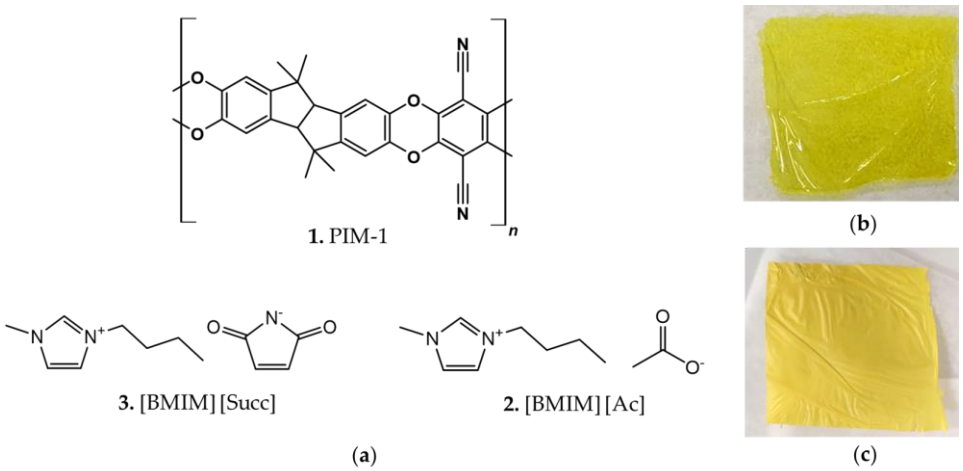

Figure 25 a) Molecular structures of PIM-1 (1), 1-Butyl-3-methylimidazolium succinimidate [BMIM][Succ] (2) and 1 -Butyl-3-methylimidazolium acetate [BMIM][Ac]; (b) Self-standing PIM-1 membrane; (c) Self-standing PIM-1/[BMIM][Succ] 50% membrane.

PIM-1/ILs membranes were prepared by a solvent evaporation method. PIM-1 was first dissolved in chloroform and stirred for 15 min at 40°C. Subsequently, IL was added to the solution and stirred for 15 min at 40°C. PIM-1 and ILs films were prepared with a total of 2 wt% polymer concentration in chloroform. The blend ratio of PIM-1/IL contents varies from 10%, 25%, and 50% were IL is [BMIM][Ac] or [BMIM][Succ].The blended solution was cast onto a leveled nylon substrate at ambient temperature. The polymer films were formed after the evaporation of the solvent. The resultant membranes were dried at 40 °C under vacuum for at least 16 h to remove the remained traces of solvent. The membranes were labeled as "PIM-1/IL ratio composition", for example, PIM-1/[BMIM][Ac] 10%. The thicknesses of the casted films were around 1 μm, while the densities were between 0.979 and 1.955 (g/cm3).

2.2 Instruments

2.2.2 Thermo-gravimetric analysis (TGA-IR)

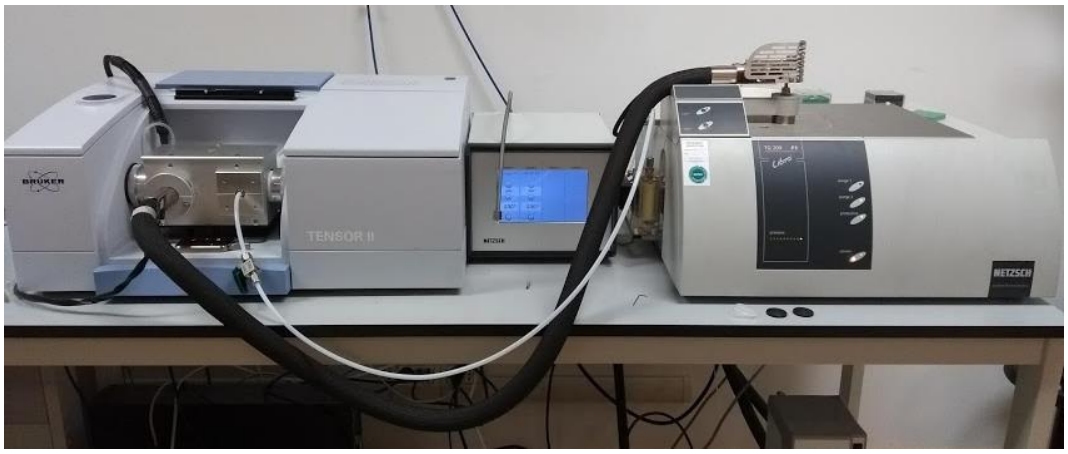

Figure 26: Thermo-gravimetric analyzer coupled with infrared spectrometer a Right: TGA instrument; left: IR spectrometer equipped connection for gas-phase transmission of decomposition products; center: heated transfer line and temperature controller.

Thermal gravimetric analysis coupled with infrared spectrometry was conducted to analyze all fillers and membranes. The analysis, known as TGA-IR, was performed using a Thermo-gravimetric Analyzer (NETZSCH TG 209 F1) coupled with an Infrared spectrometer (Bruker TENSOR II). The transfer line was heated at 230 °C, and the IR gas cell was heated at 200 °C. The samples (approximately 3 mg) were heated from 30°C to 800°C at a rate of 20 °K min-1 in alumina pans, under a N_2 flow of 40 ml min^{-1}. Before the test, three vacuum cycles were conducted to remove air and eliminate solvent impurities from the material's surface. The experimental weight error is within ±1%. FTIR analysis was performed in the absorbance mode within the range of 650 – 4400 cm^{-1}. Each filler had an initial weight ranging between 2 mg and 3 mg, while each membrane had an initial weight between 10 mg and 12 mg.

2.2.2 FT-IR spectroscopy

Membrane composites with PSU BMIMSucc and EG, PIM-1 polymer, and membrane PIM-1 based with BMIM Succ and GTCNE have been studied via Fourier transform infrared (FT-IR) spectroscopy. The measurement was carried out

on a Bruker Invenio spectrophotometer equipped with a mercury-cadmium-telluride (MCT) detector.

2.2.4 Differential scanning calorimetry

PSU membranes were carried out with Differential Scanning Calorimetry, DSC DSC822, and Mettler-Toledo, The tests were performed three cycles of heating and cooling was performed from 50 to 250 °C with a rate of 10 $Kmin^{-1}$ about 5 mg sample in aluminum pans.

2.2.5 Raman

Raman characterization was performed using a Renishaw In Via micro-Raman spectrometer, equipped with a cooled CCD camera. A laser diode source ($\lambda = 514.5$ nm) was used with 5 mW power, and sample inspection occurred through a micro-scope objective (50×), with a backscattering light collection setup. Measurements are collected with a fast acquisition time (2 s) and are an average of 50 accumulations.

2.2.6 XPS

X-ray Photoelectron Spectroscopy was carried out with a PHI 5000 Versaprobe spectrometer (monochromatic Al K-alpha X-ray source, 1486.6 eV energy) over 500 μm x 500 μm areas of interest. The following pass energy values were used: 187.85 eV for survey spectra and 23.5 eV for high-resolution scans. A combined electron and argon ion gun neutralizer system was used for charge compensation during the acquisitions. The analysis of experimental data was performed with CasaXPS software. The binding energy scale was calibrated by placing the C-C sp^2 component at 284.5 eV, using a LF(0.6, 1, 255, 350, 6) asymmetric line-shape as provided in CasaXPS

2.2.7 XRD

A PANalytical X'Pert MRD Pro powder diffractometer equipped using the 1D PIXcel detector was employed for the X-ray diffraction analysis (Malvern PANalytical, the United Kingdom). The patterns were collected in Bragg-Brentano reflection mode by using Cu Kα1/2 radiation, at an operating voltage of 40 kV and a tube current of 40 mA.

The instrumental broadening was determined by fitting of PseudoVoigt functions to line profiles of a standard LaB6 powder NIST660c. The measurements were carried out in continuous mode with a step size of $2\theta = 0.0131°$ and a data time per step of 150 s for the Sigma-Aldrich and 300 s for the membranes. QualX software with COD-database was employed for the qualitative phase determination and MAUD free software for the quantitative analysis and refinement. The COD cards matching the diffraction patterns are the numbers 00-900-8569 (space group P 63 m c) and 00-901-2705 (space group R -3 m).

2.2.8 Gas solubility, diffusion, and permeability measurement.

Figure 27 Dynamic Vapor Sorption vacuum experimental apparatus

Solubility, diffusion, and permeability measurements were carried out through the Dynamic Vapor Sorption vacuum experimental apparatus (DVS) by Surface Measurement Systems Limited. This technology can perform several kinds of measurements related to adsorption and desorption under static and dynamic conditions providing dynamic data suitable for diffusion coefficient calculation.

In the DVS application measuring diffusivity in 5 membranes disc with a diameter of 0.55 cm per disk, a constant diffusion and a constant source concentration were assumed. Fick's second law of diffusion, describing non-steady-state mass transfer, in spherical coordinates reads [89]:

$$\frac{\partial C}{\partial t} = \frac{1}{r^2}\frac{\partial}{\partial r}\left(Dr^2\frac{\partial C}{\partial r}\right)$$

Eq 10

where D is the diffusion coefficient; C is the concentration of the solute and r is the distance from the center of the sample.

The concentration is linked to the mass of gas diffused (M) by:

$$M = \int_V CdV$$

Eq 11

By assuming that the membrane's samples are disks with a uniform radius r_p and with the boundary condition $\frac{\partial C}{\partial r}$= 0 at r= 0, , Eq 10 has the following solution, under isothermal conditions [89].

$$\frac{M_t}{M_\infty} = 1 - \frac{6}{\pi^2}\sum_{n=1}^{\infty}\frac{1}{n^2}exp\left(-\frac{n^2\pi^2 Dt}{r_P^2}\right)$$

Eq 12

Where M_t is the gas mass uptake adsorbed/desorbed at a given time t and M_∞ the gas mass uptake at the equilibrium. The uptake mass is calculated by subtracting the initial mass (m_0) from the mass recorded at each time For short times, Eq **12** can be reduced to a simplified form:

$$\frac{M_t}{M_\infty} = \frac{6}{r_p}\left(\frac{Dt}{\pi}\right)^{0.5}$$

Eq 13

From Eq **13** follows that the slope of the plot $\frac{M_t}{M_\infty}$ vs $\sqrt{t}$ gives the diffusion coefficient.

$$slope = \frac{6}{r_p}\sqrt{\frac{D}{\pi}}$$

Eq 14

Eventually, the diffusion coefficient is evaluated by

$$D = \frac{slope^2 d\pi}{16}$$

Eq 15

The procedure can be exploited for increasing levels of partial pressure (% P/P_0), i.e. for increasing available adsorbate mass, thus obtaining several diffusion constants corresponding to different % P/P_0 levels This allows one to verify the assumption of weak dependence of diffusion constant upon the concentration of present gas.

Data processing

This allows one to verify the assumption of weak dependence of diffusion constant upon the concentration of present gas ($_{measured}$) is the superposition of mass measured at vacuum (m_0) called reference mass, and adsorbed gas (m_{gas})

$$m_{measured}(t) = m_0 + m_{gas}$$

However, measurements may be affected by buoyancy effects and overshooting/undershooting effects due to pressure transient [90]

$$m_{measured}(t) = m_0 + m_{gas}(t) - m_{bouyancy}(t) + m_{overshooting}(t)$$

Buoyancy is the upward force, exerted by the gas filling the balance chamber, that opposes the weight of the fully immersed sample. As a result, the weight measurement decreases the quantity $m_{bouyancy}$ proportional to the partial pressure $P_p(t)$ following Archimedes principle:

$$m_{bouyancy}(t) = \rho_g V_{membrane} P_p(t)$$

Where ρ_g ist the gas density and V_s is the sample volume. If the volume is not easily computable, as in the case of flakes characterized by irregular geometry, it

can be estimated from the ratio between mass at vacuum (m_0) and membrane density ($\rho_{membrane}$):

$$V_{membrane} = \frac{m_0}{\rho_{membrane}}$$

Buoyancy effects on the sample holder are already accounted for by the balance, in which a second empty sample pan allows for continuous tare measurement.

Any partial pressure variation from one step to the subsequent (e.g., from vacuum to pp=20%) cannot occur instantaneously inside the DVS and requires a transient period in which the partial pressure variation is a function of the gas inflow rate (0.13 l/min). This means that the pressure transient duration increases with the variation of partial pressure from about 1.5 min (from 0 to 20%) to 6 min (from 0% to 80%).

During the pressure transient, short-lived flow perturbations in the chamber take place while gas is entering the camber. Consequently, immediately after a step change in the chamber pressure, a temporary fluctuation in the weight measure occurs in the form of an overshoot/undershoot. This fluctuation has no impact on the equilibrium adsorption estimate, but it does affect the short-term sorption investigation, which is involved in diffusion calculation. Therefore, a correction should be introduced to each change of partial pressure step. To this end, a test with an empty pan called a "blank run", has to be performed to isolate the overshooting/undershooting behavior ($m_{overshooting}(t)$)corresponding to the imposed partial pressure steps (Wang et al., 2017). The blank run consists in running a test applying the same gas mixture and the same partial pressure steps of the test to be corrected but testing the empty pan instead of the sample. In such a way, the mass variations measured during the blank test represent the flow perturbations due to the pressure transient only. The duration of partial pressure steps could be shorter for a blank run than for the corresponding test with the sample because mass can stabilize faster since there is no adsorption process. The signal due to the pure overshooting ($m_{overshooting}(t)$) can therefore be isolated for each partial pressure step to provide the correction to be applied to the actual measurements.

To sum up, before interpretation, data have to be corrected as follows:

$$m_{gas}(t) = m_{measured}(t) - m_0 + \rho_g V_s P_p(t) - m_{overshooting}(t)$$

Afterward, mass uptake (M_t) and equilibrium mass uptake (M_∞) are calculated respectively by:

$$M_t = m_{gas}(t)$$

$$M_\infty = m_{gas}\,(t_\infty)$$

Where $m_{gas}(t)$ the mass is measured at each time and $m_{gas}(t_\infty)$ is the mass measured at the equilibrium. In most cases, the equilibrium is not completely reached. Mass changes toward the equilibrium are usually very low, near the DVS accuracy. Thus, the partial pressure step is stopped when $\frac{dm}{dt} < 0.001 mg/s$ and the last registered mass for each partial pressure step is assumed to be a good approximation of the equilibrium mass.

Successively the $\frac{M_t}{M_\infty}$ vs $\sqrt{t}$ plot is obtained for each partial pressure step and the corresponding diffusivity coefficient is calculated as described in the "Theoretical background" section. Slopes are obtained by linear regression of selected portions of data that exhibit a linear trend at early times.

2.2.9 FE-SEM

The morphological analysis was performed using a Zeiss Auriga dual-beam FIB-SEM microscope. Concerning sample preparation, EG and GEM samples were dispersed in ethanol and subsequently drop-casted on Cu lacey carbon TEM grids.

All membranes were studied using copper support and placed vertically so that the cross-sectional area of the membrane could be studied. The specimens were pretreated by fracturing the membrane with liquid N_2 and attached to the copper support by carbon tape

2.2.10 E-SEM

The morphological analysis was performed by means of an ESEM FEI Quanta model 600 electron microscope.

All membranes were studied by employing aluminum support, placed vertically so that the cross-section of the membrane could be studied. PSU-based samples were pretreated by fracturing the membrane with liquid N_2 and attached to the aluminum

support by carbon tape, PIM-1-based samples were prepared by using cryostat microtome and attached to the aluminum support by carbon tape

2.2.11 Zeta potential

The surface chemical properties of GEM were investigated by Z potential measurements in ethanol solutions with a GEM concentration of 0.05 mg/mL by Zetasizer Nano ZS90 (Malvern Panalytical, Malvern, UK).

2.2.1.2 Thickness measurements

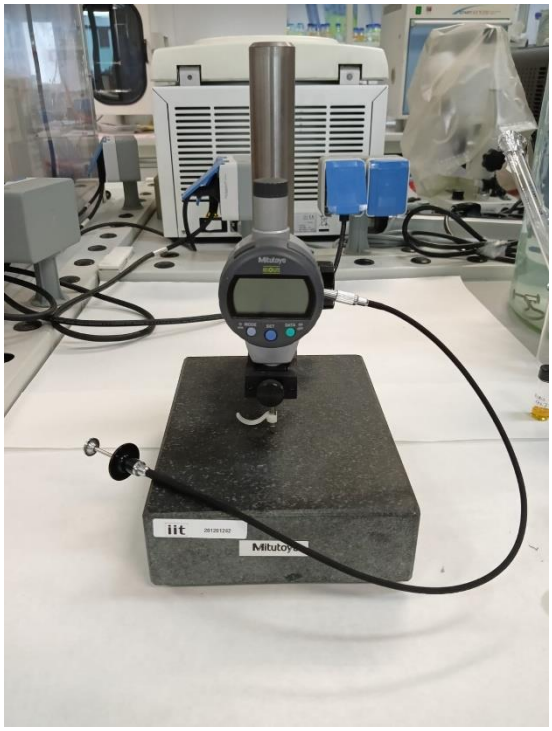

Figure 28 Thickness gauge

The thickness of the membranes were made by using a Multytoyo Absolute gravity thickness gauge was measured by preparing 5 discs with a diameter of 0.95 and measuring at 5 different points per disc, in order to obtain an average value of the membrane to total. The values of thickness, volume, and density will be reported in section 4.1.1 Table **13**

Chapter 3

Results and Discussion: Materials

This chapter will describe and discuss the qualitative characteristics observed from graphene-based fillers prepared in the laboratory, successively the PIM_1 Matrix synthesized in the laboratory will be discussed, and data regarding THE commercial PSU can be found in Chapter 2

3.1 Fillers

3.1.1 Exfoliated Graphene

Figure 29 presents a comparison between graphite and EG. By closely examining the thermogravimetric analysis of the EG and the initial graphite from which it was derived, it becomes evident that there is a mass loss during the temperature increase in the analysis. In theory, one would expect EG to be degradation-resistant, especially considering that the analyses were conducted in an inert atmosphere and graphene possesses excellent thermal conductivity.

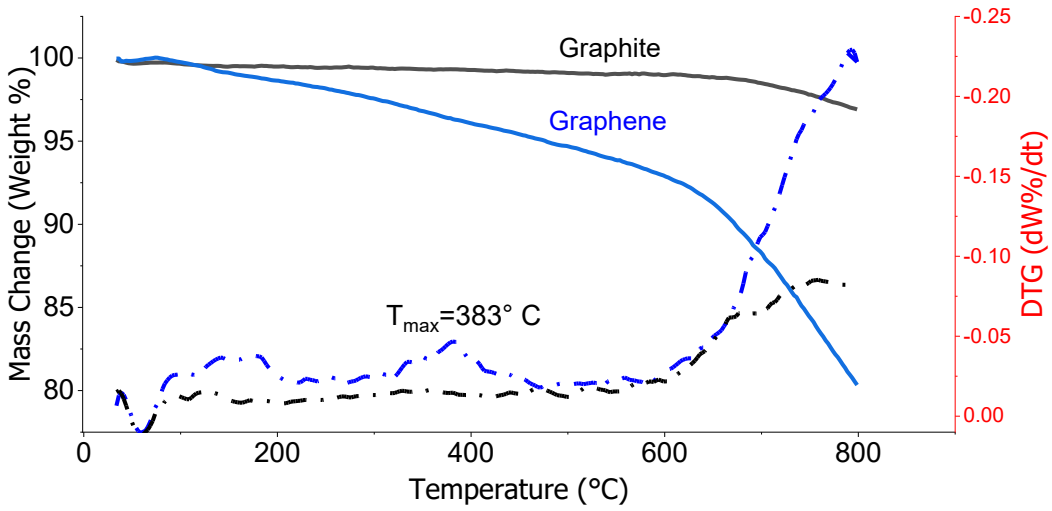

Figure 29 Comparison of TG analysis of Graphene and Graphite.

The slight mass loss (approximately 7% by weight) (Figure 29) can be attributed to two factors. Firstly, during the sonication-assisted exfoliation of graphite in NMP, the graphite layers are dispersed into smaller and simpler layers of graphene. Simultaneously, NMP adsorbs onto the surface and in the spaces between the graphene layers through pi-pi interactions, remaining on the graphene surface. Secondly, the formation of microbubbles during sonication results in the generation of oxidized carbon species on the graphene surface. These species are naturally present to some extent on graphite and contribute to the weight loss observed around 700 degrees for graphite. However, this loss is more pronounced in graphene (Figure 30a) due to the increased presence of oxidized species resulting from the exfoliation process [72,91] Indeed, these hypotheses are confirmed from the development of organic residues assessed by the infrared spectra of developed gases at 360 °C (Figure 30b) where organic solvent C-H stretching at 2970 cm^{-1} and C-H rocking at 1050 cm^{-1}, CO_2 main stretching at 2360 cm^{-1} and H_2O presences derived from oxidized graphite degradation are individuated. The intensities of the stretching peaks in the function of degradation temperature assessed the production of these molecules during the whole TG analyses (Figure 30c)

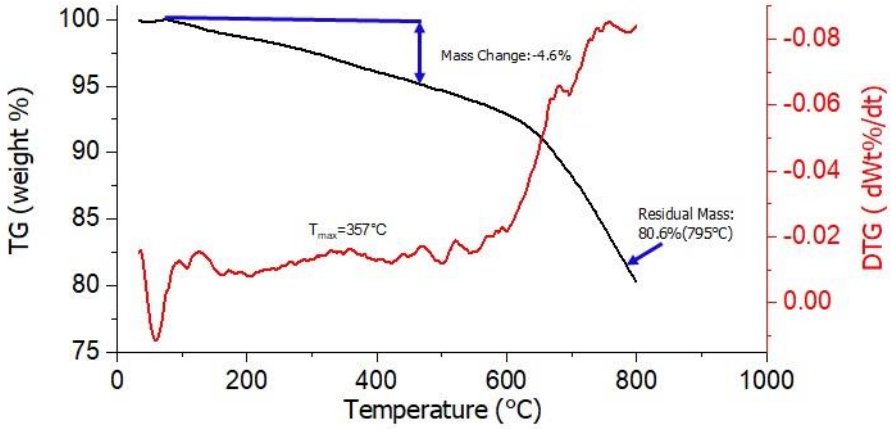

(a)

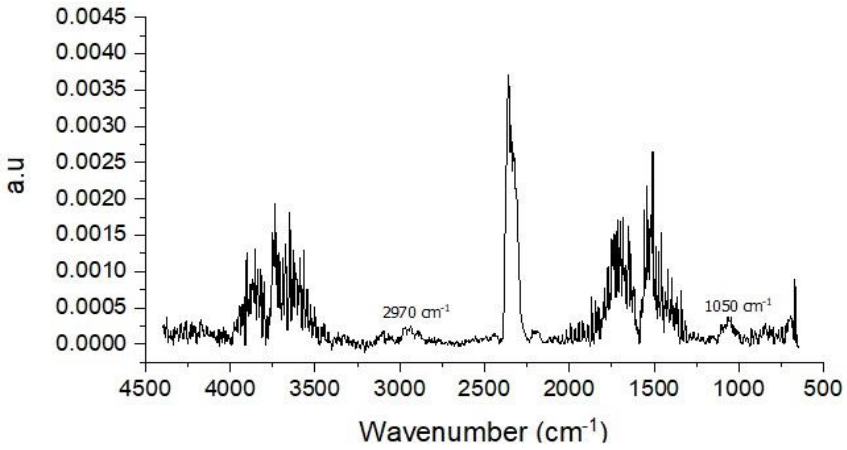

(b)

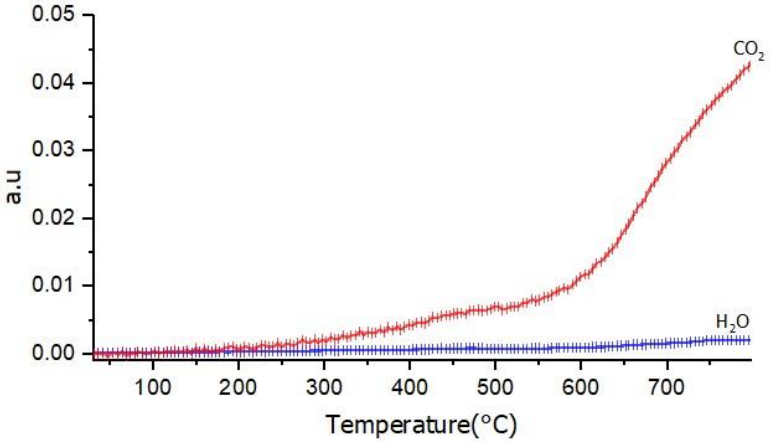

(c)

Figure 30 TG analysis of EG (a) with the correlated IR spectra at 360 °C (b) and the progression of CO_2 and H_2O during the heating(c).

The Raman analysis (Figure 31) revealed that the graphene obtained exhibits a low degree of exfoliation, indicating it consists of few-layer graphene. This conclusion is supported by the position of the G band, which is observed at approximately 1582 cm^{-1}. Typically, the G band undergoes a higher Raman shift in monolayer graphene. Additionally, the presence of a slightly broadened 2D band further confirms the limited exfoliation of the prepared graphene.

Another piece of evidence supporting this hypothesis is the ratio between the intensities of the 2D peak and the G peak, which has a value close to 1.50. This ratio aligns with the expectation for graphene with a low degree of exfoliation.

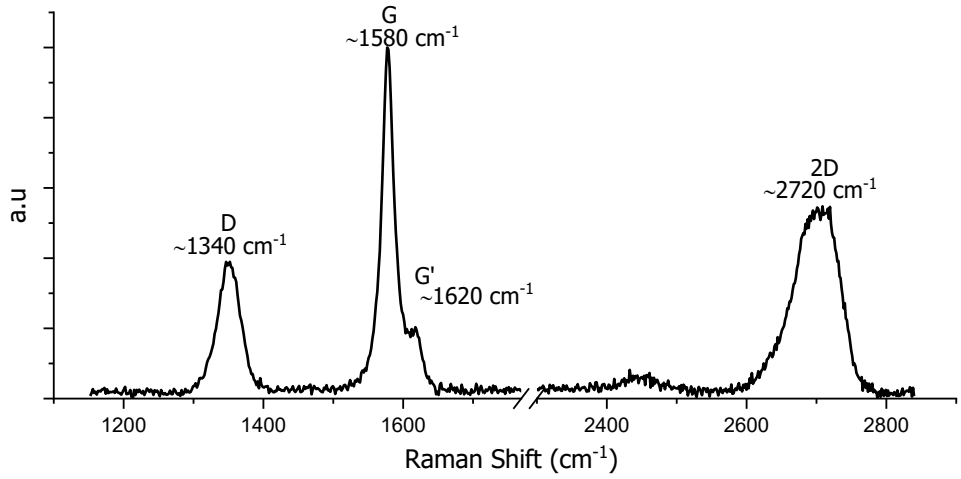

Figure 31 Raman spectra of EG.

The fact that EG does not have a high degree of exfoliation is not a relevant factor for this research. The properties of EG with a few layers still allow for the study of its behavior. Therefore, the focus of this study was directed towards investigating the functionalization of EG and its application in membrane modifications, rather than emphasizing the degree of exfoliation. Conducting an extensive and costly analysis to achieve a higher degree of exfoliation would have consumed valuable time and resources, which could have hindered the progress in preparing the desired modifications on this carbonaceous nanomaterial.

3.1.2 Graphene-based diethyl maleate nanocomposite

The content set forth in this paragraph has been published as a scientific article [88]

To analyze the morphological changes that occurred during the preparation of the GEM nanocomposite with diethylmaleate, electron microscopy was employed. Figure 32 shows a comparison between the exfoliated graphene and the GEM nanocomposite. Upon careful observation at a submicrometer scale, it can be noted that the functionalization process did not induce significant changes to the material's morphology. The graphene aggregates present before the reaction did not exhibit any induced basal plane nanoporosity after functionalization. Additionally, the FESEM images revealed a nearly uniform distribution of polyethylmaleate on the graphene surface, without the presence of diethylmaleate aggregates at a nanometer scale.

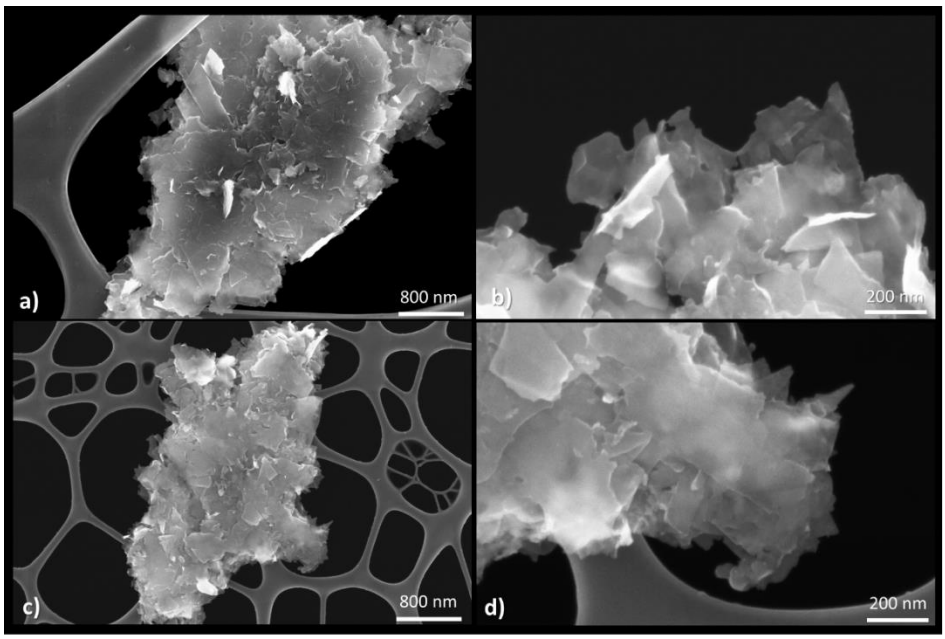

Figure 32Field-emission Scanning Electron Microscopy images at different magnifications showing exfoliated graphene a,b) and GEM c,d) on lacey carbon.

Table 6 TG analyses Weight loss for GEM prepared without and with AIBN

GEM preparation	Weight loss at 156 °C (Wt. %)	Weight loss at 370 °C (Wt. %)	Residual Mass 795 °C (Wt. %)
-	-5.18	-6.73	61.20
AIBN	-6.12	-15.35	70.75

Thermogravimetric analysis coupled with IR spectrometry confirmed the organic functionalization of graphene. The obtained degradation function revealed three distinct degradation steps in Figure 32a. The first degradation step exhibited a maximum degradation temperature of approximately 150°C, followed by a second step with a maximum of around 370°C. The final degradation step occurred around 700°C, showing an increased degree of decomposition up to 800°C.

Comparing the GEM synthesized by the microwave method and the synthesis of GEM with the 'addition of the radical initiator Table **6** , it can be observed that, AIBN increases the polymer formation. The GEM modified with the radical initiator showed a higher resistance to the heating. As reported in Table **6**, the total residual mass is higher than the weight of the material made without a catalyst. The

radical initiator could also promote reticulation and thus preferential carbonization of the polymer.

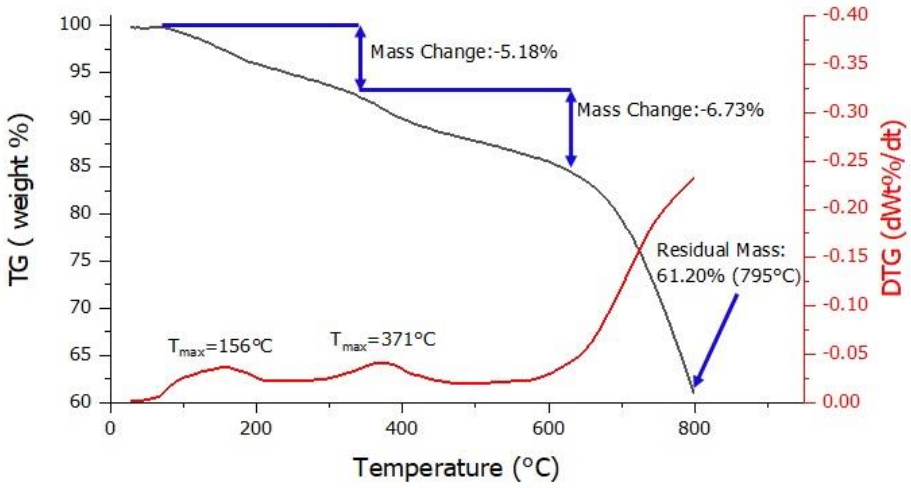

(a)

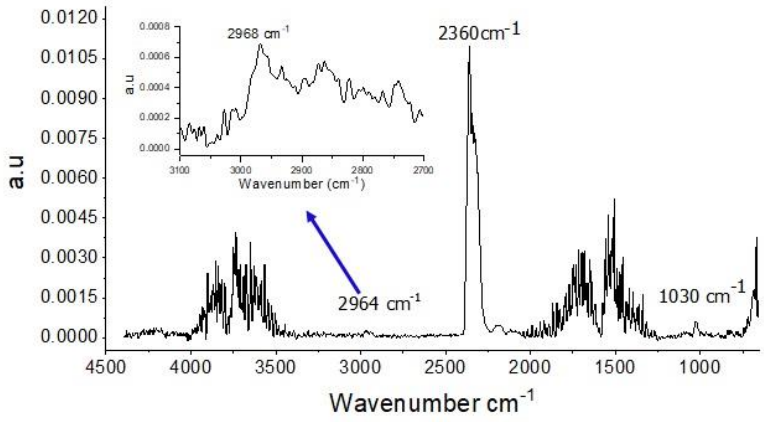

(b)

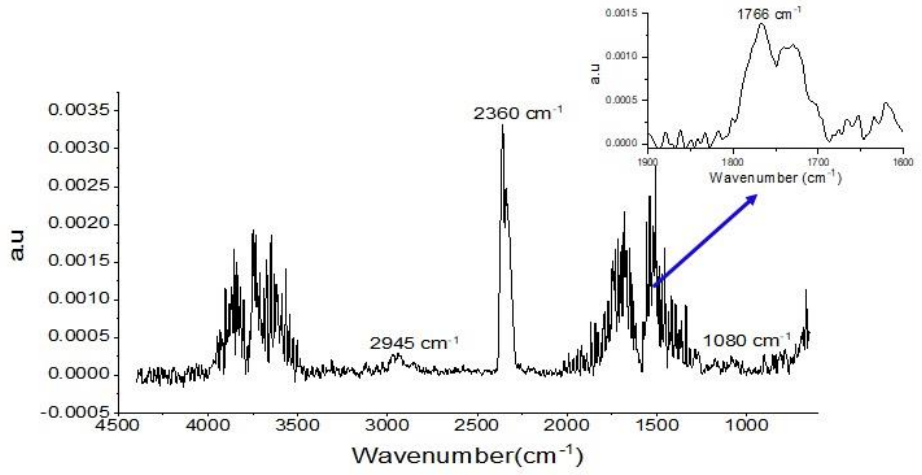

(c)

Figure 33 Thermo gravimetric analysis of GEM(a) with the correlated IR spectra near 150°C (b) and 370°C (c).

Analyzing Figure 32b, the FT-IR analysis in correlation with the maximum peaks observed in the TGA degradation, several important findings can be noted. In the first degradation step, the presence of various gases including CO_2, CO, and water was detected. Additionally, the FT-IR analysis revealed the presence of the C-H stretching of alkyl functions at approximately 2970 cm^{-1} [92]. This stretching is associated with the dealkylation of esters during degradation, which is present due to functionalization and the subsequent formation of degradation products and anhydrides.

In the second degradation step(Figure 33b), the water spectrum was subtracted to reveal additional spectral features. Around 2000 cm^{-1} and 1600 cm^{-1}, the C=O stretching of the ester carboxylic groups became prominent after subtracting the water spectrum. Furthermore, at around 1080 cm^{-1}, the C-H rocking associated with ester derivatives was observed [92,93]. This corroborates the continuous formation of ester derivatives produced during the degradation process of the nanocomposite.

Upon analyzing the Raman spectrum, Figure 34, it is evident that the degree of exfoliation in GEM is low. The G band, which appears around 1582 cm^{-1}, indicates a limited degree of exfoliation [94]. Typically, a higher degree of exfoliation is associated with a higher Raman shift [95]. This observation is further supported by evaluating the intensity ratio of the 2D band to the G band, which is similar to graphene (I_{2D}/I_G = 1.44) [96,97]. These findings suggest that the microwave reactor

reaction did not increase the degree of exfoliation in the initial graphene. Additionally, the ratio of the intensity of the D band to the intensity of the G band is very close to the value obtained from the Raman spectrum of the starting graphene (I_D/I_G = 0.48) [97]. This indicates that there is no significant increase in electronic defects on the graphene surface, and thus, no cycloaddition reactions occurred between diethylmaleate and the conjugated dienes that constitute the electronic structure of graphene.

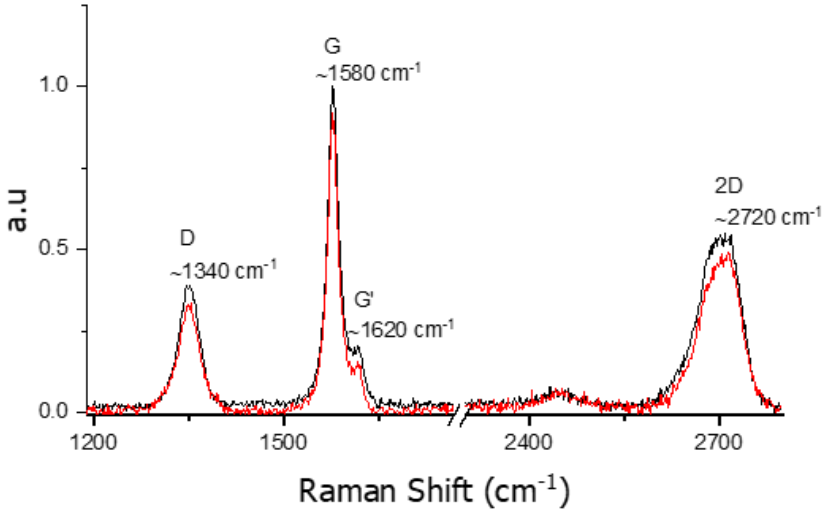

Figure 34 Comparison of Raman spectra of EG (black) and GEM (red).

The lateral size (La) of the graphitic crystallites therefore, according to Tuinstra and Koenig[98], is 9 and 8.7 nm for GEM and EC, respectively. Moreover, the absence of a broad peak at 1530 cm^{-1} suggests that the samples have a high degree of crystallization and no amorphous carbon is present [99].

In line with the Raman spectra, the diffractograms of the starting GEM and EG exhibit similar characteristics, such as an ordered structure and the absence of amorphous broadening [99]. A weak signal is observed at the Bragg reflection at 44.7° (2θ), and the space group is identified as P63mc. Both samples exhibit a strong preferential orientation along the (001) planes, as evident from Figure 35, with the main reflections corresponding to the crystal directions (002) and (004). The values of cell lengths, crystal sizes, and material density, according to the modulated turbostratic model, are provided in Table 7 , which aligns with the estimates obtained from the Raman spectra.

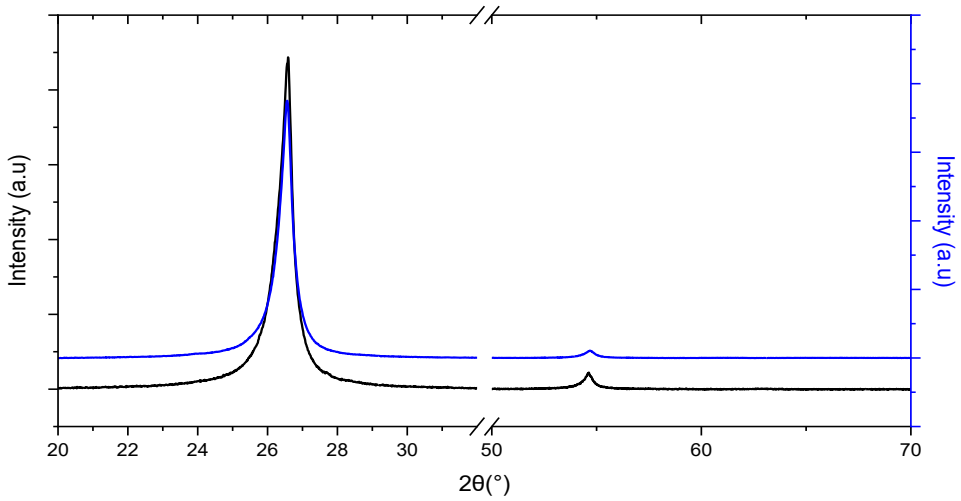

Figure 35 XRD spectra compared of graphene (black) and GEM (blue).

Table 7 Cell parameters for GEM and EG.

Parameters		GEM	EG
Cell length [nm]	A	2.17 ± 0.05	2.12 ± 0.02
	C	6.72 ± 0.01	6.71 ± 0.01
Crystal size [nm]		7.53 ± 4.76	8.02 ± 2.68
Density [kg/m2]		2.90	3.04

By utilizing UV spectrometry, a spectrum was obtained, as depicted in Figure 36. The spectrum exhibits two distinct peaks. The first peak, observed at 265 nm, is associated with the π→π* transition of the -C=C- bonds present in the aromatic rings comprising the surface and boundaries of graphene [100,101]. On the other hand, the second peak, detected at 203 nm, corresponds to the functionalization of graphene. This peak specifically represents the n→π* transition state of the C-O groups within the ester groups of the nanocomposite [102–104].

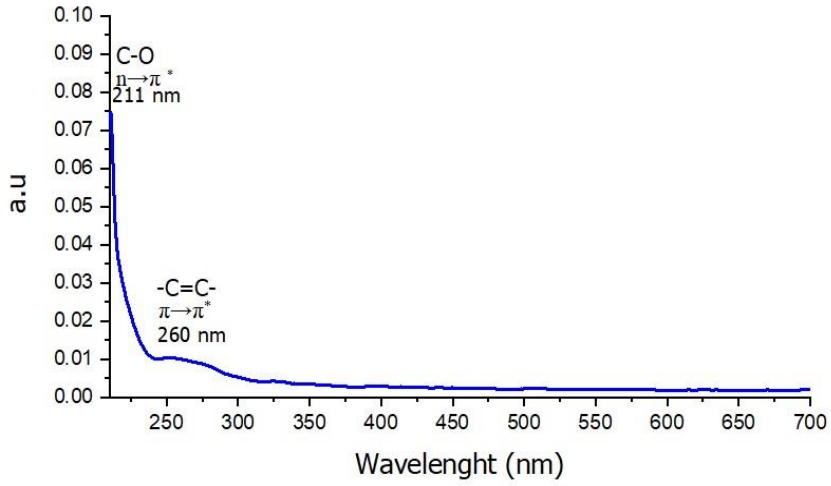

Figure 36 UV spectra of GEM.

The degree of dispersion of the material in ethanol was also assessed using UV analysis with the method proposed by Paredes et al. [105]. For this analysis, samples were prepared by dispersing 30 mg of GEM in ethanol for 5 min. After dispersion, the solution was centrifuged at 5000 rpm for 5 min to separate the supernatant from the excess graphene. The supernatant was then diluted to obtain known concentrations, and a calibration curve was constructed using these dilutions.

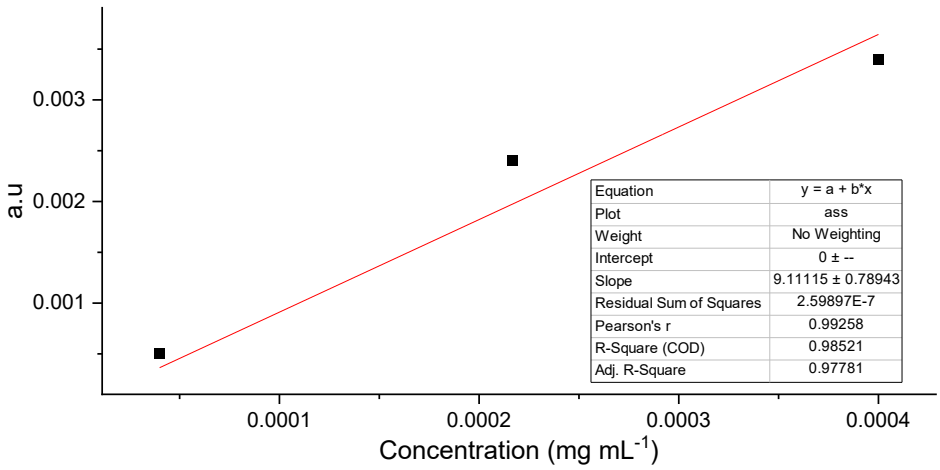

Figure 37 calibration curve to calculate the GEM concentration in ethanol.

From the calibration curve, an extinction coefficient of graphene maleate at 660 nm was determined to be ε = 911.25 $L^{-1}g^{-1}m^{-1}$. With the obtained extinction coefficient, and by applying Lambert Beer's law.

$$A = \varepsilon l C$$

Where A is the absorbance, ε is the extinction coefficient, C is the concentration and l is the optical path length, the maximum estimated concentration of maleate graphene in ethanol is 1.093 g ml^{-1}.

X-ray photoelectron spectroscopy was employed to analyze the chemical composition of the exfoliated graphene surface both before and after modification with diethyl maleate. The survey spectra revealed noticeable changes in the composition of the outer surface of the graphene flakes. A semi-quantitative analysis indicated an increase in the oxygen content, which rose from 4.2 at% to 8.8 at% following the modification.

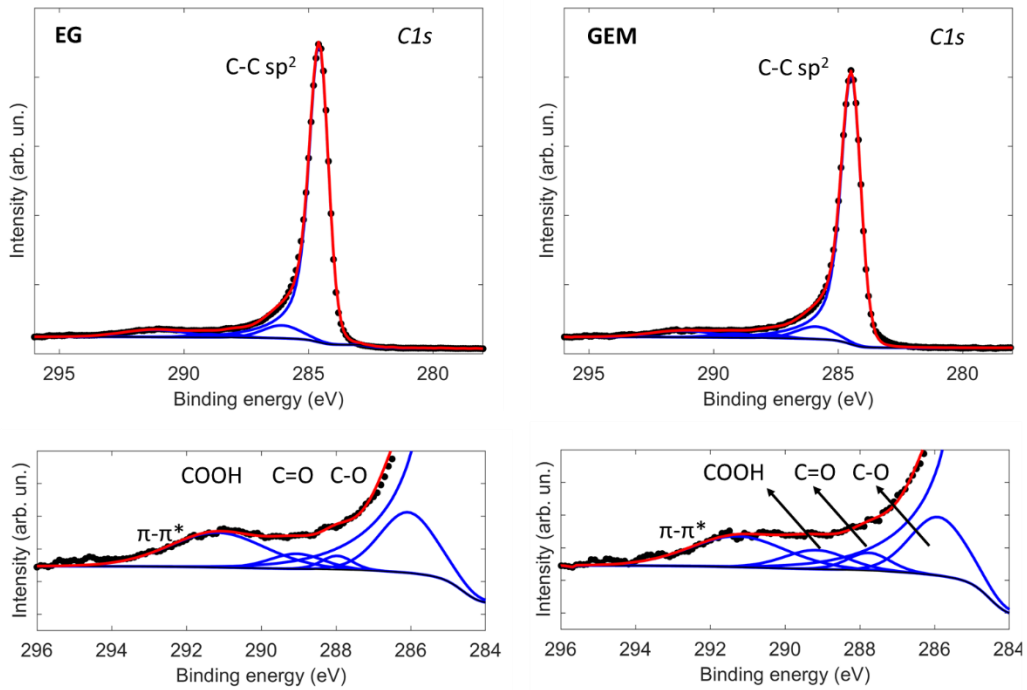

Figure 38 Comparison of XPS analysis of EG and GEM.

Table 8 peaks of XPS analysis of EG an GEM

EG				
C-C sp2 (mol %)	**C-OH (mol %)**	**C=O (%)**	**COOH (mol %)**	**π-π* (mol %)**
86 ± 1	6.2 ± 0.6	0.8 ± 0.3	1.4 ± 0.3	5.9 ± 0.7
GEM				
C-C sp2 (mol %)	**C-OH (mol %)**	**C=O(mol %)**	**COOH(mol %)**	**π-π* (mol %)**
84 ± 2	6.3 ± 0.2	1.5 ± 0.5	2.3 ± 0.4	5.6 ± 0.9

Table **7** presents the C1s region of the photoelectron spectrum, which provides further insights into the functionalization process with maleate. Concerning pristine graphene, the C1s region (Figure 38) shows the characteristic asymmetric C-C sp2 component, alongside the π-π* satellite, following the literature on graphene-based materials. [71]. Low-intensity components related to oxygen-containing functionalities (C-O, C=O, COOH) are present, which are induced by the exfoliation process. A slight increase in the contributions from C=O and COOH groups was observed, consistent with the molecular structure of the maleate. Notably, the contribution of the π-π* satellite, closely associated with the graphitic structure, remained preserved. This indicates that the functionalization process did not lead to a significant increase in defects, aligning with the findings from the previously discussed Raman analysis.

The degree of graphene dispersion was quantitatively compared using the method proposed by Coleman et al. [106–108]. Graphene was mixed in equal amounts with different solvents to assess their dispersibility, as depicted in Figure 39 Comparing solvents with lower boiling points, such as water and ethanol, or solvents with lower toxicity, such as dimethylsulfoxide (DMSO), it is evident that DMF and NMP exhibit optimal dispersing capabilities for graphene.

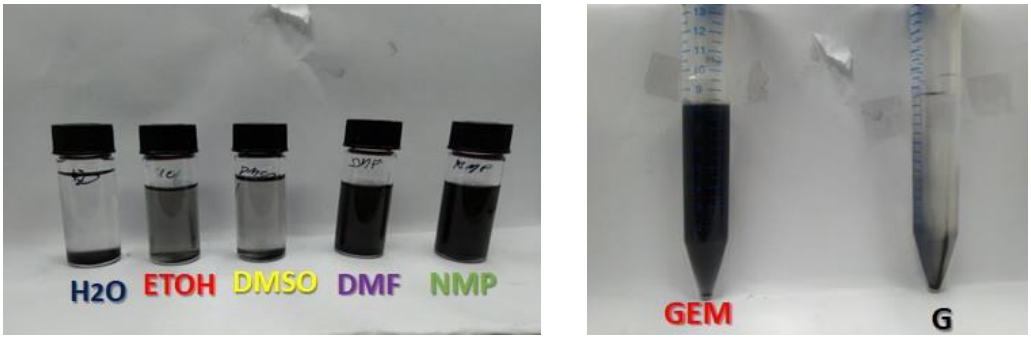

(a) **(b)**

Figure 39 Graphene Dispersion in Various Solvents (a) and Comparison of GEM vs EG Dispersed in Ethanol and Centrifuged for 10 min.

In contrast, GEM exhibits excellent solubility in ethanol, easily dissolving with just a few min of sonication. Figure 40 illustrates a visual comparison of the ethanol dispersions of GEM and graphene, highlighting the superior dispersion achieved with the nanocomposite. Notably, the GEM dispersion remains highly stable over an extended period, even after one year of storage in the dark at room temperature, as evidenced by the absence of significant precipitation. The stability of the GEM dispersion is further supported by the zeta potential measurements, with an average Zeta P value of -30mV obtained initially. Remarkably, even after one year, there is only a slight decrease in the average Zeta P, reaching -28mV, indicating the sustained moderate stability of the dispersion [109].

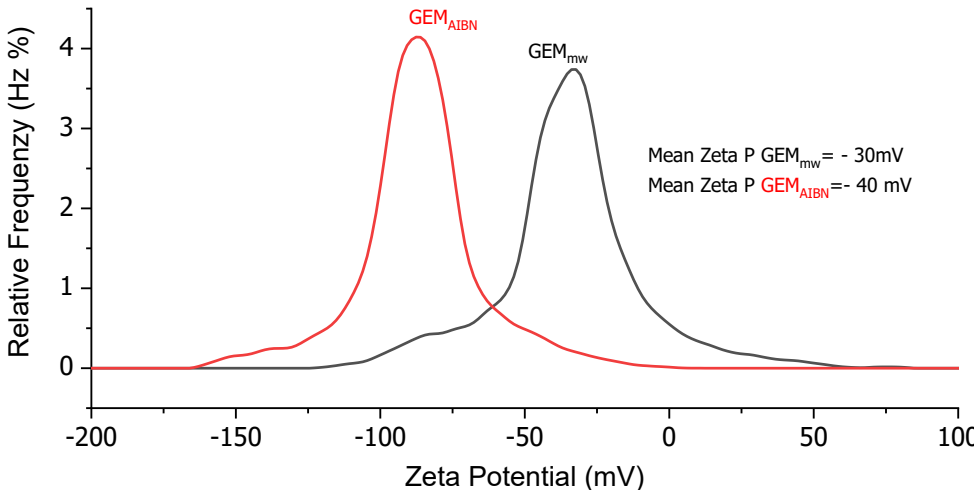

(a)

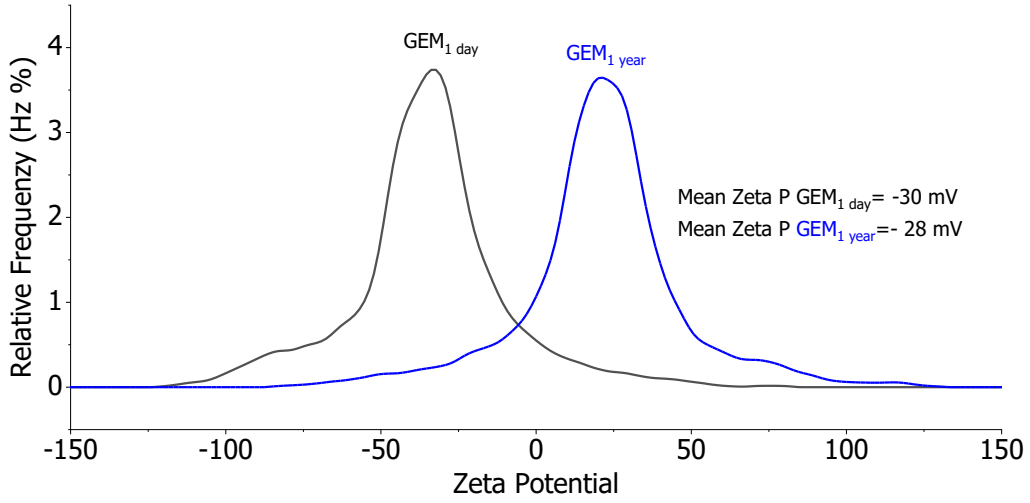

(b)

Figure 40 Zeta Potential of GEM in ethanol synthesized using microwave (MW) or AIBN (azobisisobutyronitrile) initiator is presented in (a). The comparison of the zeta potential values of freshly prepared GEM synthesized with MW and its stability after one year is shown in (b).

The incorporation of a radical initiator, such as AIBN, in the polymerization process enhances the ordering and stability of the maleate structure on the graphene surface. The average zeta potential (ZetaP) of the material prepared using this catalyst reaches -40mV, indicating excellent stability, which is characteristic of materials with favorable dispersion properties.

Table **9** shows the concentrations of ethanol dispersions of different types of graphene materials studied in recent years: Chen et al. developed a colloidal graphene (GC) using p-phenylenediamine as a dispersing agent, obtaining a concentration of 0.2 mg mL^{-1} [110] also there is a much-studied composite composed of graphene and polyvinylpyrrolidone (G-PVP) that to date has the highest concentration of graphene dispersed in ethanol, reported in the literature [111–113]. The GEM material achieves a high concentration, comparable to the reference concentration, in ethanol. However, GEM results are more stable over time, as the concentration of graphene materials starts to precipitate after a few days/weeks in the other paper descriptions, and in the case of GEM it is possible with simple storage to keep the dispersion stable over time, it will start to decrease the stability after one year and very slowly.

Table 9 Graphene concentrations in various solvents with different stabilizers with a focus on dispersibility on ethanol.

Material	Stabilizer	Conc. (mg mL^{-1})	Ref.
GEM	Poly diethyl maleate	1.09	[this work]
EG	-	0.09	[107]]
GC	p-phenylenediamine	0.2	[[110]]
G-PVP	Polyvinyl pyrrolidone	0.8	[[111–113]]

3.1.3 Discussion about Graphene functionalized with acetyl dicarboxylate

Starting from the functionalization present in the literature of maleic anhydride with graphene [81,82], it was studied in parallel to the functionalization with diethyl maleate also that with its alkane derivative with most reactivity of the molecule and with a good dienophilic appearance, so it was studied how to obtain a Diels-Alder cycloaddition on the graphene surface. The functionalization was assessed through TGA-IR, UV-Vis, and Raman analysis. UV-Vis spectroscopy revealed two distinct absorption bands (Figure 41). The absorption band at 265 nm corresponds to the characteristic $\pi \rightarrow \pi^*$ transition of the -C=C- bonds in the aromatic rings of graphene. Additionally, a prominent absorption peak at 203 nm was observed, indicating the $n \rightarrow \pi^*$ transition of the C-O groups present in the ester groups of the material, typically found between 200-210 nm. Notably, as the concentration increased, the peak shifted towards 200 nm.

Table 10 peaks obtained with UV analysis of the different graphene made with acetyl dicarboxylate

	Mrt	M60	M125	M135	M175	Mrt_cd
UV-Vis peak, alcoholic solution (EtOH) λ= nm	**203 253**	**267**	**202 254**	**208 253**	**206 265**	**260 267**

The spectra of Mrt, M125, M135, M175, and M175mhq exhibited similar peak patterns. Therefore, for brevity, only a comparison between Mrt and M125 is presented in Figure 41a. In this comparison, Mrt displayed peaks at 203 and 253 nm, while M125 exhibited peaks at 203 and 254 nm. On the other hand, M60 and Mrt_cd displayed a single peak with a broad band at 266 and 267 nm, respectively,

indicating variations in the absorption bands of graphene. Figure 41b showcases the spectrum of M60.

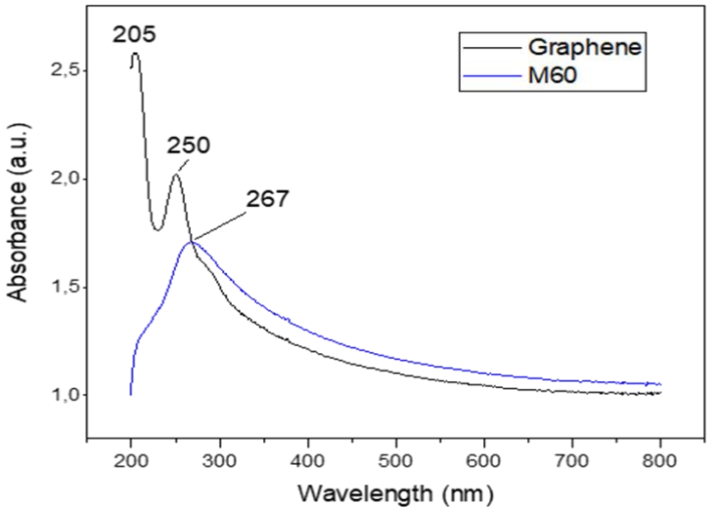

(a)

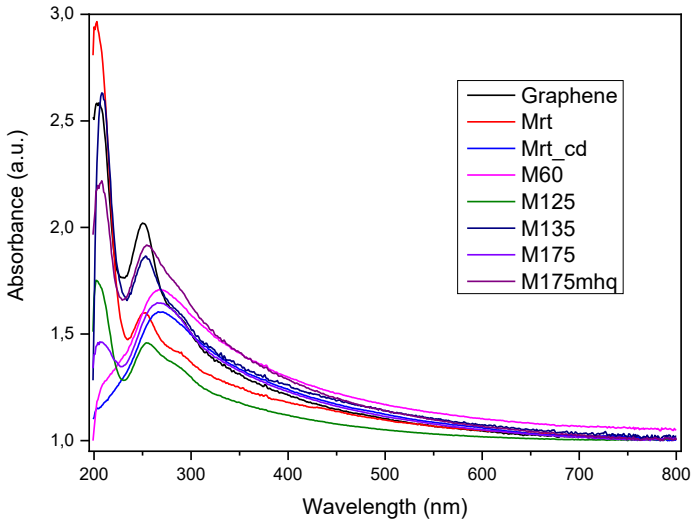

(b)

Figure 41 Comparison of UV spectra between Graphene compared with M60 is shown in Figure (a), while Figure (b) illustrates the comparison of UV spectra between Graphene and all samples studied.

The observed variations in the absorption bands of M60 and Mrt_cd suggest that they have undergone chemical functionalization, indicating the presence of new chemical groups or bonding interactions with other molecules. To confirm this, a fluorescence spectrum was performed on Mrt_cd, a commonly used technique to study the chemical and physical properties of materials. The fluorescence test provided further insights into the nature of the functionalization, confirming the presence of chemical modifications in the graphene samples.

Fluorescence spectra were obtained using synchronous-scan excitation mode on dispersed samples in ethanol. The emission spectrum was recorded by measuring the relative intensity of radiation emitted as a function of the wavelength at a constant excitation wavelength (λex) of 266 nm. Figure 42 presents the fluorescence emission spectra, revealing two strong emission peaks (λem) at 527 and 538 nm.

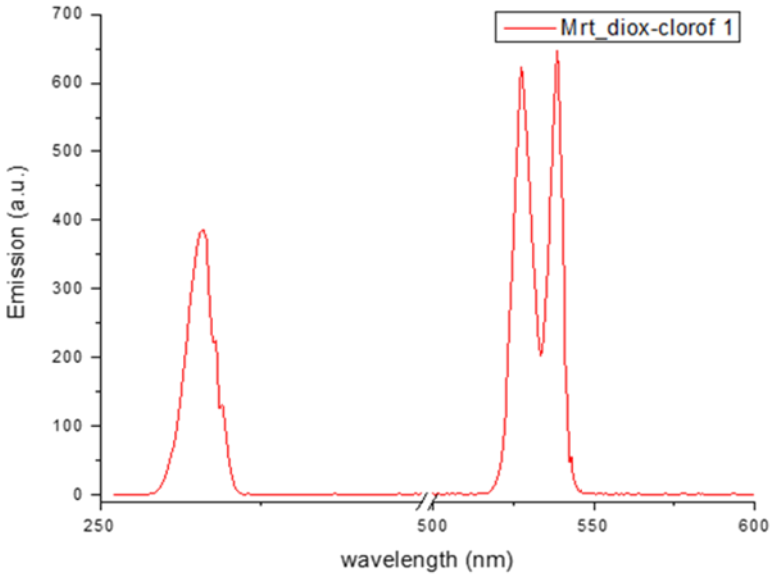

Figure 42 Fluorescence analysis of Mrt_cd

Absorption spectra of the molecule adsorbed onto the graphene foil (both pristine and oxidized) were calculated using the time-dependent density functional theory (TDDFT) approach and compared with the molecule's absorption spectrum before it was attached to graphene.

It was observed that when the molecule is chemically bonded to graphene, a low-frequency absorption peak (between 500 and 600 nm) appears. These results

are consistent with the fluorescence signal observed for functionalized graphene. According to simulations, it was observed that the origin of this peak could be attributed to hybridization between the π orbitals of the bound molecule and those of the graphene matrix.

These studies are further detailed in the article currently under submission. "Green synthesis of functionalized graphene-based material with Dimethyl but-2-ynedioate for electrochemical energy storage devices" which will be included as an appendix to the thesis

TGA-IR studies were conducted to assess the thermal stability of the compounds. All compounds exhibited a two-step degradation process, with the first step occurring at around 300°C and the second degradation occurring at around 650°C. The residual mass at 799°C was approximately 45%, except for M125 and M175, which showed a higher residual mass of around 65%. Gas phase IR analysis at different temperatures was performed for each compound, revealing characteristic peaks associated with water (two broad bands at 4000-3500 and 1800-1300 cm^{-1}), CO_2 (four peaks around 3500 cm^{-1} and one strong peak at 2350 cm^{-1}), and carbon monoxide (two bands at 2150 cm^{-1}). The spectrum of M60 displayed peaks at 1740 cm^{-1} attributed to the C=O stretching of the COOEt group (see Figure 43b).

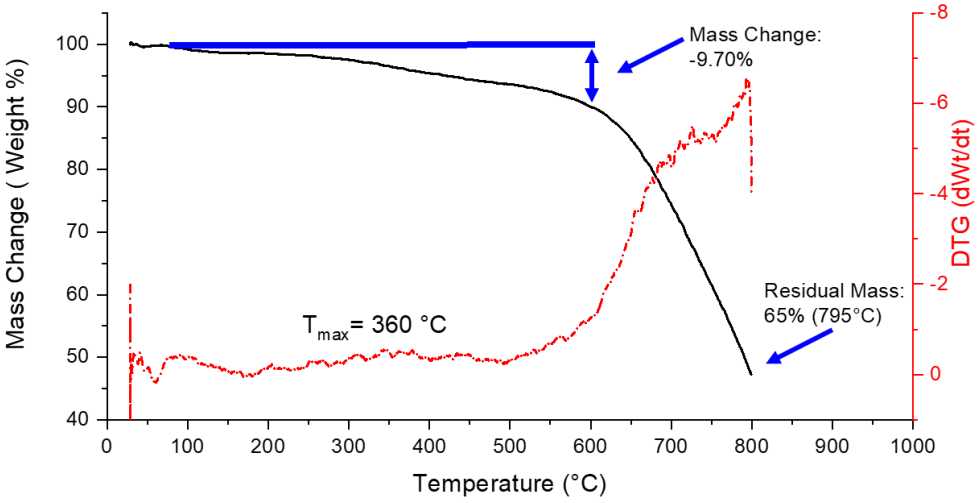

(a)

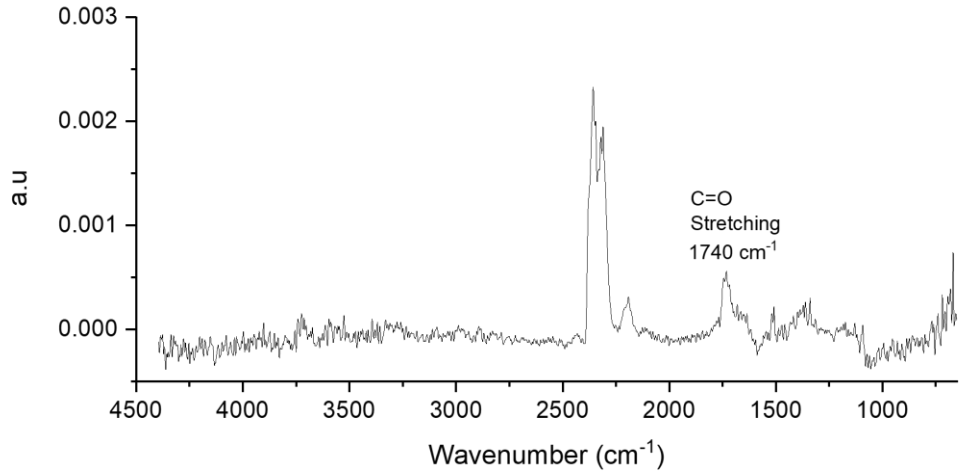

(b)

Figure 43 TG analysis of M60 (a) and the correlate IR spectra at 425°C

Among the samples subjected to thermal treatment, M60 exhibited the highest degree of functionalization, as supported by the IR analysis results.

Raman spectroscopy was performed on all samples, and the results are presented in Figure 44 and

Table **11**. The pristine material exhibited the typical features of exfoliated graphene material, with three main peaks observed in the spectrum: the D band at

1352 cm^{-1}, the G band at 1582 cm^{-1}, and the 2D band at 2712 cm^{-1}. The D band is related to the defectiveness in the sp^2 domains, as it is due to the A1g breathing vibrations of six-membered sp^2 carbon rings, becoming Raman-active when the symmetry of the nearby lattice is reduced by defects or functional groups in the material. The G band originates from a first-order inelastic scattering process involving the degenerate iTO and iLO phonons at the G point (E2g mode). Close to the G band, a weaker D' peak at 1620 cm^{-1} can be observed, again related to the amount of disorder in the lattice. The 2D band is the second order of the D band, involving two iTO phonons near the K point. In contrast to the D band, the 2D band is allowed without any kind of disorder or defects, and its shape depends on the number of graphene layers, with multiple peaks convolution [97] The intensity ratio between the D peak and G peak is related to the mean dimension LD of the graphenic domains, as Id/Ig is proportional to LD-alpha, where alpha=1 for edge defects [98] and alpha=2 for point defects. Thus, the increase in the I_D/I_G ratio reflects the augmented defectiveness of the graphenic materials. From the data reported in Table 11, it is possible to observe an increase in the I_D/I_G ratios for all the treatments performed, except for the mild room temperature treatment in toluene. The maximum effect (I_D/I_G = 0.79) is observed when 50% chloroform and 50% dioxane are chosen as the solvent solution, but the effect is remarkable for all the treatments proposed. Conversely, a downshift in the 2D peak position and a more symmetric profile are evidenced after all the functionalization treatments.

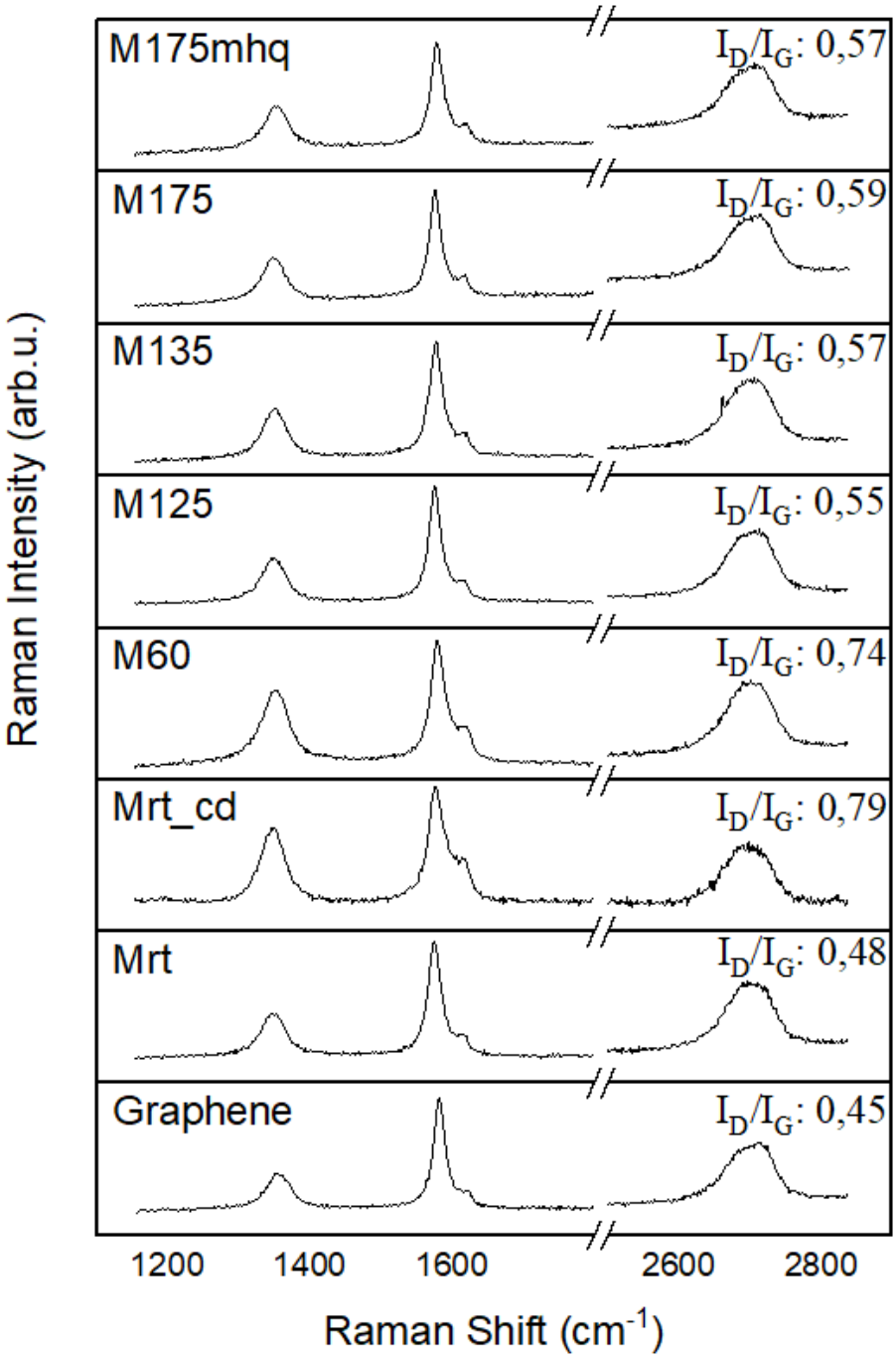

Figure 44 Raman spectra of graphene before and after functionalization

Table 11 Raman spectra Position of D, G peaks of graphene before and after functionalization and intensity ratio I_D/I_G values.

Sample	Peak positions cm^{-1}			I_D/I_G
	D	G	2D	
M175mhq	**1350**	**1579**	**2705**	**0.57**
M175	**1348**	**1577**	**2707**	**0.59**
M135	**1354**	**1579**	**2705**	**0.57**
M125	**1350**	**1575**	**2707**	**0.55**
M60	**1354**	**1579**	**2690**	**0.74**
Mrt_cd	**1350**	**1577**	**2698**	**0.79**
Mrt	**1352**	**1575**	**2696**	**0.45**
Graphene	**1352**	**1582**	**2712**	**0.45**

The diffraction pattern of the pristine material shows a multiplicity of broad and sharp peaks. The major broad peak is centered at 11 degrees (2theta) and it is often linked to graphene oxides [114]. This pattern is presented in Figure 45, while in the main article, the broad peak has been included in the background correction of the patter only to appreciate the crystalline peaks. The sharp peaks reveal the presence of two symmetries of the graphite which are the P63mc (COD code 00-900-8569) which is 77.18% of the crystalline part of the powder and the R-3:R (COD code 00-901-2705) which is the remaining 22,82%. Those two phases are evidenced in Figure 45 a and b from the blue and red pattern, respectively. From the Rietveld refinement, the crystallite size of the two phases is, according to the turbostratic model [115], about 470 and 395 A° with similar microstrain of 1.4u and 1.7u, respectively. The sample M60 instead, presents the P63mc phase alone, without any broadening associated to GO or short-range order of phases.

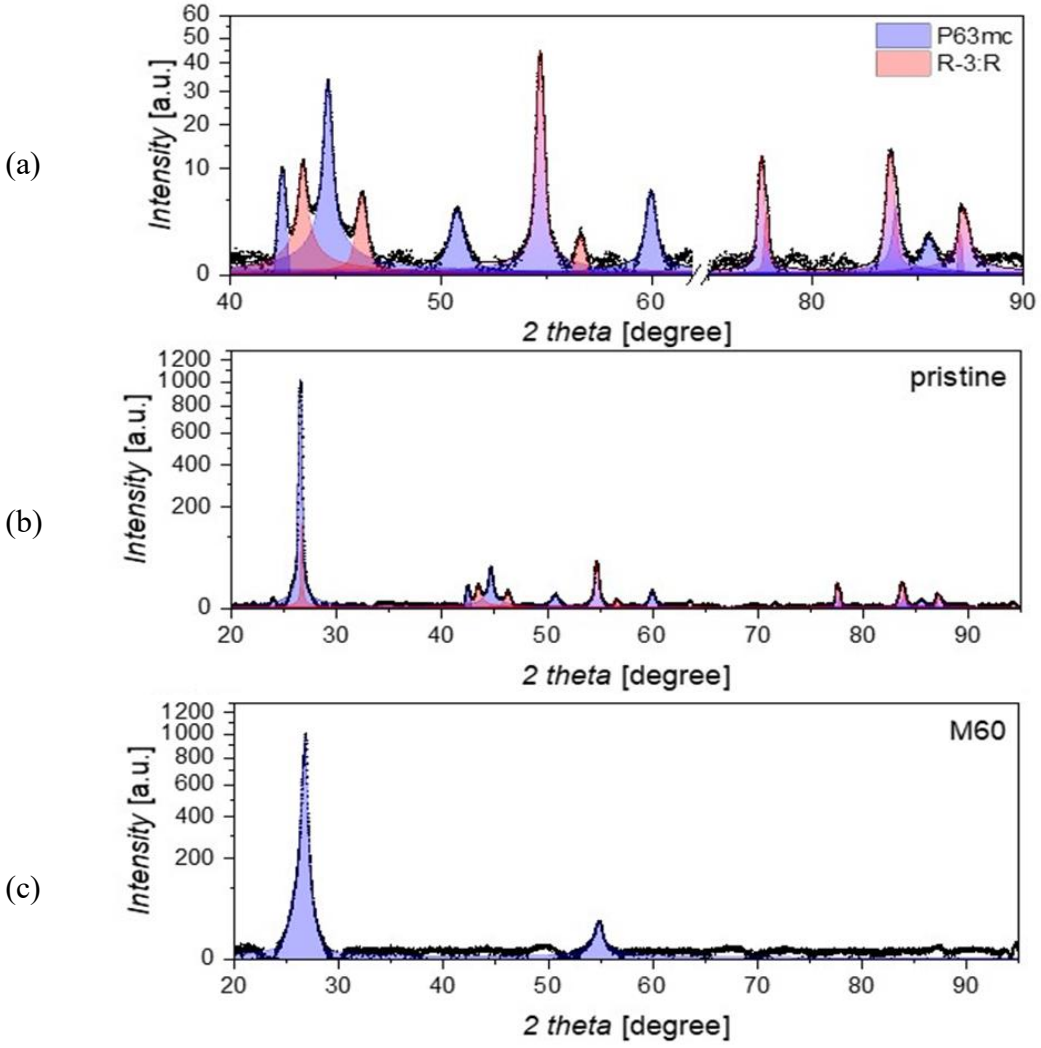

Figure 45 Pattern of the pristine powder with an (a) enlargement of the regions of 40-62 degrees and 75-90 degrees and (b) the whole pattern. (c) Pattern of the sample M60. Both the patterns have been substracted with the background radiation and for (a) and (b) the broad peak of GO was subtracted.

The cell parameter *c* related to the distance between the graphene layers of the graphite shortened concerning that of the pristine powder, decreasing from 6.7258 A° to 6,6821 A° in the self-standing sample, indicating densification of the material. The average crystalline size also decreased to 173 A°, well evidenced by the enlargement of the FWHM of the (0 0 2) peak shown in Figure 45c. Moreover, it is worth noticing that M60 presents a strong preferential orientation along the (0 0 *l*)

crystalline directions, consistent with the membrane formation procedure. The basic parameters retrieved form the refinement are reported in Table **12**.

Table 12 basic parameters retrieved form the refinement.

	PRISTINE					
COD code	00-900-8569			00-901-2705		
	P63mc			R-3:R		
		value	err		value	Err
Cell	a	2.4627283	3.83086E-4	a	3.6485388	7.9854747E-4
Cell	c	6.7258334	0.0019736902	alpha	39.479244	0.0124688605
Crystalline size		469.3685	8.159473		395.0778	7.33459
Microstrain		0.001431792	1.4131724E-4		0.001742072	2.1327745E-4
Density	2.2581			2.257		
Weight +- 0.66 %	77.18			22.82		

	M60		
COD code	00-900-8569		
	P63mc		
		value	err
Cell	A	2.2239	0.0012
Cell	C	6,6821	0,0005
Crystalline size		172.74	1.22
tMicrostrain		0,00219	0,00024
Density	2.7874		
Weight %	100%		

3.1.4 Graphene functionalized with Tetracyan Ethylene.

Figure 46 shows the Raman analysis of G(TCNE), compared to the Raman spectrum of EG, confirming the occurrence of the Diels-Alder reaction on the graphene surface. The intensity ratio between the G-band and the D-band (ID/IG) varied from 0.7 for exfoliated graphene to approximately 0.42 for graphene functionalized with TCNE. This decrease in ID/IG indicates an increase in the number of defects on the graphene surface, which significantly reduced the intensity of the D-band. However, the ratio of the 2D band to the G band remained

relatively similar between the spectrum of exfoliated graphene and functionalized graphene, with a value close to 1.90. This suggests that the degree of graphene exfoliation does not significantly change with the functionalization reaction using tetracyanoethylene Figure 46.

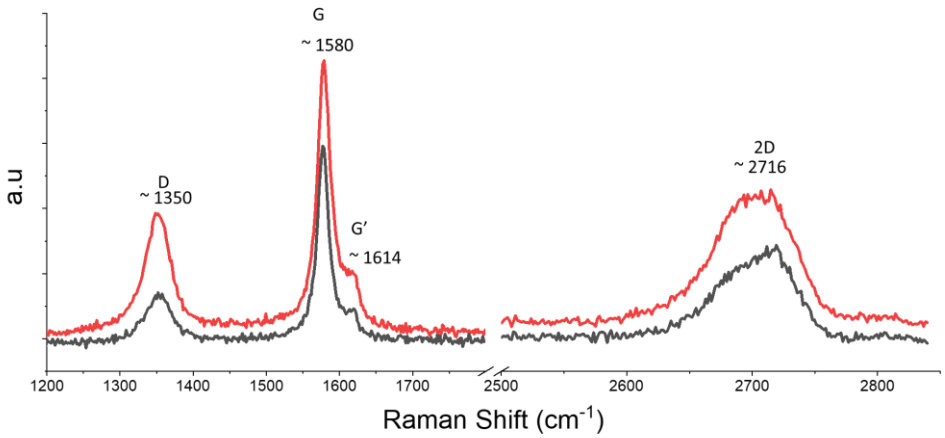

Figure 46 Raman spectroscopy comparison between G(TCNE) (red) and pristine EG (black).

Figure 47 presents the thermogravimetric (TG) analysis of G(TCNE). The TG curve demonstrates a continuous weight loss as the temperature increases. The total weight loss corresponds to 10.30% of the initial mass of the material. At 795 °C, a residual mass of 76.74% of the starting material's total mass remains. In combination with infrared spectrometry, the degradation products were identified. The analysis revealed a significant formation of water and CO_2. Additionally, the spectra exhibited the stretching of CN at around 2200 cm^{-1} at approximately 150 °C. tetracyano ethylene is known for its instability, leading to rapid degradation. The observed stretching of C=O in the spectra suggests the oxidation of CN groups with water, while the formation of CO_2 originates from the degradation of oxygen residues on the material's surface.

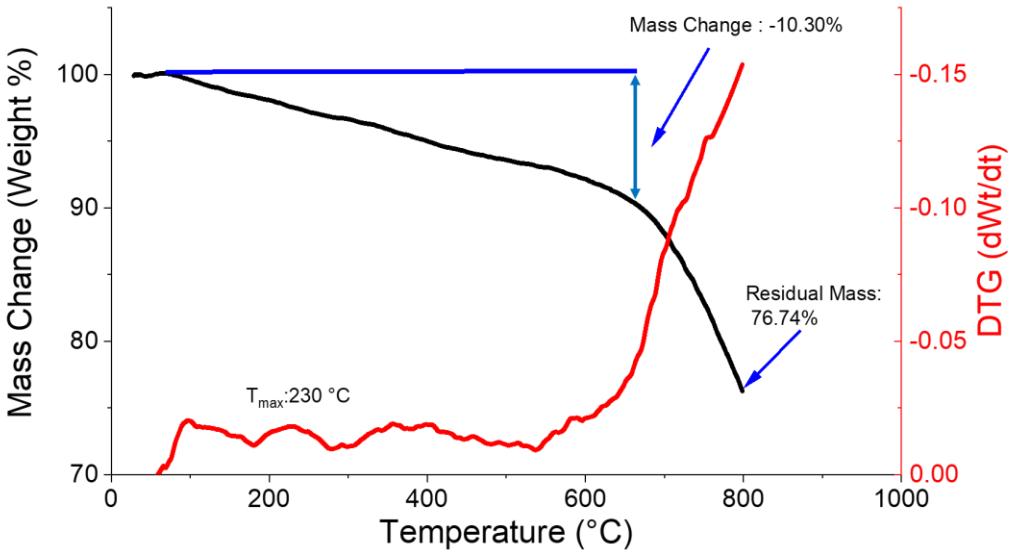

Figure 47 TG analyses of graphene functionalized with Tetracyan Ethylene

3.2 Matrix

3.2.1 Discussion about PIM-1

In the Figure 48, ATR spectrum analysis of the PIM-1 polymer, confirms the occurrence of the polymerization reaction. The spectrum reveals several characteristic peaks indicative of the polymer's structure. Firstly, the stretching of aromatic C-H bonds, along with the stretching of aliphatic C-H bonds, is observed at 2935 cm-1. Additionally, a peak at 2240 cm^{-1} corresponds to the stretching of CN groups, its intensity varies depending on the presence of oxygen groups nearby. The symmetric and asymmetric C=C stretching of the carbon atoms within the aromatic ring is represented by peaks at 1681 cm^{-1} and 1445 cm^{-1}, respectively. Furthermore, the presence of a peak at 1260 cm^{-1} confirms the condensation of the two starting units for polymerization, as it is associated with the C-O-C stretching of aromatic ethers. This peak signifies the formation of ether bridges between individual polymer molecules.

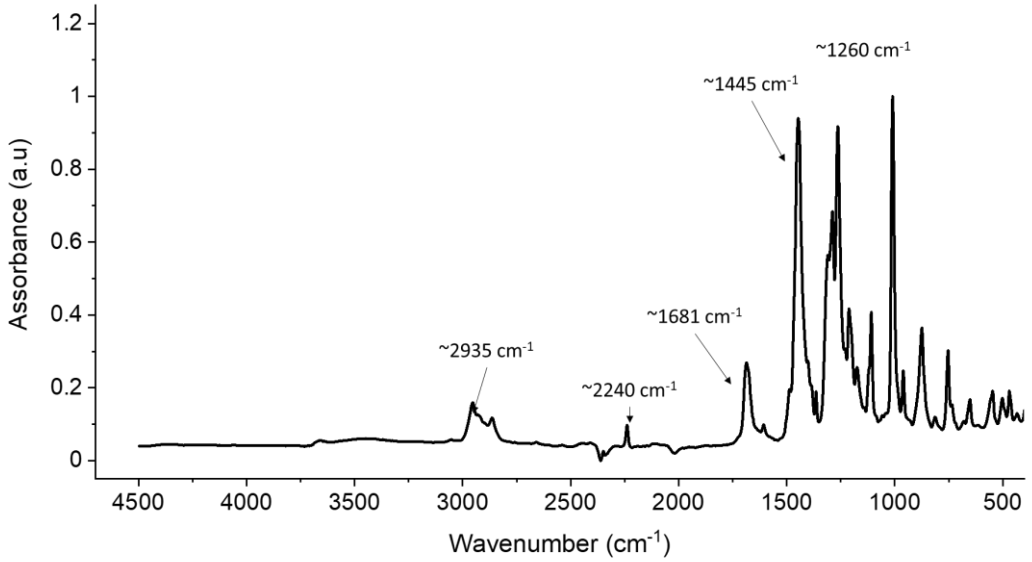

Figure 48 ATR spectra of synthesized PIM-1 polymer

Figure 49 thermogravimetric analysis demonstrates the polymer's stability up to approximately 400 degrees Celsius, beyond which degradation initiates. The peak of maximum degradation occurs around 528°C, resulting in a loss of 39.21% of the polymer's total mass. Upon reaching the maximum temperature of the analysis, a residue equal to 60.6% of the initial sample's total mass remains at 795°C.

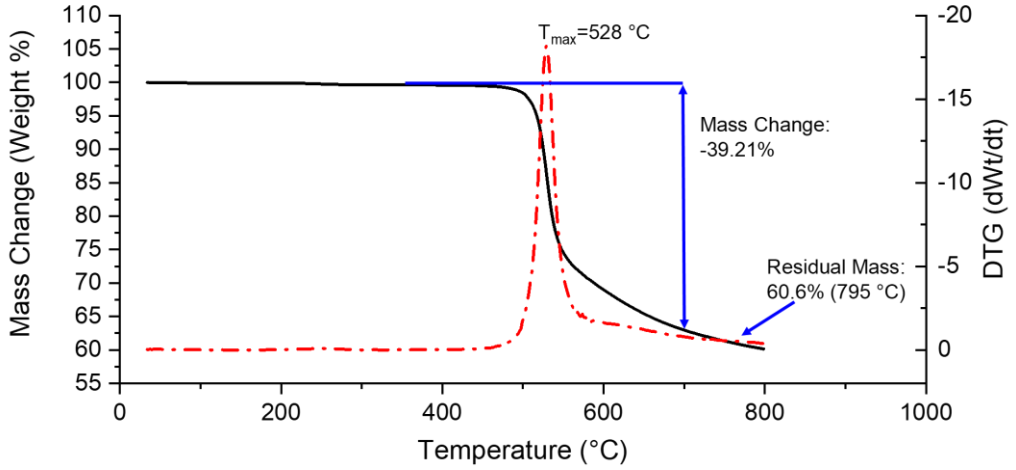

Figure 49 TG analysis of PIM-1 synthetized

Chapter 4

Mixed matrix membrane results and discussion.

This chapter will discuss the qualitative and performance analysis of the membranes and studied, the multilayer membranes will be discussed separately:

- The PSU membrane covered with GEM will be discussed next to the PSU and graphene membranes,
- The membranes covered with PIM-1 will be discussed next the PIM_1GTCNE MMMs
- Last paragraph concerns the study done in parallel of the PIM-1 IL composite membrane with BMIM Suc. and BMIM acetate.

It is important to point out that the measurements with the DVS were made by doing 4 cycles of absorption and desorption in vacuum, initially inserting 0.2 Bar of of the gas under analysis inside the chamber, When the membrane reaches saturation, a vacuum is imposed in the chamber by removing all the gas, then a higher CO2 concentration of 0.2 Bar, then 0.4 Bar, and finally a concentration of 0.8 Bar is inserted.

To a conceptual simplification we preferred to see these pressures in Bar, as percentage concentration of relative pressure of the gas, within the discussion the gas values will be expressed as 20%, 40%, 60 and 80% of relative pressure of the gas under examination, and in the graphs obtained from the membrane performance will have on the X axis the values in percent

4.1 PSU-based membranes

4.1.1 PSU-graphene nanocomposite membranes

All membranes were subjected to DSC analysis with three cycles of heating and cooling, ranging from 50 to 250°C. The first heating cycle was performed to remove any residual solvent traces from the material, which could interfere with the analysis and is not relevant to the study.

The analysis of the materials' glass transition temperatures (as shown in Figure **50**) reveals that the presence of graphene in the composite does not significantly alter the PSU's physical properties within a concentration range of up to 5%. The glass transition temperature remains in the range of 170-180°C, indicating that the addition of graphene has minimal impact on this characteristic of PSU.

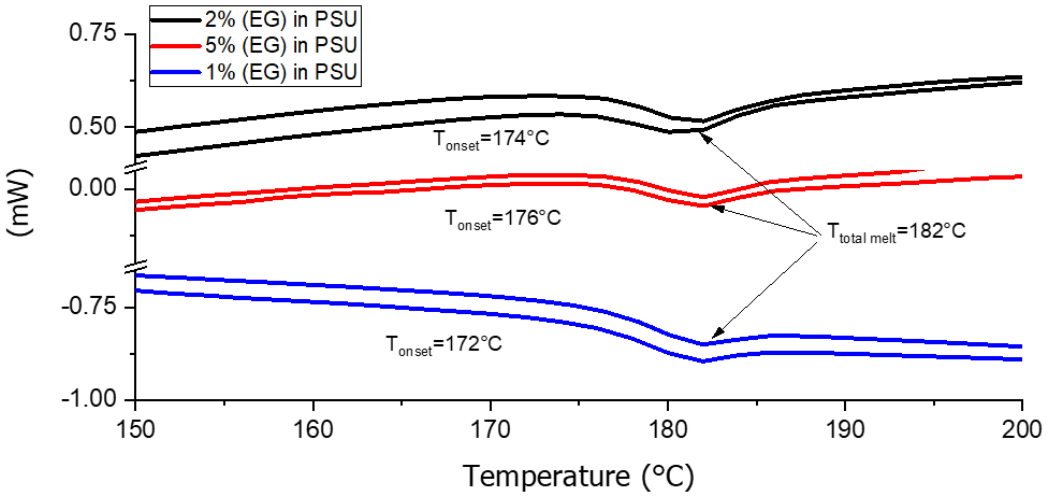

Figure 50 DSC analysis of PSU 2ith 1, 2 5 % of EG

The thermogravimetric analysis (Figure 51a) of the membranes revealed a mass loss starting around 130°C, which corresponds to the onset of the glass transition of the PSU at this temperature, the collapse of the porous structure and a loss of mass are observed due to the consequent removal of the traces of solvent remaining embedded within the membrane. in paragraph 2.1.6 (pag.40) talking about the preparation of the membranes it was mentioned that after laying the solution containing the polymer, on a glass substrate, the preparation is left to dry under a fume hood, the negative pressure of the membrane allows the NMP solvent to sublimate to a large extent leading to the formation of the porous matrix of the

membrane which takes on a color from white (in the absence of graphene) to gray, black (in the presence of graphene) , within the porous structure small amounts of NMP solvent remain embedded. If we had used a vacuum system to prepare the membrane, such as a vacuum stove, the embedded solvent would have been removed totally to the detriment of the porous structure, in fact the solvent removed quickly and in large amounts would have re-dissolved the polymer and collapsed the pores leading to a colorless solid nonporous membrane (appearance of the solid, nonporous PSU). in the case of the TG we observe, at the glass transition temperature) the collapse of the pores , the loss of the amount of solvent contained within the pores, resulting in a loss of weight, however by carefully observing the trend of the curve (Figure 51b) we subsequently see a slight increase in weight, perceived by the instrument.

this change and increase in weight is due to a change in the density of the material, removed the solvent the porous structure continues the collapse, when it is now totally collapsed it has given way to a denser material with a different buoyancy to the porous material which was lighter, as a result a small percentage by weight is regained.

Comparing the PSU membrane with the membrane containing 5% EG Figure 51b, a lower buoyancy thrust is observed for the latter, this is because the presence of graphene within the matrix has increased the density of the membrane by decreasing the amount of pores within the matrix, so with the collapse of the structure and removal of the solvent, when by now the material analyzed is more dense the balance is reestablished in the presence of graphene the density varies less as the temperature increases.

The actual degradation of the material occurs at a temperature of 529°C. It is important to note that the observed mass loss is not indicative of degradation but rather a change in the density of the material being analyzed. The TGA of the membrane also containing ionic liquid Figure 51c shows a TG trend very similar to that of the membranes containing the polymer and filler alone, mass loss around 120°C is also observed here, thus the presence of the ionic liquid within the matrix did not affect the inherent glass transition temperature of the polymer.

When comparing the TGA curves of the membranes with different concentrations, it becomes evident that before the collapse of the structure, the membrane containing 5% by weight of graphene exhibits a higher density compared to the other membranes. This can be attributed to a lower number of pores and the

presence of channels formed by the aggregation of PSU around the graphene, resulting in the expansion of the channels within the porous structure.

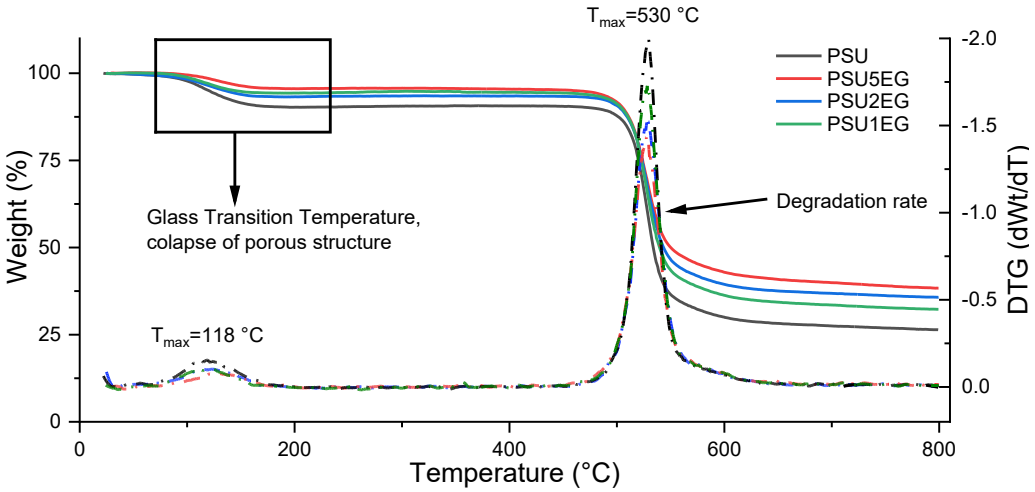

(a)

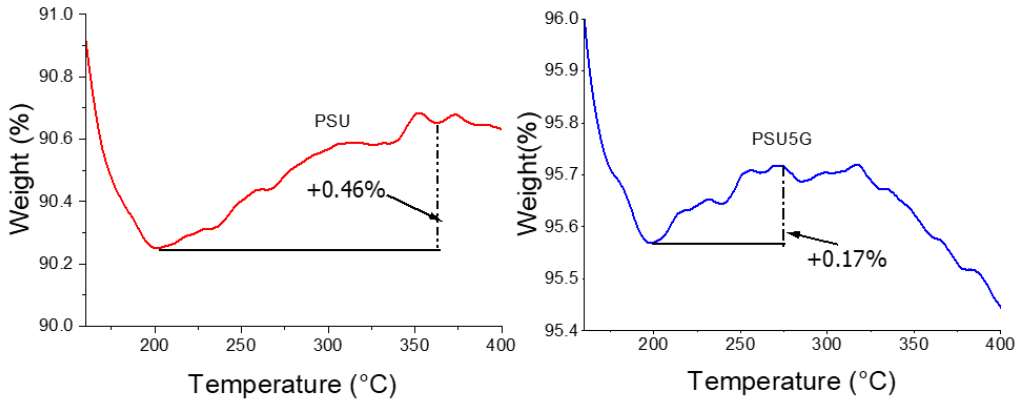

(b)

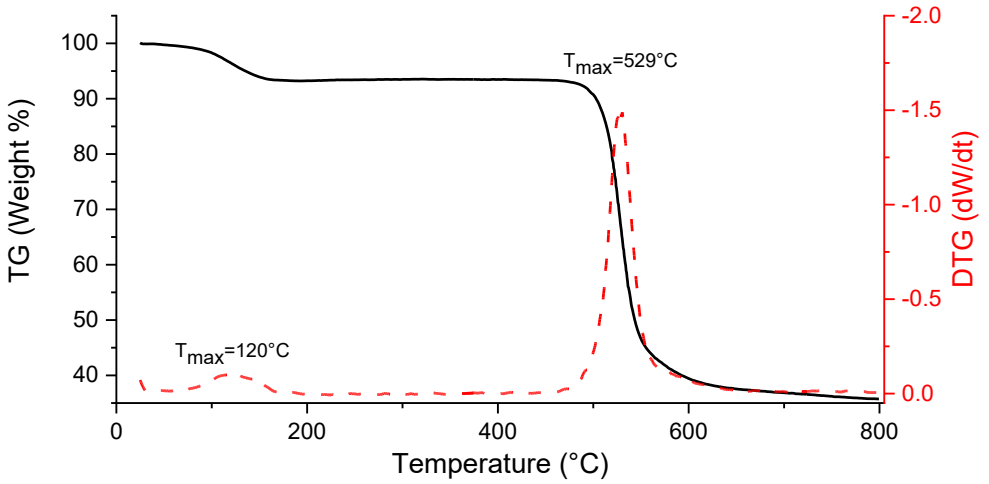

(c)

Figure 51 TG analysis of PSU and PSU with different concentrations of graphene. Comparison of mass loss curves between PSU and PSU with varying concentrations of graphene. (a) Impact of graphene on the porosity of the membranes at the glass temperature (b). TG of PSU2GIL. (c)

This structural difference is confirmed by electron scanning microscopy (ESEM) analysis (Figure 52). All samples were prepared using a cryostatic cutter, and with an increase in exfoliated graphene content, significant changes in morphology are observed.

Notably, when graphene constitutes 2% of the total mass, the formation of areas with high polymer density can be observed in the cross-section of the membrane. The number of these areas increases further when the graphene concentration reaches 5% by weight.

Electron microscopic analysis reveals the presence of graphene in these high-density areas. This contraction of the structure leads to two effects:

1) The formation of large channels where pores are present, resulting from the internal contraction of the polymer structure.

2) A decrease in porosity within the high-density zones.

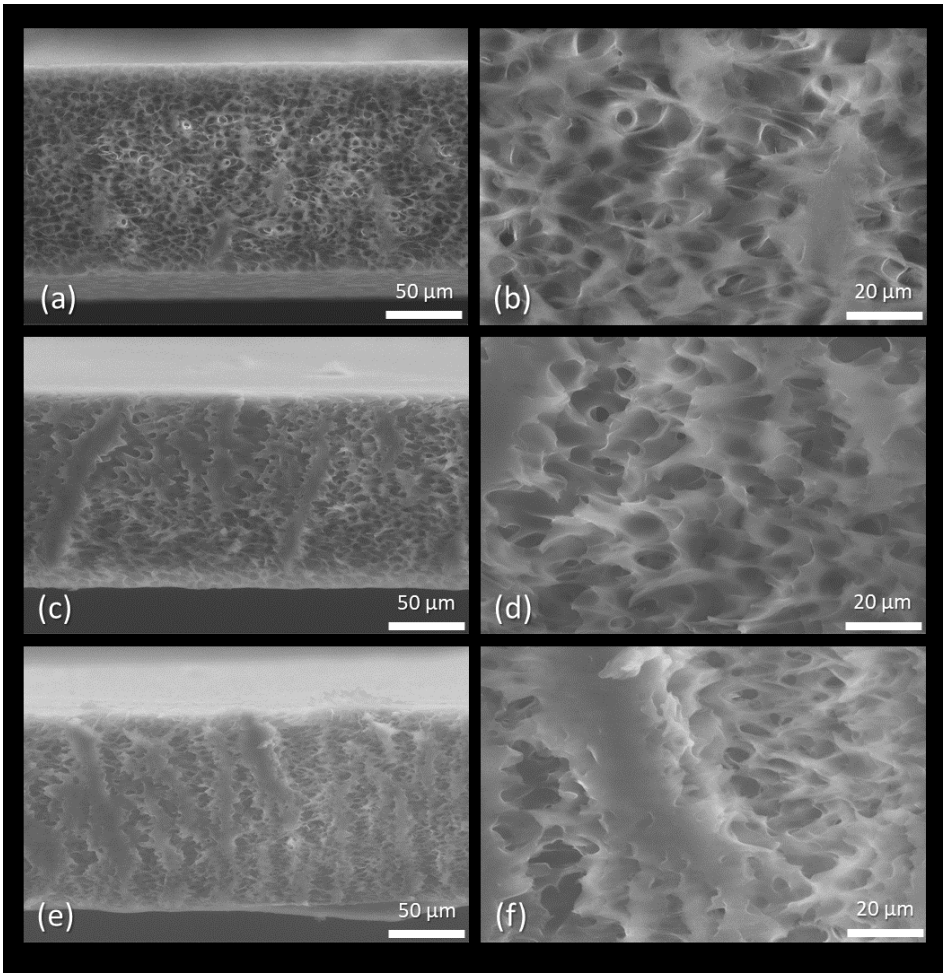

Figure 52 Morphological ESEM analysis of PSU with graphene at concentrations of 1% (a,b) 2%(c,d), and 5% (e,f)

The data obtained from volume and density measurements, as shown in the table, further confirm the effect caused by the presence of graphene.

Table 13 Evaluation of sample densities.

Name	Volume (cm^3)	Thickness (cm)	Density ($g\ cm^{-3}$)
PSU1G	**0.0108 ±0.01**	**0.009±0.0001**	**0.441 ±0.02**
PSU2G	**0.0109 ± 0.01**	**0.009 ±0.0001**	**0.480 ±0.02**
PSU5G	**0.0300 ±0.02**	**0.0086 ±0.0001**	**0.506 ±0.01**

Membranes were prepared by incorporating 5% of BMIM Suc into the matrix. Infrared analysis indicates that there is no chemical interaction between the polymer matrix, graphene, and the ionic liquid. The characteristic peaks of PSU are observed, and no significant changes are observed in the spectra, suggesting the absence of chemical bonding or reactions between the components. On closer observation we observe in the range between 1720 cm^{-1} and 1640 cm^{-1} the presence of a shoulder at 1714 cm^{-1} correlated with C=O stretching of amide of succimidate group, and a rightward shift of the peak at 1685 cm^{-1} that in the presence of the liquid and ionic and 5% graphene shifts to the right at 1680 cm^{-1}.

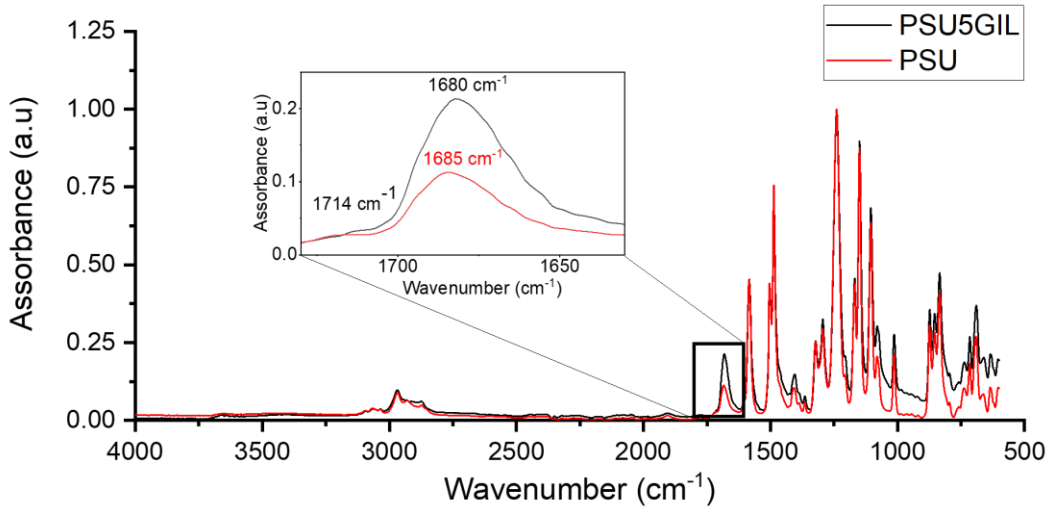

Figure 53 Comparison of the IR spectra of membranes, PSU with 5% EG and BMIM Succ with PSU pure membrane.

Solubility, diffusion, and membrane permeability analysis for CO_2 were conducted using a microbalance. The experimental procedure involved introducing a gaseous atmosphere with a constant relative pressure of CO_2 into the system, followed by evacuation of the chamber, and then repeating the measurement at a higher relative pressure. This cyclic process allowed for the evaluation of CO_2 solubility, diffusion, and permeability characteristics of the membrane.

Based on the gas performance analyses of PSU membranes containing graphene, several observations can be made. Firstly, the solubility of CO_2 in the membranes (Figure 54a) increases with the addition of graphene, particularly at graphene concentrations between 1% and 2%. However, at a concentration of 5% EG, the solubility dramatically decreases and approaches that of pure PSU. A

similar trend can be observed in the diffusion of gas through the membranes (Figure 54b). The membrane with 5% EG behaves similarly to the porous material without filler, while the membranes with 1% and 2% graphene exhibit a greater increase in gas diffusion, except at 20% relative pressure (Figure 54c) where however there could be some errors due to the low rate error/signal. It is important to note that at this low CO_2 concentration, the absorption by PSU is much lower compared to the other membranes, leading to potential calculation errors when evaluating the membrane at this relative pressure.

Considering the solubility and diffusion it can be inferred that the permeability, which depends on these two factors, is significantly higher for PSU membranes with 1% EG and 2% EG. These membranes demonstrate similar performance, with slightly higher performance observed in PSU membranes containing 2% EG.

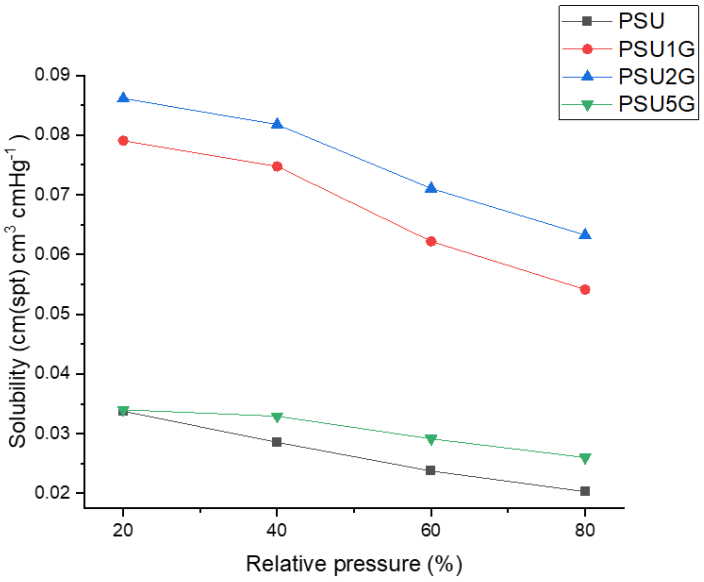

(a)

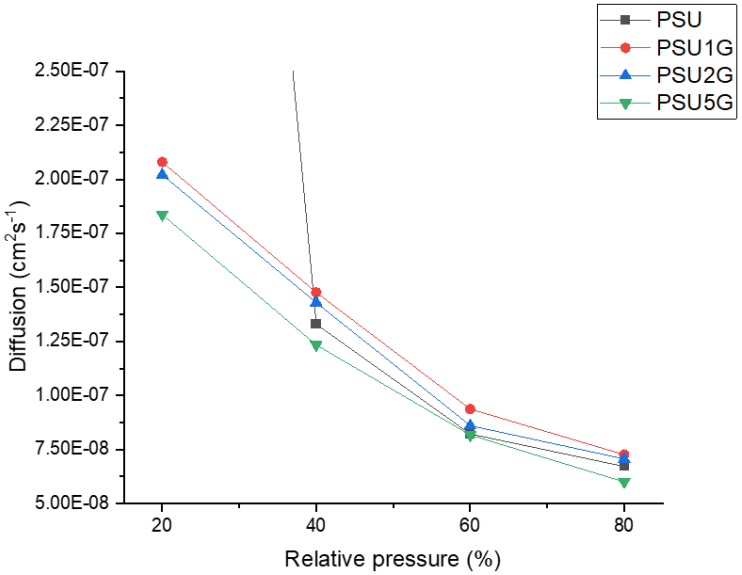

(b)

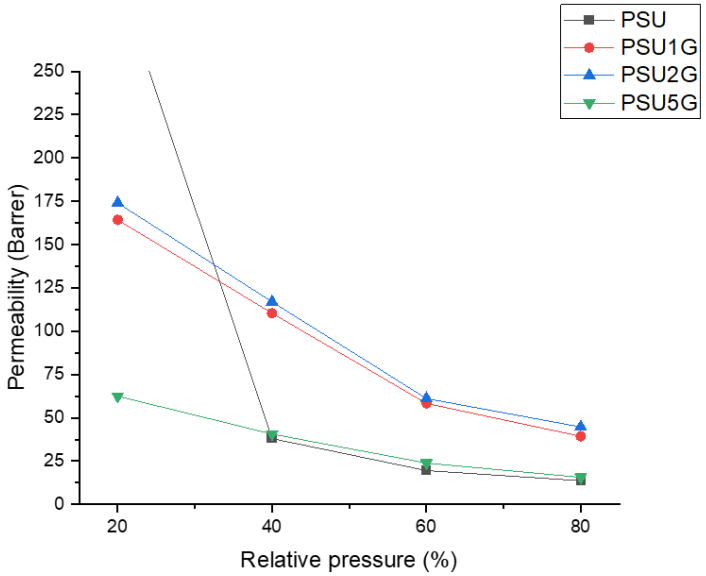

(c)

Figure 54 Comparison of Gas Performance in CO_2 atmosphere between PSU Membrane with EG and PSU Membrane the solubility performance (a) diffusion(b) and permeability (c).

When comparing membranes containing EG to those with the addition of BMIM Succ (Figure 56), it is evident that the presence of ionic liquid within the matrix negatively affects the CO_2 performance of the membranes. In the case of the membrane with 5% EG, the presence of BMIM Succ has a positive contribution to the solubility of CO_2, which increases noticeably. On the other hand, the membrane containing 2% EG, which initially showed better performance, suffers from the presence of the ionic liquid. This is particularly evident when looking at the diffusion data, where the membrane with 2% EG and BMIM Succ exhibits a significant decrease in gas diffusion values, indicating a greater difficulty for CO_2 to diffuse one possible reason why this occurs may be related to the morphology observed in cross section by ESEM microscopy (Figure 52).

As mentioned earlier, the presence of graphene increases the number of areas of higher density at the expense of the porous structure, due to the inorganic polymer-filler interaction. Up to a concentration of 2% (Figure 55) there is an increase in these denser regions and a deformation of the pores, which are wider and pulled compared to the pure PSU membrane.

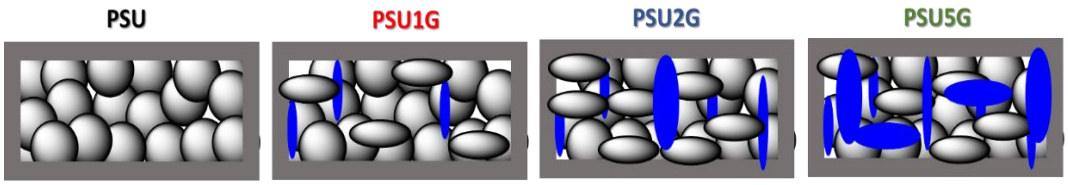

Figure 55 schematic representation of the change in the cross section an the porous(grey shapes) of PSU membranes with different concentration of EG, with an increase of high denstity region (blu shape) with the icrease of EG.

When the EG concentration reaches 5% of the whole material, the higher density spots increase dramatically (Figure 55) decreasing in large numbers the porous regions and making the membrane more dense and low porous, as observed by TG analysis and density measurements.

Interestingly, the membrane containing 5% graphene benefits from the presence of the BMIM Suc, as CO_2 diffuses more easily through this membrane. This can be attributed to morphological changes in the cross-section of the membrane, creating wider spaces that can accommodate the ionic liquid. Although the ionic liquid itself slows down the diffusion of gas due to its viscosity, the presence of wider spaces in the membrane containing 5% EG allows for more

efficient CO_2 diffusion. In contrast, the membrane containing 2% EG, when combined with the ionic liquid, experiences a significant drop in performance.

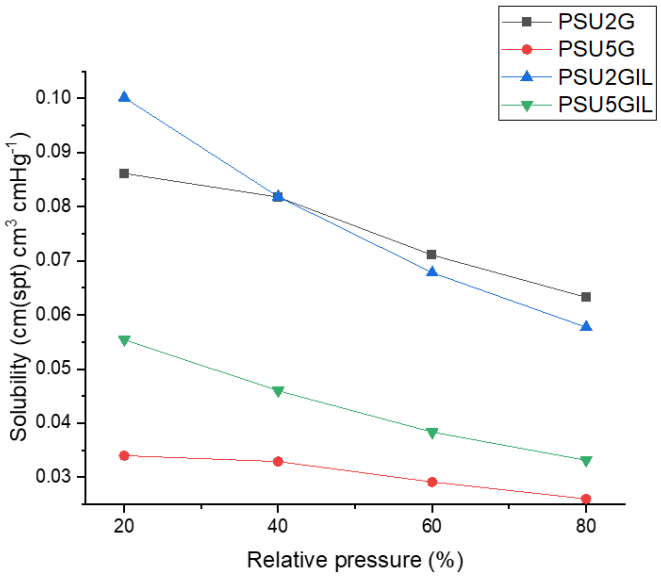

(a)

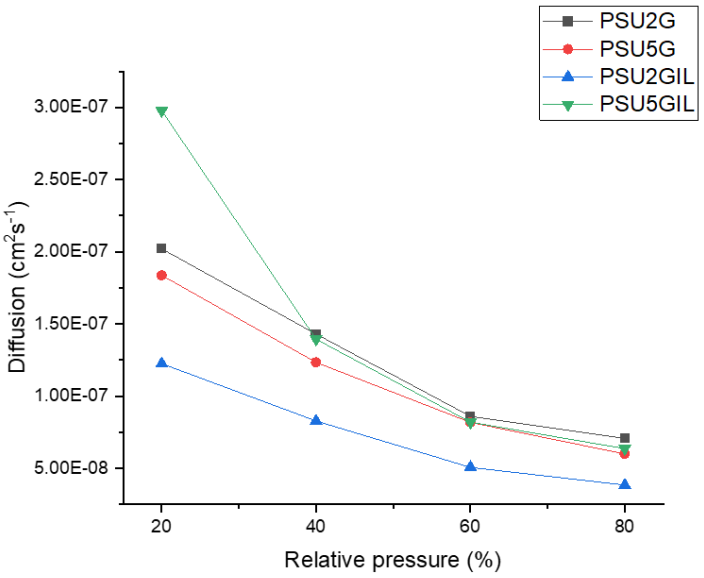

(b)

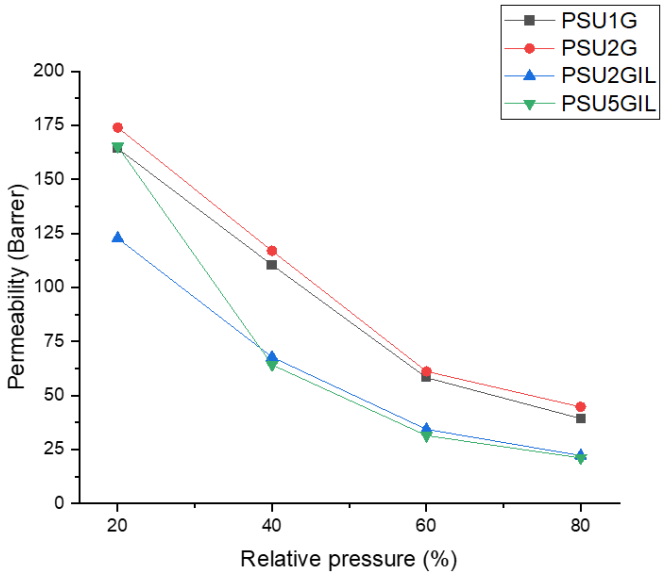

(c)

Figure 56 Comparison of Gas Performance in CO_2 atmosphere between PSU MMM with and without EG and BMIMSuc, respectively the solubility performance (a) diffusion(b) and permeability (c).

Based on the permeability data obtained, it is observed that the PSU membrane with 2% graphene (without the ionic liquid) still exhibits the best performance for CO_2 permeability.

When the ionic liquid is inserted inside the membrane two fundamental factors come into play that affect membrane performance, on the one hand CO2 is more membrane-like and in contact with the ionic liquid it reacts and chemically binds; on the other hand the capture and release of the molecule come into play, which go to affect the rate of diffusion, there being three fundamental steps: adsorption on the surface, absorption into the liquid (by chemical reaction), and release from the ionic liquid (by bond breaking).

Added to these factors is a third factor, ionic liquids tend to increase in density when they react with CO_2, slowing down the passage of this gas more.

These factors added to the morphological changes related to the filler have led to good results when EG has a concentration of 2% , where there are a large number of pores, some deformed and enlarged, others remaining the size similar to pure

PSU. When IL is inserted some pores will be filled by the ionic liquid, others will remain empty or hold small traces of the solvent (Figure 51) CO_2 finds different ways to pass.

When we increase to 5% EG, the high-density regions are in greater numbers Figure 55, and by inserting the ionic liquid most of the pores will be filled with IL, resulting in slower uptake, and diffusion.

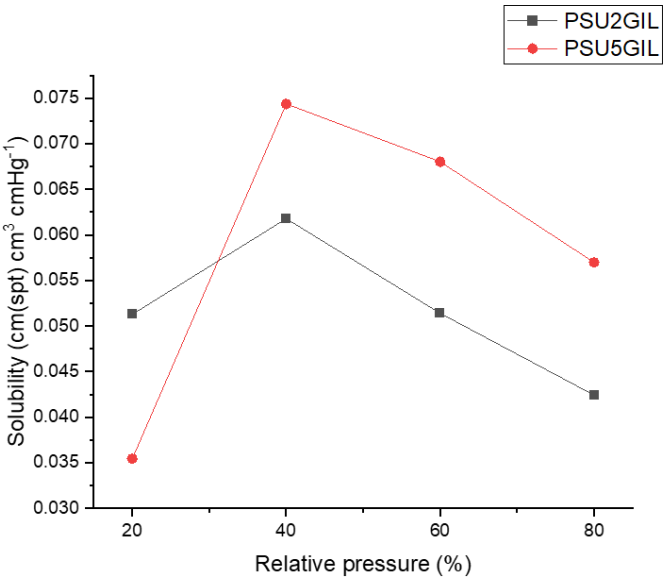

(a)

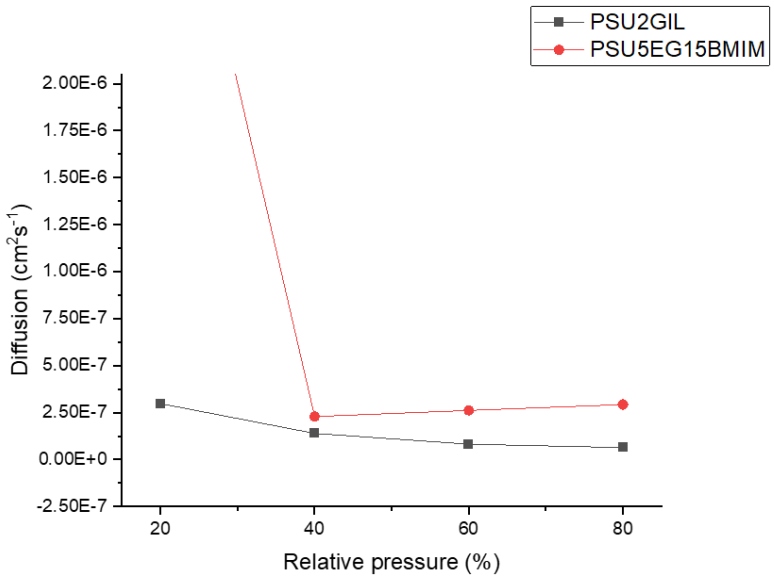

(b)

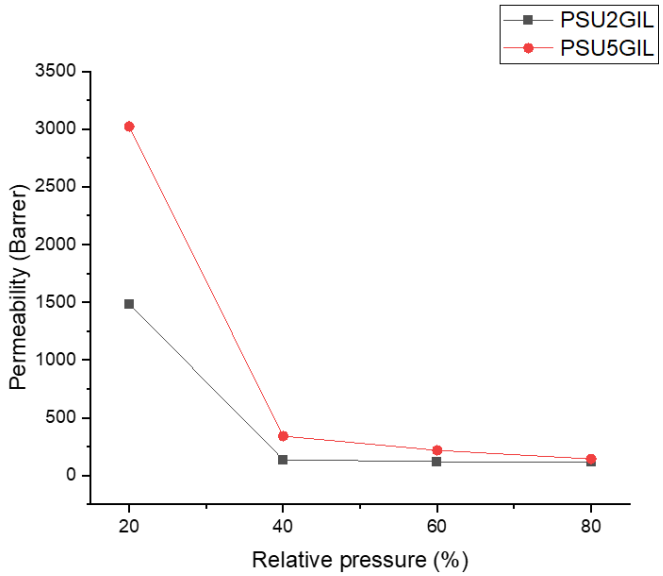

(c)

Figure 57 Gas Performance, the solubility (a) diffusion(b) and permeability (c), of MMM PSU-EG with ionic liquids in N_2 atmosphere

The difficulty in diffusion through the membranes containing ionic liquid is also observed to some extent in studies conducted in a N_2 atmosphere. As mentioned earlier, measurements in N_2 were not feasible using the microbalance due to their

low solubility in most of the studied membranes. However, when considering the presence of both ionic liquid and graphene, it becomes more challenging for N_2 to traverse the membrane's cross-section.

Comparing the obtained data, it is observed that N_2 is absorbed more easily and exhibits greater diffusion in the membrane containing 5% graphene. This suggests that this particular membrane possesses higher selectivity for N_2 gas.

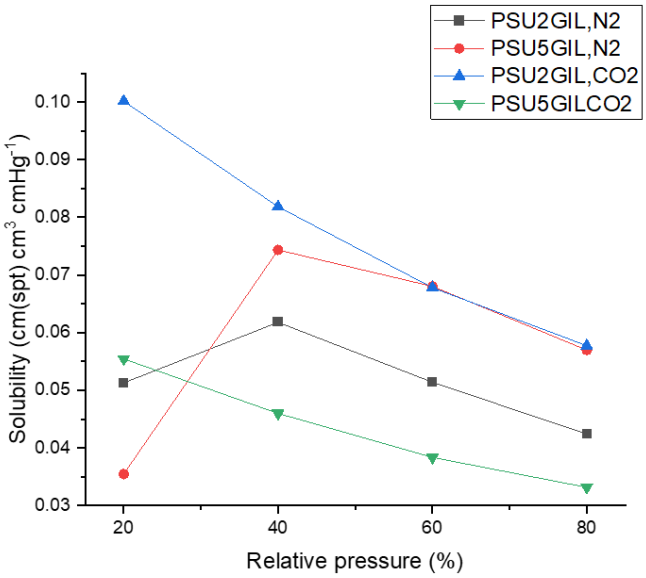

(a)

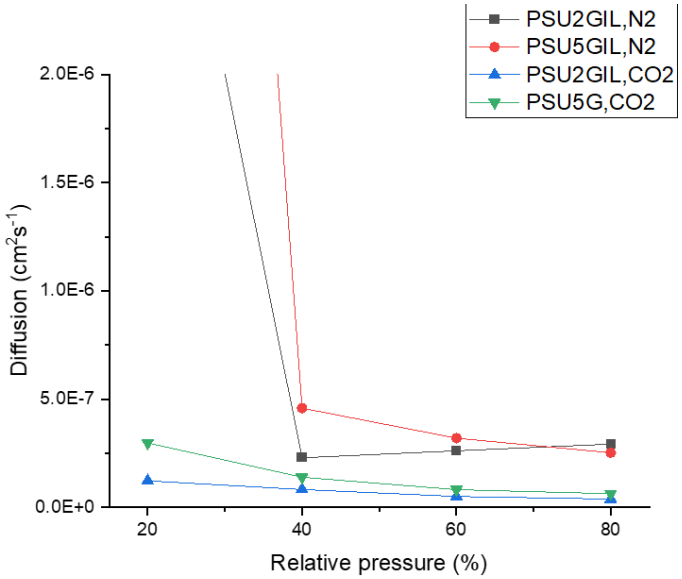

(b)

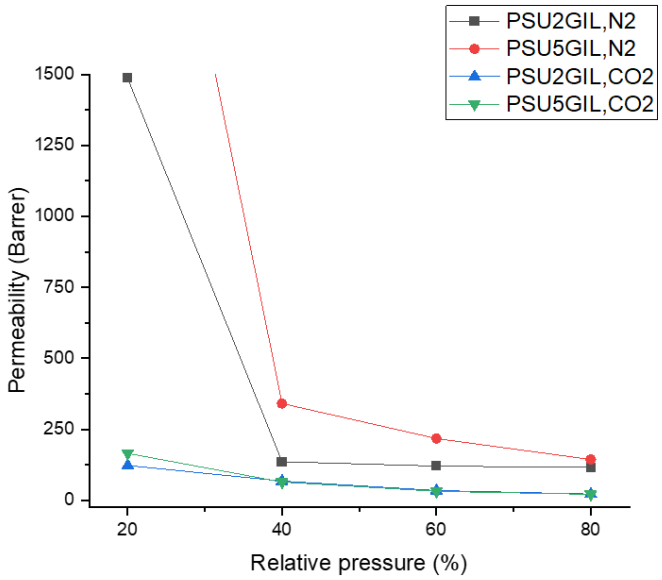

(c)

Figure 58 Comparison of performance in N_2 atmosphere and CO_2 atmosphere, of membranes PSU containing EG and BMIM

By comparing the data obtained in the CO_2 atmosphere and N_2 atmosphere it can be seen that in the membrane at 5% EG N_2 dissolves with a very similar trend to that of CO_2 with the membrane at 2%, in both membranes, it can be said that N_2 diffuses preferentially in comparison with N_2, and also from the permeability a higher selectivity of these membranes is observed in particular of PSU5GIL not to CO_2 but to N_2 that passes more easily.

4.1.2 GEM [PSU] Wafer

Based on the results obtained from the membranes composed of PSU and graphene, it was determined to prepare a PSU-based membrane coated with a layer of GEM dispersed in ethanol using an airbrush technique.

Figure 59 presents the morphological analysis of the PSU membrane using FESEM. The analysis reveals the presence of a compact layer uniformly coating the surface of the PSU membrane. Importantly, no indications of pore damage or disruption in the underlying membrane structure are observed. The GEM coating

exhibits an average thickness of 18 microns on each side, contributing to approximately 32% of the overall membrane thickness.

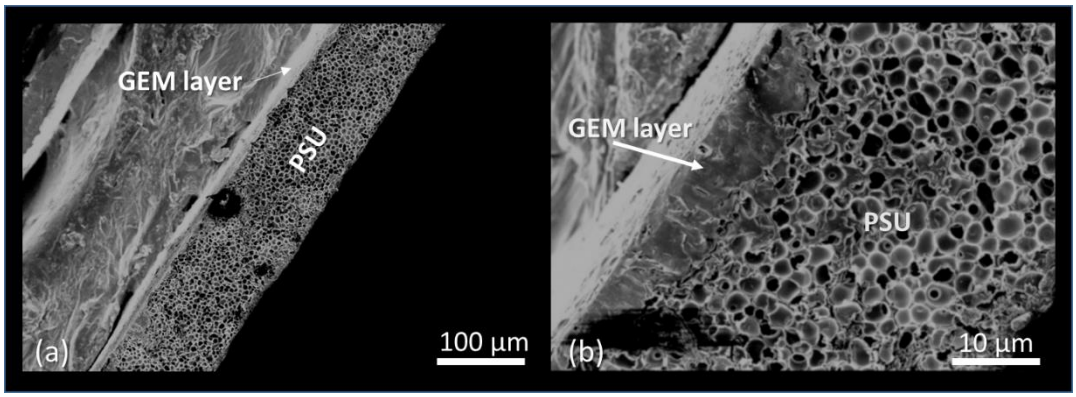

Figure 59 FESEM Morphological Analysis of PSU Membrane Coated with GEM

Based on the permeability studies conducted on the GEM-coated PSU membrane Figure 60), it is observed that the presence of GEM enhances diffusion and permeability compared to the normal PSU membrane. The GEM coating creates a surface that is more favorable for CO_2 adsorption and absorption, leading to an increased concentration of the gas within the membrane. Additionally, the GEM coating does not significantly impede diffusion, resulting in improved performance.

Comparing the GEM-coated membrane with membranes containing exfoliated graphene, it is notable that although the solubility values of GEM[PSU] Figure 60a are like those obtained with the membrane containing 5% EG (which exhibited lower CO_2 performance among the PSU-EG membranes), the diffusion through the GEM-coated membrane yields significantly higher results Figure 60b. This high diffusion, combined with relatively lower solubility, results in an intermediate permeability value that is higher than that obtained with 5% graphene in the matrix Figure 60c.

In future studies, it would be worthwhile to further investigate the interaction between GEM and PSU within the polymer matrix. Since GEM is a nanocomposite enclosed by a polymer layer on its surface, the interaction between this material and PSU may differ from that of exfoliated graphene; due to the different interaction GEM could have with the organic matrix (polymer-polymer interaction), different to that of graphene (polymer-inorganic interaction).

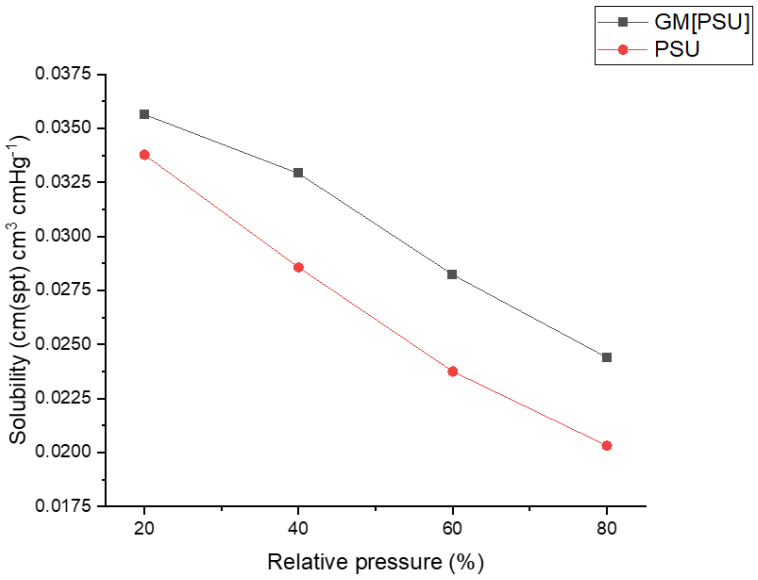
GM[PSU]
PSU
Solubility (cm(spt) cm3 cmHg-1)
0.0375
0.0350
0.0325
0.0300
0.0275
0.0250
0.0225
0.0200
0.0175
20
40
60
80
Relative pressure (%)

(a)

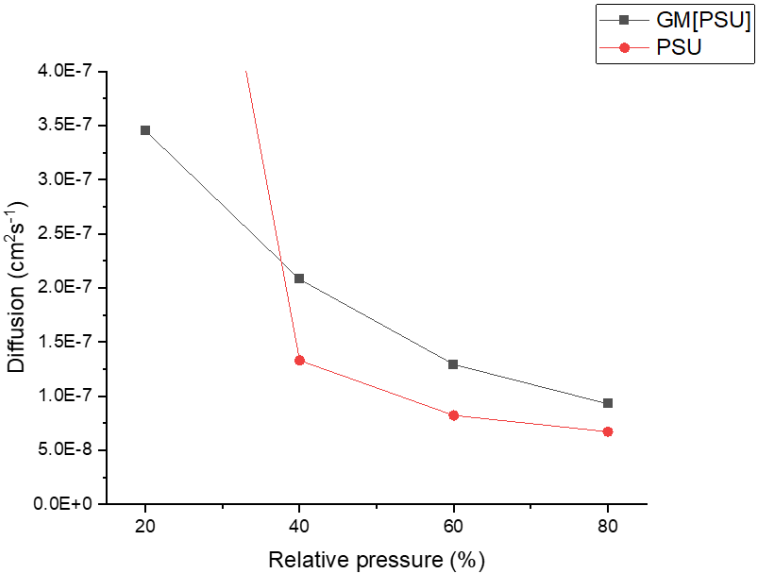
GM[PSU]
PSU
Diffusion (cm2s-1)
4.0E-7
3.5E-7
3.0E-7
2.5E-7
2.0E-7
1.5E-7
1.0E-7
5.0E-8
0.0E+0
20
40
60
80
Relative pressure (%)

(b)

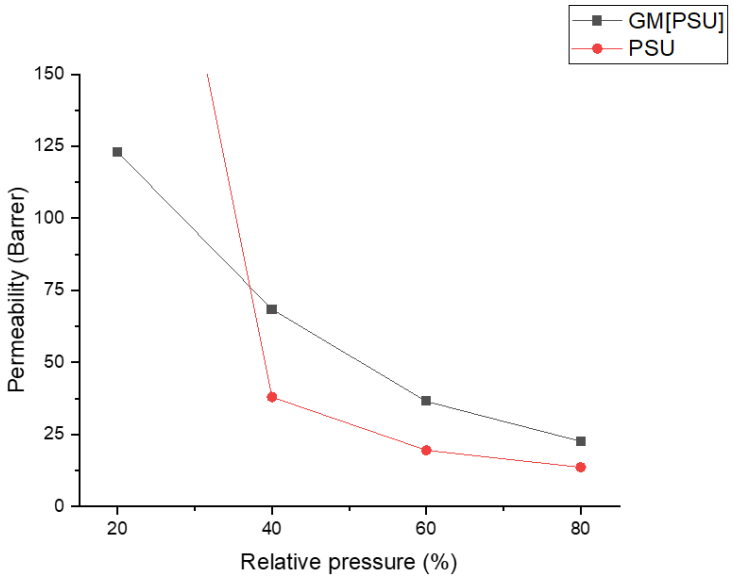

(c)

Figure 60 CO_2 Solubility (a), Diffusion (b), and Permeability (c) of PSU Membrane Coated with GEM compared to Normal PSU.

4.2PIM-1-based membrane

4.2.1 PIM-1 membrane mixed with graphene

To understand which solvent was the most appropriate for the solvent casting technique with PIM-1 membranes, a comparison was made between chloroform and a 50:50 mixture of chloroform and tetrahydrofuran (THF), based on the electrospinning study conducted by Wongwilawan et al. [116]The use of the 50:50 mixture in the electrospinning technique resulted in the formation of hyper porous filaments.

By conducting a morphological analysis of the two membranes using ESEM microscopy (see Figure 61), distinct differences in the cross-section of the membranes were observed. The membrane prepared using only chloroform showed a compact cross-section with a wrinkled surface. On the other hand, the use of the THF/$CHCl_3$ mixture resulted in the formation of wide cross channels crossing the membrane Figure 61b.

While the membrane prepared with the THF/$CHCl_3$ mixture may initially seem more promising, it is important to note that the main characteristic of PIM-1 is its

composition of a porous network with dimensions in the Dalton range, which are difficult to detect with the ESEM technique. These pores are what contribute to the rough surface observed in morphological analysis using this technique. Due to this reason, it was decided to continue the preparation of membranes containing the nanomaterial, graphene-based, using chloroform as the solvent.

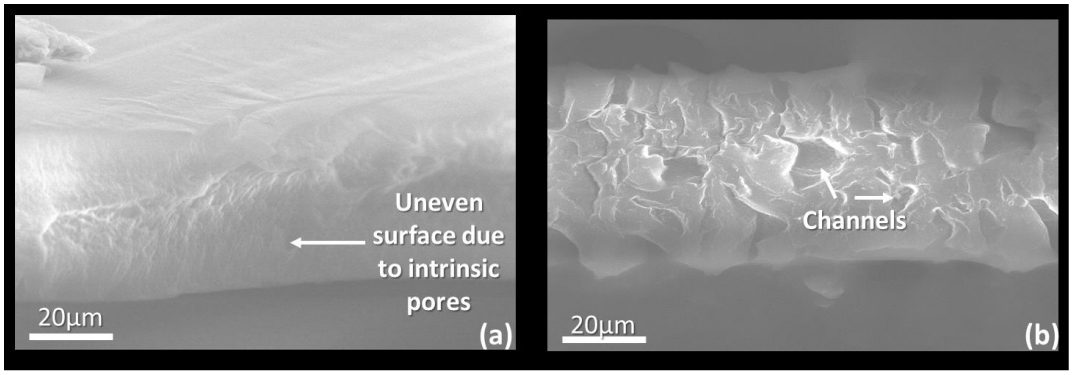

Figure 61 Morphological analysis of the cross-section of PIM-1 membranes prepared using different solvents. (a) PIM-1 prepared with CHCl3: (b) PIM-1 prepared with a 50:50 mixture of $CHCl_3$/THF

Analysis using the FESEM technique provided additional morphological insights into the PIM-1 membranes (Figure 62). Unlike the ESEM technique, the FESEM technique revealed a more detailed surface of the cross-section. It showed that the rough and irregular surface observed with ESEM is a network of interconnected polymeric filaments. This type of porosity is also evident in the PIM(GTCNE) membrane, where distinct holes and areas of higher density are more prominently observed. These variations in porosity and density are likely attributed to the presence of carbon nanomaterial in the polymer matrix, which causes contraction and structural changes in the membrane [117].

The morphological data obtained through FESEM analysis provides valuable information for understanding the results obtained from the thermogravimetric analysis. It helps to elucidate the relationship between the membrane's microstructure and its thermal properties.

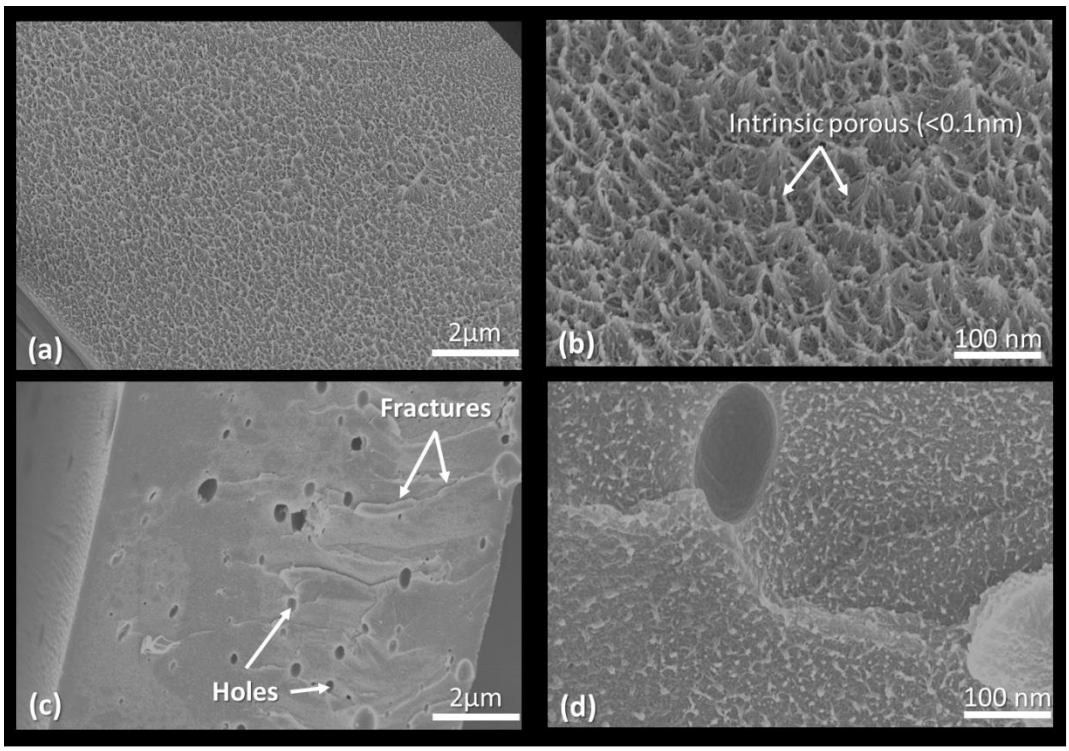

Figure 62 FESEM analysis of the cross-section of PIM-1 membranes (a, b) and PIM(GTCNE) membranes (c, d)

Figure 63 presents the TGA results, comparing the thermal behavior of PIM-1 and PIM-1 membranes containing graphene functionalized with tetracyano ethylene (a), as well as the TGA analysis of the PIM-1 membrane containing graphene functionalized with and ionic liquid BMIM-Suc (b). Comparing the thermogravimetric analysis (TGA) of PIM-1 and PIM-1 membranes containing graphene functionalized with tetracyano ethylene (PIM(GTCNE)), two distinct degradation phases can be observed. In the first phase, the maximum degradation temperature is 160°C for PIM(GTCNE) and 184°C for PIM-1. This mass loss primarily occurs in the PIM(GTCNE) membrane, and it is attributed to the removal of residual DMF from the polymer matrix after synthesis. The rapid mass loss observed in the graphene-containing membrane can be attributed to its unique structure, characterized by larger channels compared to the pure membrane, which has a much smaller pore size.

The second mass loss corresponds to the actual degradation of the membrane, and the maximum degradation temperature is observed at 515°C for PIM-1. In contrast, when the membrane contains graphene, the maximum degradation temperature is approximately 523°C. This indicates that the presence of graphene

imparts greater thermal resistance to the membrane. The enhanced thermal stability of the PIM(GTCNE) membrane can be attributed to the reinforcing effect of graphene in the polymer matrix.

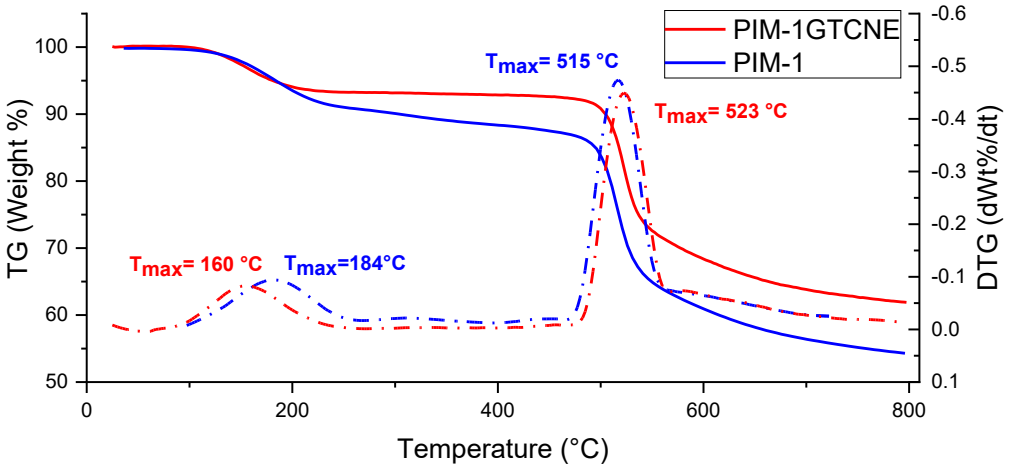

(a)

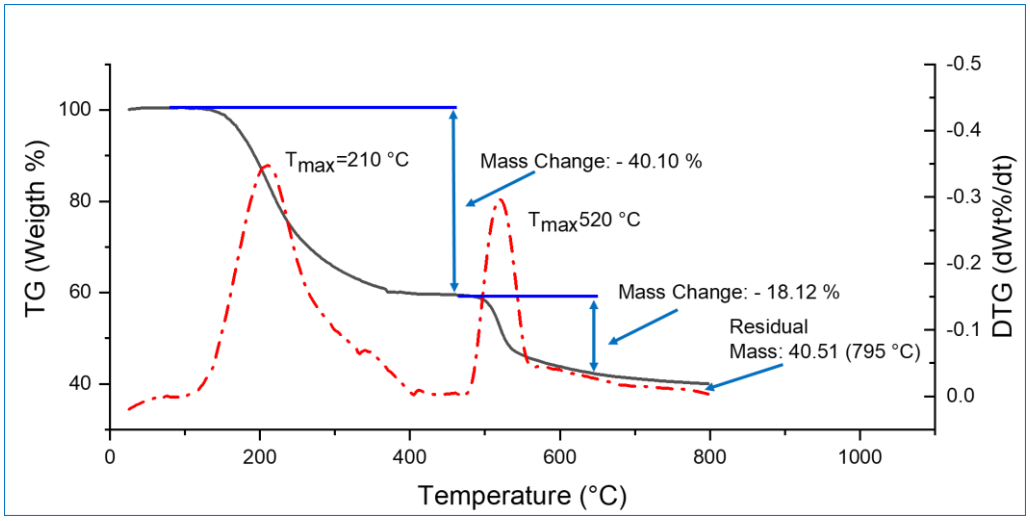

(b)

Figure 63: Thermogravimetric analysis (TGA) comparison of PIM-1 and PIM(GTCNE) membranes (a), and TGA analysis of PIM(GTCNE)IL (b)

In the case of PIM-1, the glass transition is not easy to detect; studies on the polymer have shown that the glass transition is around 400-440°C, a temperature very close to the decomposition temperature of the material, which leads to difficulties in measuring this physical characteristic by the DSC technique.

The degradation behavior of the membrane containing the ionic liquid is characterized by two distinct phases. The first degradation phase occurs with a maximum of 208 °C, involving the loss of both the solvent traces and the ionic liquid. The second degradation phase occurs around 520 °C, indicating the thermal resistance effect imparted by graphene, which remains effective even in the presence of the ionic liquid.

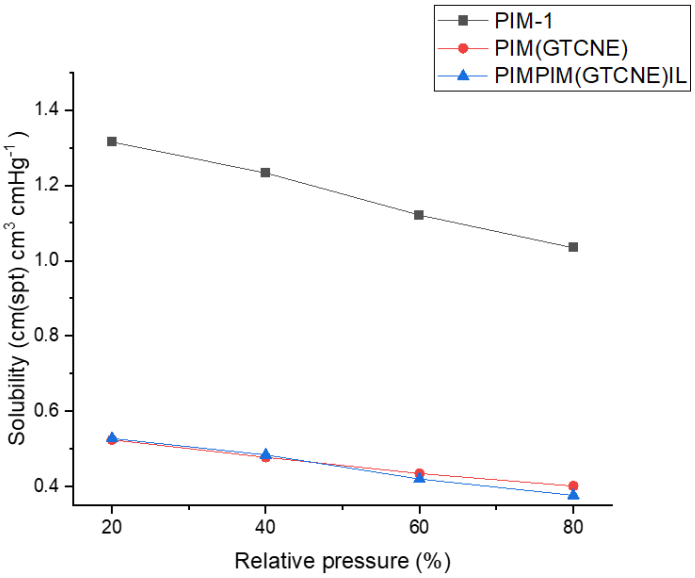

Figure 64 Comparison of solubility between PIM-1 membranes, PIM-1GTCNE, and PIM-1GTCNE with BMIM Succ.

The study of the permeability and diffusion of pure PIM-1 was not feasible using microbalance measurements. This is attributed to the significantly high solubility of CO_2 in PIM-1, and the diffusion to high to measure condition, as depicted in Figure 64. The solubility of CO_2 in PIM-1 is considerably higher compared to other membranes, rendering the adsorption kinetics incongruent with the actual values. To address this limitation, parallel investigations were conducted on PIM-1 membranes incorporated with ionic liquids BMIM acetate and BMIM Succ [88] Solubility measurements were determined using a microbalance, while diffusion and permeability assessments necessitated the utilization of a flow system connected to a micro gas chromatogram, which was originally employed for N_2 permeability studies.

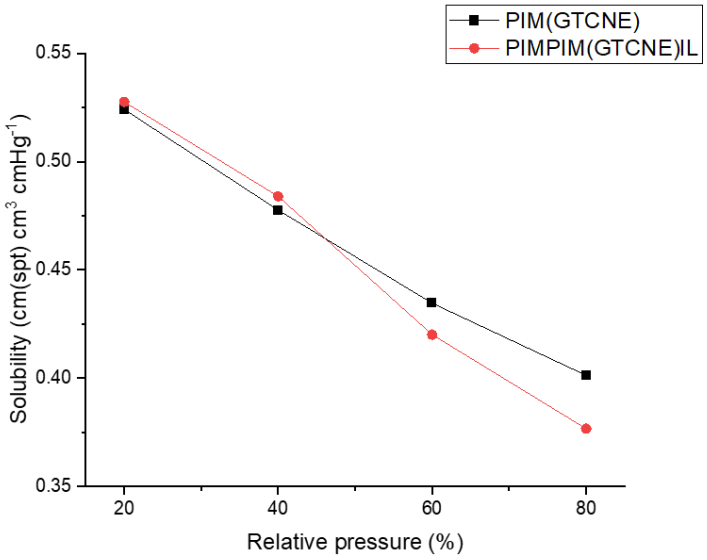
PIM(GTCNE)
PIMPIM(GTCNE)IL
Solubility (cm(spt) cm^3 cmHg^{-1})
0.55
0.50
0.45
0.40
0.35
20
40
60
80
Relative pressure (%)

(a)

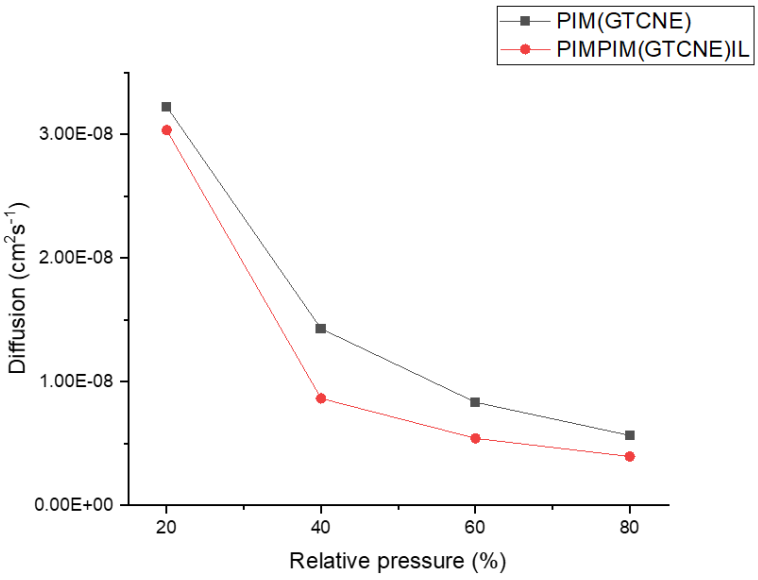
PIM(GTCNE)
PIMPIM(GTCNE)IL
Diffusion (cm^{2}s^{-1})
3.00E-08
2.00E-08
1.00E-08
0.00E+00
20
40
60
80
Relative pressure (%)

(b)

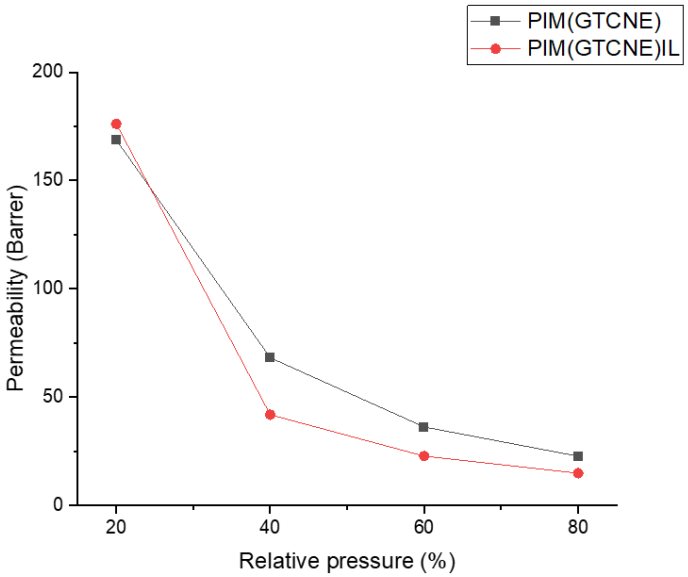

(c)

Figure 65 Comparison of gas performance of PIM(GTCNE) with and without BIMIM Succ in CO_2 atmosphere, Solubility 8a) diffusion (b) and Permeability(c) are reported.

Unfortunately, during the Ph.D. it was not possible to be able to measure the performance of the membranes by this method; however, it is planned to continue the study to obtain a better comparison with the PIM-1 membrane.

Regarding the diffusion permeability and solubility study of PIM(GTCNE) and PIM(GTCNE)IL membranes, it was possible to measure CO_2 permeability with better accuracy.

It is observed that the two membranes containing the carbon nanomaterial, with and without the ionic liquid have a very similar solubility to CO_2, as the concentration of CO_2 in the system increases, a higher solubility is observed in the membrane containing only the PIM(GTCNE) which has a much more linear trend with increasing CO_2, with the ionic liquid on the other hand we have a decrease when CO_2 reaches a relative pressure of 60%

From the diffusion data it can be seen that CO_2 is more easily able to pass through the membrane containing only the functionalized graphene, this is probably caused by the viscosity of the ionic liquid slowing down the passage of CO_2 through the membrane, the gas having to dissolve in the liquid and interact chemically with it.

Although from the data obtained, the solubility of the gas is far greater in the presence of the ionic liquid.

Diffusion through this membrane is much slower, L PIM-1 membranes containing GTCNE is probably favored by the presence of surface irregularities caused by the contraction of the polymer decreased the space present between the pores, and created cracks in the cross section, with the further addition of the ionic liquid that goes to occupy the cracks created we have a dramatic lowering of the performance of these membranes at the diffusion level.

4.2.2 PIM-1[PSU], PIM-1(GTCNE)[PSU] and the mixed composite membrane PSU/PIM-1.

In Figure 66, the morphological analysis of wafer membranes coated with PIM-1 and PIM(GTCNE) reveals distinct surface characteristics. The PIM-1-coated membrane exhibits a layer rich in cracks and channels, resulting in a highly porous surface. In some areas, openings on the PIM-1 surface expose the central membrane layer. On the other hand, the PIM(GTCNE)-coated membrane, serving as the outer layer, exhibits an irregular but denser and more compact surface. Some seepage from the underlying layer is observed in certain regions, possibly attributed to the use of chloroform during the coating process. In the cross-section, a noticeable difference is observed in pore sizes, with the PIM-1 layer exhibiting smaller pores compared to the larger pores of the PSU layer. The porosity of the PIM-1-coated membrane is more challenging to discern.

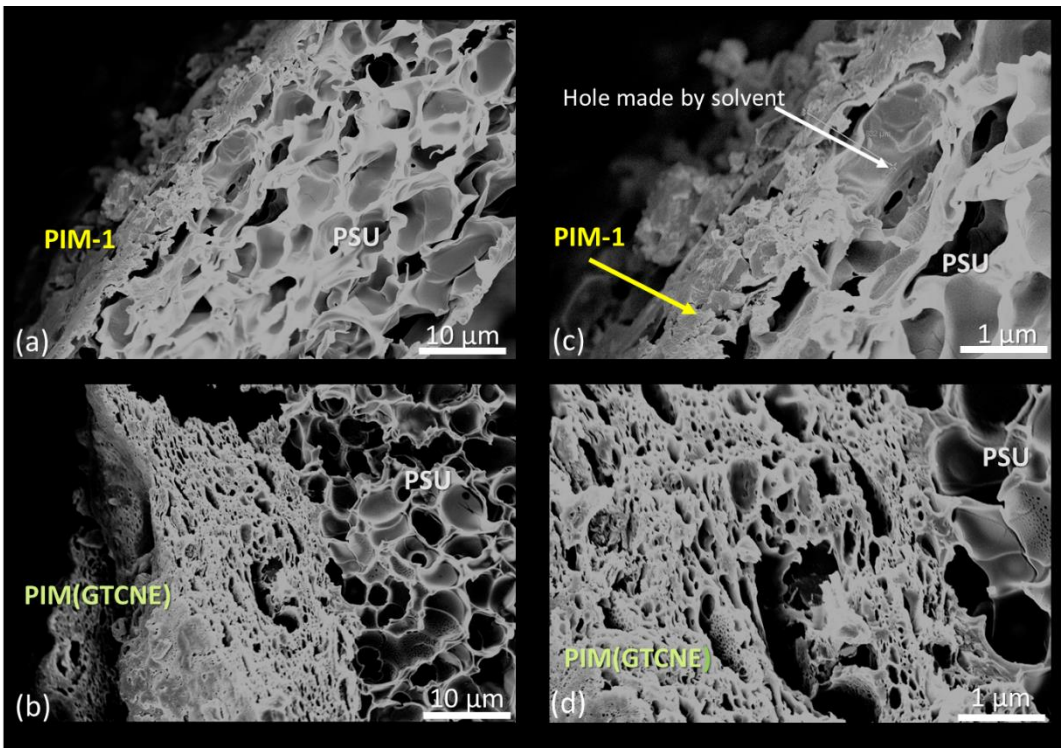

Figure 66 Morphological analysis done with al FESEM microscopy of PIM[PSU] membrane at 100 and 10 µm (a,b) and of PIMGTCNE[PSU](c,d)

From the performance analysis of the PIM[PSU] and PIM(GTCNE)[PSU] membranes, it is evident that the presence of a thin layer of PIM-1 has a significant impact on the solubility of CO_2. Compared to PSU alone, the affinity of the material for CO_2 increases when PIM-1 is incorporated. Moreover, the combination of PIM-1 and graphene on the membrane surface exhibits positive effects on performance. The gas diffusion through the cross-section is accelerated, resulting in a noticeable enhancement in PSU permeability when both PIM-1 and graphene are present. These findings pave the way for further studies and the potential design of unidirectional bilayer membranes.

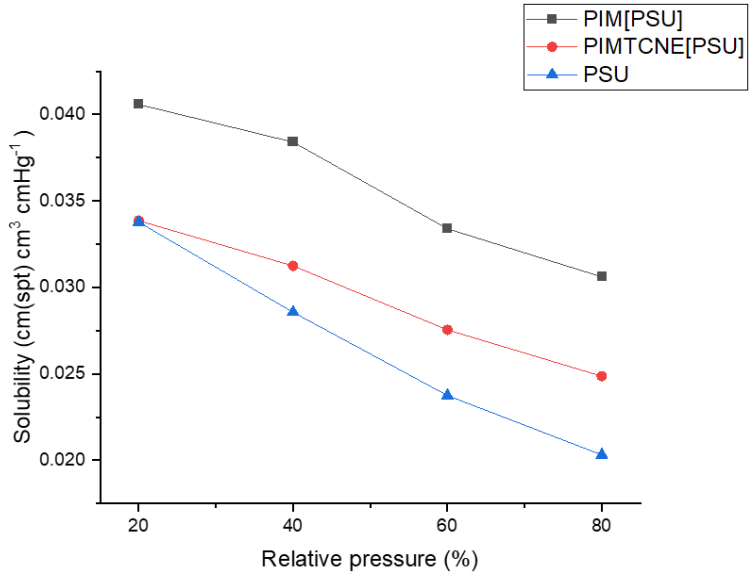
PIM[PSU]
PIMTCNE[PSU]
PSU
Solubility (cm(spt) cm^3 cmHg^{-1})
0.040
0.035
0.030
0.025
0.020
20
40
60
80
Relative pressure (%)

(a)

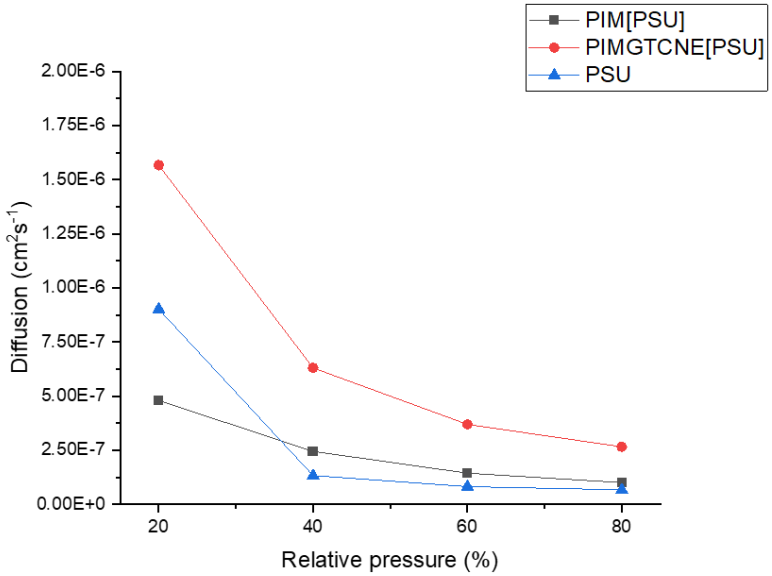
PIM[PSU]
PIMGTCNE[PSU]
PSU
Diffusion (cm^{2}s^{-1})
2.00E-6
1.75E-6
1.50E-6
1.25E-6
1.00E-6
7.50E-7
5.00E-7
2.50E-7
0.00E+0
20
40
60
80
Relative pressure (%)

(b)

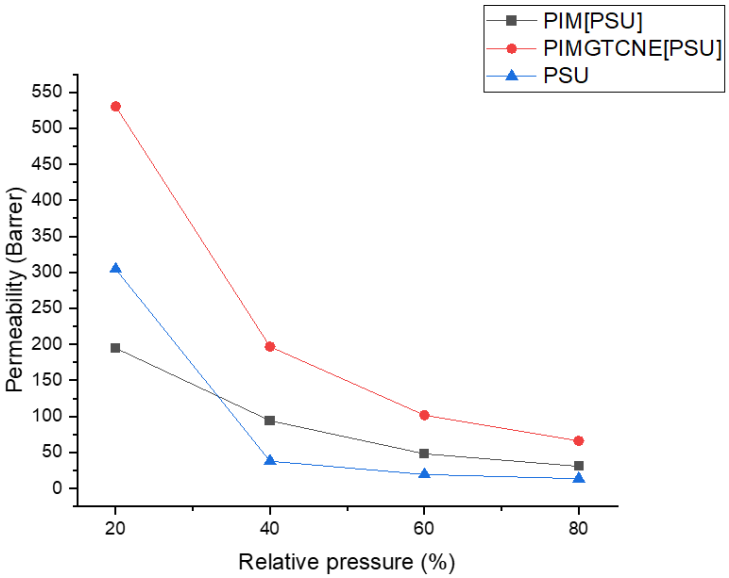

(c)

Figure 67 Comparison of Solubility (a) diffusion (b) and permeability(c) of multilayer membranes PIM[PSU], PIMTCNE[PSU] compared with PSU performance

Regarding the membrane composed of 25% PIM-1 and 75% PSU, a heterogeneous structure is observed on both sides of the membrane, likely due to the spreading and drying process on the substrate. One side of the membrane exhibits narrow and elongated channels with an average width of 3.7 microns and depths ranging from 16 to 30 microns. These channels are separated by smaller pores similar to those formed when spreading pure PSU, albeit even narrower. On the other side of the membrane, the channels run parallel to the surface with larger diameters. Upon closer examination of the surfaces that connect the channels and pores, interconnected holes can be observed, facilitating the exchange between different regions of the membrane.

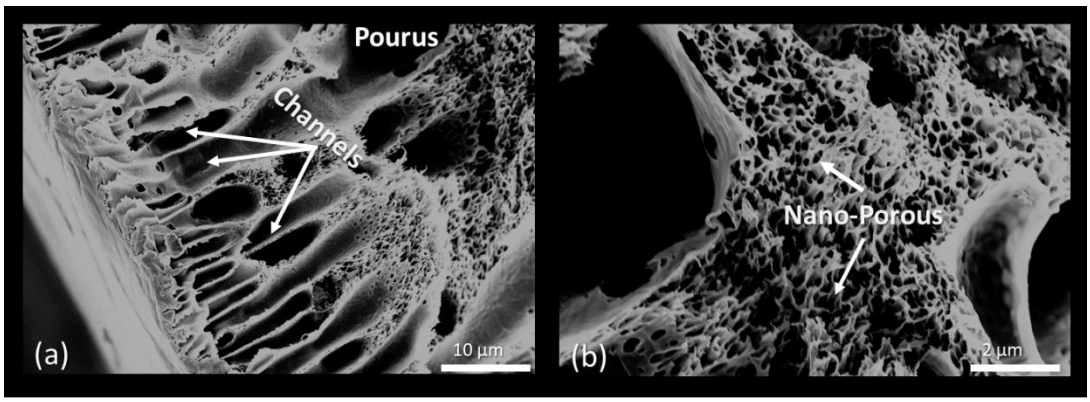

Figure 68 FESEM microscopy analysis of PSU/PIM-1 observed at a magnification of 10µm (a) and 2 µm (b).

Once again (Figure 69), the permeability analyses reveal the positive impact of PIM-1 on PSU. Firstly, the solubility of CO_2 in the membrane significantly increases when PIM-1 is incorporated, allowing for higher absorption of the gas compared to pure PSU. Additionally, the presence of PIM-1 moderately enhances the gas diffusion capacity through the membrane. The increased number of channels in the composite membrane comes at the expense of the number of pores. As a result, the membrane could accumulate a larger amount of gas, which subsequently follows a more tortuous path through the pores in the cross-section, leading to an increased residence time within the membrane. However, this residence time is still shorter than that of the gas in the pure PSU membrane.

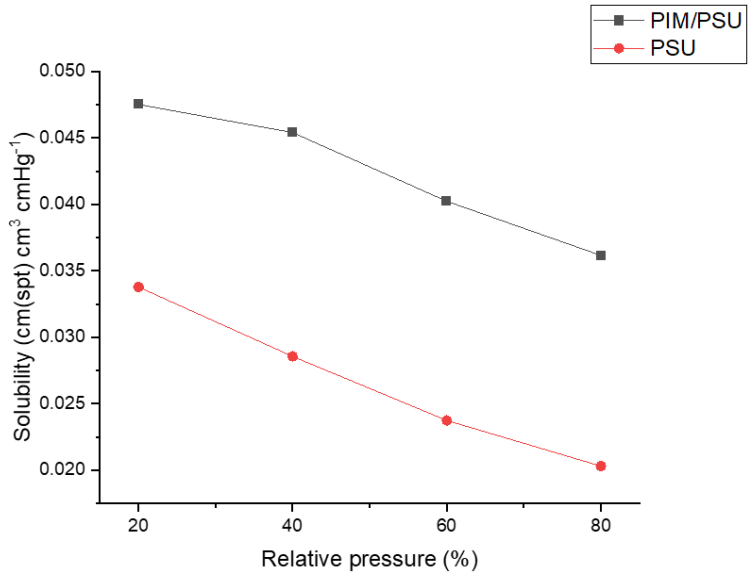
PIM/PSU
PSU
Solubility (cm(spt) cm^3 cmHg^{-1})
0.050
0.045
0.040
0.035
0.030
0.025
0.020
20
40
60
80
Relative pressure (%)

(a)

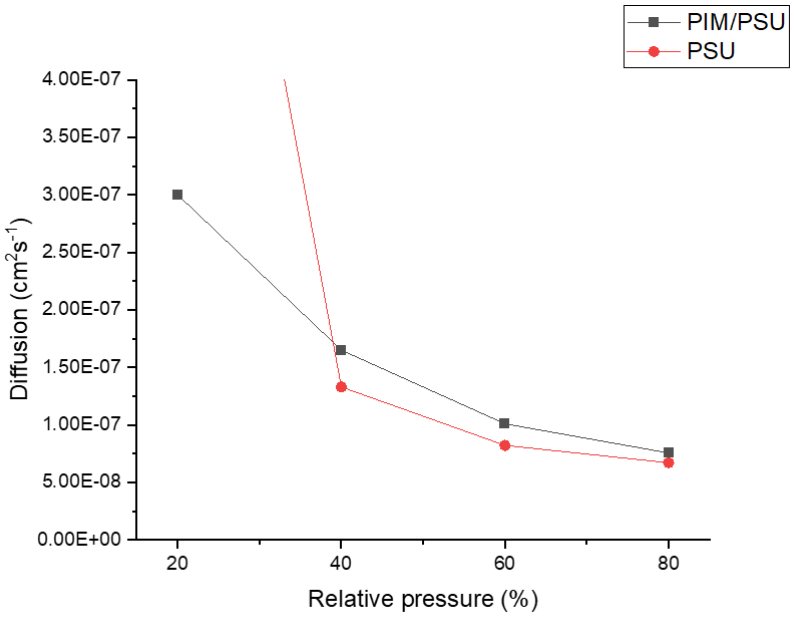
PIM/PSU
PSU
Diffusion (cm^{2}s^{-1})
4.00E-07
3.50E-07
3.00E-07
2.50E-07
2.00E-07
1.50E-07
1.00E-07
5.00E-08
0.00E+00
20
40
60
80
Relative pressure (%)

(b)

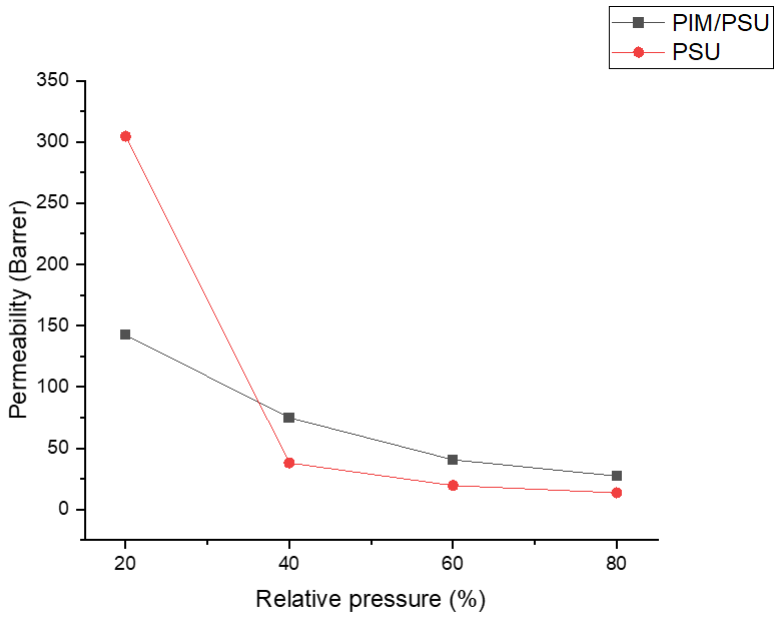

(c)

Figure 69 Gas performance Solublity (a),Diffusion(b) and Permeability(c) in CO_2 of the PSU/PIM-1 composite membrane compared to the PSU membrane.

4.2.3 Composite membrane PIM-1 with Ionic liquids BMIMSucc and BMIM acetate

Part of the work described in this chapter was also previously published in "ILs-modified membranes based on Polymers of Intrinsic Microporosity (PIMs) for CO2 separation"[88]

In this paragraph, a study done in parallel with PIM-1 mixed with different concentrations of BMIM Succimidate (BMIMSuc) and BMIM acetate (BMIMac) will be quickly discussed

4.2.3.1 Composite membrane PIM-1 with different concentrations of Ionic liquids BMIMSucc and BMIM acetate

ATR was performed on blended membranes and bare PIM-1 membranes to prove the successful introduction of ILs within the PIM1-based films. All spectra are shown in Figure 70. In the PIM-1 membrane spectrum, the typical peaks of the

polymer are present. In particular, the C-O-C stretching peak of the aromatic ethers and the CN stretching of the nitrile group at 2240 cm-1 is present [118]. The imidazolium in-plane ring modes present in both ILs are located at (∼1560 cm^{-1}) for [BMIM][Ac] and [BMIM][Succ] [119]. In Figure 70a the presence of [BMIM][Succ] in the membrane is confirmed by the presence of the peak at 1558 cm^{-1} referring to the carbonyl stretching peak of succimidate anion of [BMIM][Succ]. The appearances of characteristic bands for [SUC]- anion at 1695 cm−1 and 1064 cm−1 are attributed to C=O and C–N[120]. As expected, the increase of the typical ILs peaks intensities is directly linked with the increase of ILs % in the blend.

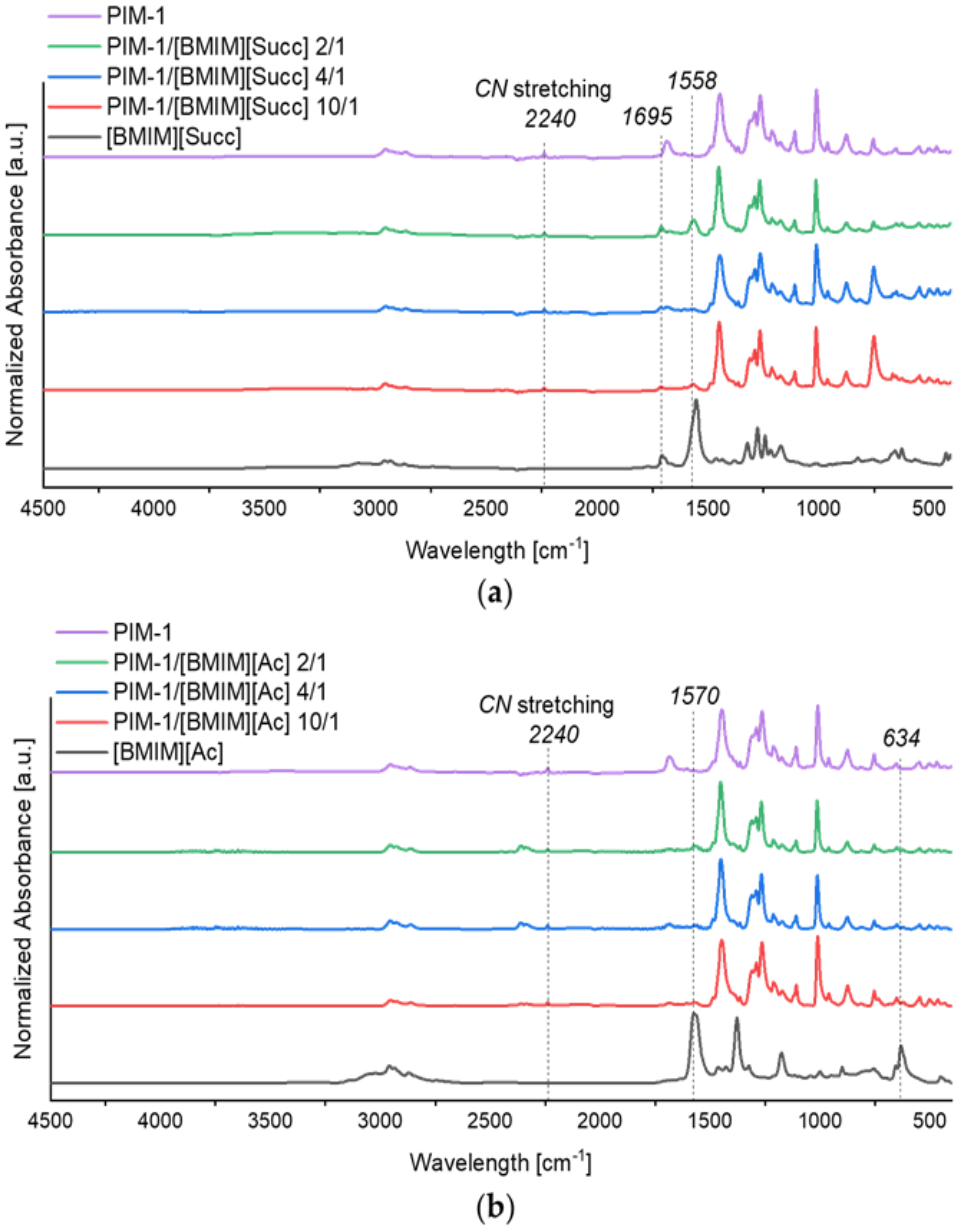

Figure 70 Infrared spectra of PIM-1 membrane compared with PIM-1 composite membrane with different concentrations of BMIM Succ(a) and different concentrations of BMIM Ac (b)

The imidazolium vibration partially superimposes with the asymmetric stretching (1570 cm^{-1}) of the ATR spectra reported in Figure 70b of the acetate anion of [BMIM][Ac] [121]. The acetate bending is instead at 634 cm^{-1}. The presence of both absorption in PIM-1/[BMIM][Ac] blends is shown, confirming the successful incorporation ILs in PIM-1 polymer.

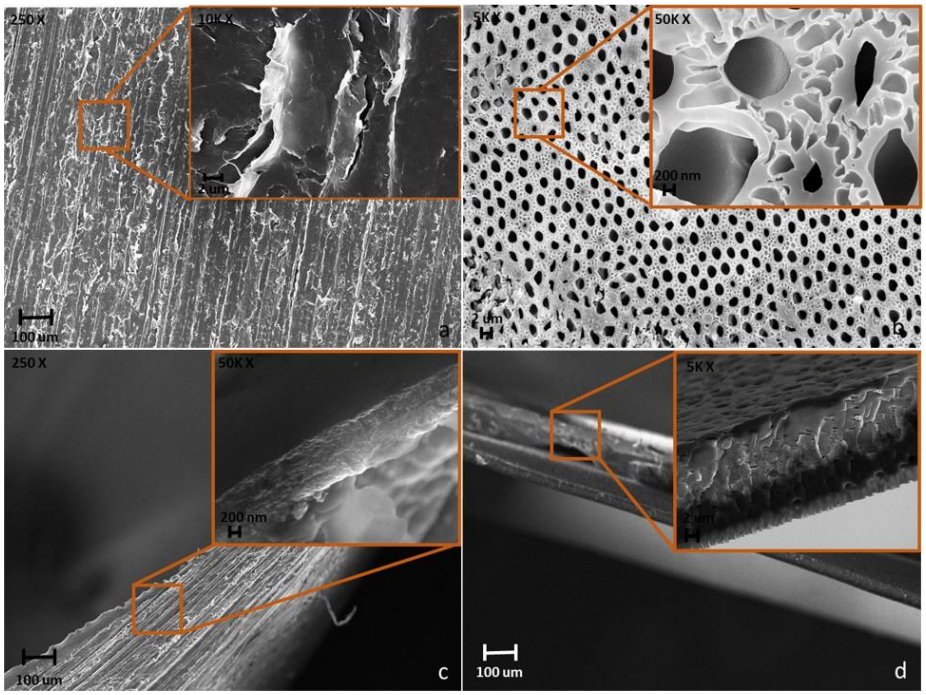

Figure 71 FESEM capture of surface (a) PIM-1, (b) PIM-1/[BMIM][Ac] 10% and their cross sections (c) and (d) respectively

The FESEM capture of representative of the membrane with and without the addition of ILs. PIM-1 showed a smooth surface without an appreciable porous network with cracks due to the intrinsic brittleness of the polymeric film as shown in Figure 71a highlight. As reported in Figure 71c, the PIM-1 cross section shows a thick range from 13 up to 20 µm confirming the absence of diffuse pores. The PIM1/ILs showed a very different topology characterized by porous with an average diameter size of up to 1.5-µm (Figure 71b). Furthermore, the cross-section for the sample shown in Figure 71d shows the presence of small channels inside the film bulk and average thickness comparable with neat PIM-1. The FESEM analysis enlightens the porous formation as a consequence of the addition of ILs without altering the thickness of the specimens.

The solubility of CO_2 in PIM-1 is usually quite high due to the nitrile groups that may be assumed to enhance both the strength of intermolecular forces and, because of their lateral position, the free volume, giving rise to even higher apparent solubilities. The high apparent solubility of gases in PIMs thus it is attributed mainly to their microporous character, which provides a high capacity for gas [122].

Once [BMIM][Succ] is introduced, the CO_2 solubility in the blended membranes decreases in the first instance to the following order: 10,25,50% (Figure 72 a Table 14). Again, the blend with the 25% of IL has higher solubility compared to the other blended mem-branes; we speculate that there is a trade-off between the beneficial effect of ILs in enhancing the solubility and their "negative" limiting the free volume. Indeed, the limited free volume due to the ILs filling the empty voids of PIM-1 decreases the gas diffusion through the membrane. Moreover, the high viscosity of [BMIM][Succ] could further limit the diffusion of CO_2 in the membrane. Thus, despite the high solubility of CO_2 in [BMIM][Succ], which could reach an uptake of 10.9%w at CO_2 pressure of 1 bar, the inclusion of these ILs in-to the membrane decreases the total solubility (Figure 72aTable 14).

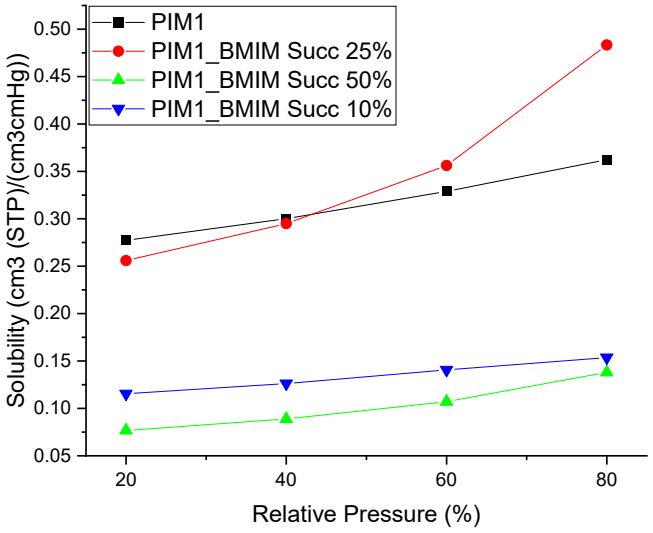

(**a**)

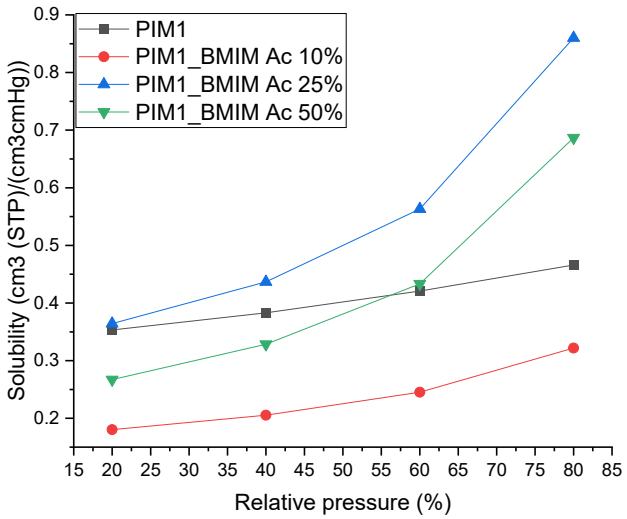

(b)

Figure 72 Comparison of CO_2 solubility between PIM-1 pure membrane with 10,25,50,% of BMIM Succ. (a) and with 10,25,50% of BMIM Ac (b) insert the matrix of PIM-1

On the contrary, the solubility coefficient of CO_2 is found to increase significantly with the increment of [BMIM][Ac] from 10% to 50%, compared to pure PIM-1 membrane, with the higher increase in solubility for PIM-1/[BMIM][Ac] 25% reaching and surpassing the PIM-1 for high pressures (Figure 72, Table 14). This result was expected since [BMIM][Ac] has a high solubility specifically for CO_2 [123].

Table 14 CO_2 Solubility coefficients at 80% of relative pressure of CO_2 derived from the direct sorption experiments

Membrane	CO_2 Solubility 1
PIM-1	0.47
PIM-1/[BMIM][Succ] 10%	0.22
PIM-1/[BMIM][Succ] 25%	0.33
PIM-1/[BMIM][Succ] 50%	0.18
PIM-1/[BMIM][Ac] 10%	0.32
PIM-1/[BMIM][Ac] 25%	0.86
PIM-1/[BMIM][Ac] 50%	0.69

Chapter 5

Conclusions

4.1 Achievements

Throughout the three-year Ph.D., the primary objective has been to develop mixed-matrix membranes aimed at enhancing selectivity for specific gases. To achieve this, various graphene-based fillers were synthesized for subsequent incorporation into the polymer matrix. Two of these fillers demonstrate innovation and possess physical characteristics applicable in other fields beyond gas separation.

Firstly, a novel graphene-based nanocomposite, containing a small amount of ethyl maleate-based polymer matrix, was successfully developed. This nanocomposite can be dispersed in low-boiling polar solvents such as ethanol at a concentration of 1.10 mg/ml. The dispersion exhibits excellent stability, as confirmed by zeta potential studies, which revealed a relatively stable dispersion with a mean zeta potential ranging from 30 mV to 28 mV after one year. When a radical initiator is utilized, the nanocomposite exhibits enhanced stability in ethanol, reaching a mean zeta potential of 40 mV and maintaining it over an extended period.

The second graphene-based filler involves a novel Diels-Alder cycloaddition reaction occurring on the surface of graphene. The obtained data confirmed an increase in defects on the carbonaceous material's surface through Raman spectroscopy. X-ray diffraction analysis revealed a change in the crystalline structure before and after the reaction. This reaction can be completed in a short time using microwave irradiation. Remarkably, this material exhibits interesting physical characteristics, including fluorescence and conductivity, thereby opening doors to new applications in the field of energy.

The membranes developed in recent years can be categorized into three groups: PSU-based glassy polymer membranes, PIM-1-based membranes, and multilayer

membranes. PSU-based membranes, well-known for their gas separation capabilities and the specific pores they can form, were initially studied to determine the optimal concentration of graphene within the matrix for enhanced membrane performance. Analytical instrument data indicates that the presence of 1% to 2% graphene significantly improves membrane permeability, with an increase of 184% and 207% compared to pure PSU membranes for 1% graphene and 2% EG, respectively, at a CO_2 pressure of 0.4 bar (40% relative pressure).

The presence of the ionic liquid BMIM Succimidate decreases the permeability of graphene-containing membranes. However, it shifts the selectivity towards N_2 over CO_2, making these membranes practically not selective. In the case of PIM-1-based membranes, the high solubility of CO_2 in the polymer posed challenges in conducting realistic comparisons using the available analytical tools. Incorporating graphene functionalized with TCNE significantly reduces the solubility of CO_2, enabling evaluation and comparison of mixed matrix membranes prepared with PIM-1. A screening study was done with PIM-1 and BMIM Succ. and BMIM Ac. ionic liquids, we observed how BMIM Succ has a negative influence on CO_2 diffusion and solubility for PIM-1, and how this decreases when the concentration of the ionic liquid is very high. BMIM Ac on the contrary proved to be better as an ionic liquid, increasing the solubility to CO_2 for these membranes, in both cases the optimal concentration that best affects the solubility to the gas is 25%, above 25% a lowering of membrane performance is observed.

Plans involve utilizing an analyzer connected to a micro gas chromatography system to evaluate membrane permeability in comparison to pure PIM-1 at a pressure of 1 bar.

Regarding multilayer membranes, intriguing data was obtained. Membranes consisting of a PSU-based core body covered with a thin layer of either PIM-1 or PIM-1 mixed with GTCNE exhibit improved performance compared to PSU alone. The presence of the thin layer enhances CO_2 absorption when PIM-1 is present on the surface, while the inclusion of GTCNE in the PIM matrix facilitates preferential CO_2 diffusion toward the middle part of the PSU.

4.2 Perspectives

Many of the results obtained during these years of research have led to the development of innovative materials and, in some cases, with avenues of application beyond gas separation.

GEM turns out to be an ethanol-dispersible graphene filler, which can lead to the development of innovative graphene-based inks.

It is also planned, building on the data obtained in the study of PSU with EG and the GEM[PSU] multylayer membrane,to study the separation performance of MMMs containing this filler .

The second functionalization, with acetyl dicarboxylate, obtained on graphene gave equally innovative and interesting results. In the future, starting from the observed fluorescence effects, it is planned to study this effect for sensor type applications, currently the article concerning this material is under review. also it is planned to do studies related to the utiliod id this graphene material at the level of CO2 separation and ion exchange membranes in catalytic systems for CO2 conversion.

as explained in this thesis the designed membranes gave interested information regarding the separation of CO2 however it was decided to do a further separation study by means of a system we designed connected to a micro gas chromatograph, allowing us to observe at the pressure of 1 bar the permeability for CO2 and N2 the latter in particular is the gas that was more difficult to evaluate the membrane performance.

However, the study related to graphene PSU membranes gave a lot of useful data, in the future I plan to do two more qualitative analyses, from observation via TEM microscopy to give further data on the distribution of graphene in the membrane and mechanical studies by Dynamic mechanical analysis.

The study of multilayer membranes gave particularly interesting and innovative results, and in the future we plan to continue the development of these membranes both tri-layer and bi-layer, so as to design one-way membranes for CO2 separation

Also last project for the future and continue the study of PIM-1 membranes containing GTCNE, membranes that have given the least promising results at present, and investigate new preparation methods as well as change the filler to another functionalized graphene.

References

1. Noted, E. *’ ’There Is No Question Climate Change Is Happening. the Only Arguable Point Is What Role Humans Are Playing in It. ’ ’ - David Attenborough: Enviromental Awareness Note Book*; Amazon Digital Services LLC - Kdp Print Us, 2019; ISBN 9781099097065.

2. Hulme, M. *Exploring Climate Change through Science and in Society*; 2013; ISBN 9780415811620.

3. Kweku, D.; Bismark, O.; Maxwell, A.; Desmond, K.; Danso, K.; Oti-Mensah, E.; Quachie, A.; Adormaa, B. Greenhouse Effect: Greenhouse Gases and Their Impact on Global Warming. *J. Sci. Res. Reports* **2018**, *17*, 1–9, doi:10.9734/jsrr/2017/39630.

4. EPA Table 2-8 Inventory of U.S. Greenhouse Gas Emissions and Sinks, 1990 to 2020. *EPA Rep.* **2020**.

5. Brithish Petroleum ESG Datasheet 2020 Available online: efaidnbmnnnibpcajpcglclefindmkaj/https://www.bp.com/content/dam/bp/business-sites/en/global/corporate/pdfs/sustainability/group-reports/bp-esg-datasheet-2020.pdf.

6. Gerden, T. The Adoption of the Kyoto Protocol of t He United Nations Framework Convention on Climate Change. *Prisp. za Novejso Zgodovino* **2018**, *58*, doi:10.51663/pnz.58.2.07.

7. Bocchini, S.; Castro, C.; Cocuzza, M.; Ferrero, S.; Latini, G.; Martis, A.; Pirri, F.; Scaltrito, L.; Rocca, V.; Verga, F.; et al. The Virtuous CO2 Circle or the Three Cs: Capture, Cache, and Convert. *J. Nanomater.* **2017**, *2017*, 0–15, doi:10.1155/2017/6594151.

8. Lo Zingarelli - Lo Zingarelli Vocabolario Della Lingua Italiana-Lo Zingarelli (2019).

9. Freeman, B.; Yampolskii, Y.; Pinnau, I. *Mater. Sci. Membr. Gas. Vapor Sep*; 2006; ISBN 047085345X.

10. Mohanty, K.; Purkait, M.K. *Membrane Technologies and Applications*; 2011; ISBN 9781439805275.

11. Robeson, L.M. Correlation of Separation Factor versus Permeability for

Polymeric Membranes. *J. Memb. Sci.* **1991**, *62*, 165–185, doi:10.1016/0376-7388(91)80060-J.

12. Budd, P.M.; McKeown, N.B.; Ghanem, B.S.; Msayib, K.J.; Fritsch, D.; Starannikova, L.; Belov, N.; Sanfirova, O.; Yampolskii, Y.; Shantarovich, V. Gas Permeation Parameters and Other Physicochemical Properties of a Polymer of Intrinsic Microporosity: Polybenzodioxane PIM-1. *J. Memb. Sci.* **2008**, *325*, 851–860, doi:10.1016/j.memsci.2008.09.010.

13. Robeson, L.M.; Smith, Z.P.; Freeman, B.D.; Paul, D.R. Contributions of Diffusion and Solubility Selectivity to the Upper Bound Analysis for Glassy Gas Separation Membranes. *J. Memb. Sci.* **2014**, *453*, 71–83, doi:10.1016/j.memsci.2013.10.066.

14. Freeman, B.D. Basis of Permeability/Selectivity Tradeoff Relations in Polymeric Gas Separation Membranes. *Macromolecules* **1999**, *32*, 375–380, doi:10.1021/ma9814548.

15. Breck, D.. W. *Zeolite Molecular Sieves*; Wiley-Interscience, Ed.; New York, 1974;

16. Robeson, L.M.; Dose, M.E.; Freeman, B.D.; Paul, D.R. Analysis of the Transport Properties of Thermally Rearranged (TR) Polymers and Polymers of Intrinsic Microporosity (PIM) Relative to Upper Bound Performance. *J. Memb. Sci.* **2017**, *525*, 18–24, doi:10.1016/j.memsci.2016.11.085.

17. Farnam, M.; Mukhtar, H.; Shariff, A.M. A Review on Glassy Polymeric Membranes for Gas Separation. *Appl. Mech. Mater.* **2014**, *625*, 701–703, doi:10.4028/www.scientific.net/AMM.625.701.

18. Aghaie, M.; Rezaei, N.; Zendehboudi, S. A Systematic Review on CO2 Capture with Ionic Liquids: Current Status and Future Prospects. *Renew. Sustain. Energy Rev.* **2018**, *96*, 502–525, doi:10.1016/j.rser.2018.07.004.

19. Zeng, S.; Zhang, X.; Bai, L.; Zhang, X.; Wang, H.; Wang, J.; Bao, D.; Li, M.; Liu, X.; Zhang, S. Ionic-Liquid-Based CO2 Capture Systems: Structure, Interaction and Process. *Chem. Rev.* **2017**, *117*, 9625–9673, doi:10.1021/acs.chemrev.7b00072.

20. Dai, Z.; Noble, R.D.; Gin, D.L.; Zhang, X.; Deng, L. Combination of Ionic Liquids with Membrane Technology: A New Approach for CO2 Separation. *J. Memb. Sci.* **2016**, *497*, 1–20, doi:10.1016/j.memsci.2015.08.060.

21. Yuan, J.; Mecerreyes, D.; Antonietti, M. Poly(Ionic Liquid)s: An Update. *Prog. Polym. Sci.* **2013**, *38*, 1009–1036,

doi:10.1016/j.progpolymsci.2013.04.002.

22. Malik, M.A.; Hashim, M.A.; Nabi, F. Ionic Liquids in Supported Liquid Membrane Technology. *Chem. Eng. J.* **2011**, *171*, 242–254, doi:10.1016/j.cej.2011.03.041.

23. Wang, S.; Yi, M.; Shen, Z.; Zhang, X.; Ma, S. Adding Ethanol Can Effectively Enhance the Graphene Concentration in Water-Surfactant Solutions. *RSC Adv.* **2014**, *4*, 25374–25378, doi:10.1039/c4ra03345k.

24. Giernoth, R. Task-Specific Ionic Liquids. *Angew. Chemie - Int. Ed.* **2010**, *49*, 2834–2839, doi:10.1002/anie.200905981.

25. Scovazzo, P. Determination of the Upper Limits, Benchmarks, and Critical Properties for Gas Separations Using Stabilized Room Temperature Ionic Liquid Membranes (SILMs) for the Purpose of Guiding Future Research. *J. Memb. Sci.* **2009**, *343*, 199–211, doi:10.1016/j.memsci.2009.07.028.

26. Myers, C.; Pennline, H.; Luebke, D.; Ilconich, J.; Dixon, J.N.K.; Maginn, E.J.; Brennecke, J.F. High Temperature Separation of Carbon Dioxide/Hydrogen Mixtures Using Facilitated Supported Ionic Liquid Membranes. *J. Memb. Sci.* **2008**, *322*, 28–31, doi:10.1016/j.memsci.2008.04.062.

27. Gutowski, K.E.; Maginn, E.J. Amine-Functionalized Task-Specific Ionic Liquids: A Mechanistic Explanation for the Dramatic Increase in Viscosity upon Complexation with CO2 from Molecular Simulation. *J. Am. Chem. Soc.* **2008**, *130*, 14690–14704, doi:10.1021/ja804654b.

28. Yuan, J.; Antonietti, M. Poly(Ionic Liquid)s: Polymers Expanding Classical Property Profiles. *Polymer (Guildf).* **2011**, *52*, 1469–1482, doi:10.1016/j.polymer.2011.01.043.

29. Mecerreyes, D. Polymeric Ionic Liquids: Broadening the Properties and Applications of Polyelectrolytes. *Prog. Polym. Sci.* **2011**, *36*, 1629–1648, doi:10.1016/j.progpolymsci.2011.05.007.

30. Shaligram, S. V.; Wadgaonkar, P.P.; Kharul, U.K. Polybenzimidazole-Based Polymeric Ionic Liquids (PILs): Effects of “substitution Asymmetry” on CO2 Permeation Properties. *J. Memb. Sci.* **2015**, *493*, 403–413, doi:10.1016/j.memsci.2015.07.020.

31. Gu, Y.; Lodge, T.P. Synthesis and Gas Separation Performance of Triblock Copolymer Ion Gels with a Polymerized Ionic Liquid Mid-Block. *Macromolecules* **2011**, *44*, 1732–1736, doi:10.1021/ma2001838.

32. Adzima, B.J.; Venna, S.R.; Klara, S.S.; He, H.; Zhong, M.; Luebke, D.R.; Mauter, M.S.; Matyjaszewski, K.; Nulwala, H.B. Modular Polymerized Ionic Liquid Block Copolymer Membranes for CO 2/N2 Separation. *J. Mater. Chem. A* **2014**, *2*, 7967–7972, doi:10.1039/c4ta00661e.

33. Nguyen, P.T.; Wiesenauer, E.F.; Gin, D.L.; Noble, R.D. Effect of Composition and Nanostructure on CO2/N2 Transport Properties of Supported Alkyl-Imidazolium Block Copolymer Membranes. *J. Memb. Sci.* **2013**, *430*, 312–320, doi:10.1016/j.memsci.2012.12.016.

34. Ansaloni, L.; Nykaza, J.R.; Ye, Y.; Elabd, Y.A.; Giacinti Baschetti, M. Influence of Water Vapor on the Gas Permeability of Polymerized Ionic Liquids Membranes. *J. Memb. Sci.* **2015**, *487*, 199–208, doi:10.1016/j.memsci.2015.03.065.

35. Bara, J.E.; Gabriel, C.J.; Hatakeyama, E.S.; Carlisle, T.K.; Lessmann, S.; Noble, R.D.; Gin, D.L. Improving CO2 Selectivity in Polymerized Room-Temperature Ionic Liquid Gas Separation Membranes through Incorporation of Polar Substituents. *J. Memb. Sci.* **2008**, *321*, 3–7, doi:10.1016/j.memsci.2007.12.033.

36. Zhang, B.; Hoagland, D.A.; Su, Z. Ionic Liquids as Plasticizers for Polyelectrolyte Complexes. *J. Phys. Chem. B* **2015**, *119*, 3603–3607, doi:10.1021/jp5128354.

37. Bara, J.E.; Gin, D.L.; Noble, R.D. Effect of Anion on Gas Separation Performance of Polymer-Room-Temperature Ionic Liquid Composite Membranes. *Ind. Eng. Chem. Res.* **2008**, *47*, 9919–9924, doi:10.1021/ie801019x.

38. Zhou, J.; Mok, M.M.; Cowan, M.G.; Mcdanel, W.M.; Carlisle, T.K.; Gin, D.L.; Noble, R.D. High-Permeance Room-Temperature Ionic-Liquid-Based Membranes for CO 2 / N 2 Separation. **2014**, 53–56.

39. Voss, B.A.; Bara, J.E.; Gin, D.L.; Noble, R.D. Physically Gelled Ionic Liquids: Solid Membrane Materials with Liquidlike CO 2 Gas Transport. *Chem. Mater.* **2009**, *21*, 3027–3029, doi:10.1021/cm900726p.

40. Nguyen, P.T.; Voss, B.A.; Wiesenauer, E.F.; Gin, D.L.; Noble, R.D. Physically Gelled Room-Temperature Ionic Liquid-Based Composite Membranes for CO2/N2 Separation: Effect of Composition and Thickness on Membrane Properties and Performance. *Ind. Eng. Chem. Res.* **2013**, *52*, 8812–8821, doi:10.1021/ie302352r.

41. Uchytil, P.; Schauer, J.; Petrychkovych, R.; Setnickova, K.; Suen, S.Y. Ionic

Liquid Membranes for Carbon Dioxide-Methane Separation. *J. Memb. Sci.* **2011**, *383*, 262–271, doi:10.1016/j.memsci.2011.08.061.

42. Alessandro Triolo, Olga Russina,Hans-Jurgen Bleif, E.D.C. Nanoscale Segregation in Room Temperature Ionic Liquids. *J.Phys.Chem.B* **2007**, *111*, 4641–4644, doi:https://doi.org/10.1021/jp067705t.

43. Abdelrasoul, A.; Doan, H.; Lohi, A.; Cheng, C.H. Morphology Control of Polysulfone Membranes in Filtration Processes: A Critical Review. *ChemBioEng Rev.* **2015**, *2*, 22–43, doi:10.1002/cben.201400030.

44. Salahshoori, I.; Nasirian, D.; Rashidi, N.; Hossain, M.K.; Hatami, A.; Hassanzadeganroudsari, M. *The Effect of Silica Nanoparticles on Polysulfone–Polyethylene Glycol (PSF/PEG) Composite Membrane on Gas Separation and Rheological Properties of Nanocomposites*; Springer Berlin Heidelberg, 2021; Vol. 78; ISBN 0123456789.

45. Farrokhara, M.; Dorosti, F. New High Permeable Polysulfone/Ionic Liquid Membrane for Gas Separation. *Chinese J. Chem. Eng.* **2020**, *28*, 2301–2311, doi:10.1016/j.cjche.2020.04.002.

46. Almansour, F.; Alberto, M.; Bhavsar, R.S.; Fan, X.; Budd, P.M.; Gorgojo, P. Recovery of Free Volume in PIM-1 Membranes through Alcohol Vapor Treatment. *Front. Chem. Sci. Eng.* **2021**, *15*, 872–881, doi:10.1007/s11705-020-2001-2.

47. Budd, P.M. *Polymers of Intrinsic Microporosity and Their Potential in Process Intensification*; Elsevier Inc., 2019; ISBN 9780128146828.

48. Wang, S.; Shi, K.; Tripathi, A.; Chakraborty, U.; Parsons, G.N.; Khan, S.A. Designing Intrinsically Microporous Polymer (PIM-1) Micro Fi Bers with Tunable Morphology and Porosity via Controlling Solvent / Nonsolvent / Polymer Interactions. **2020**, doi:10.1021/acsapm.0c00386.

49. Tamaddondar, M.; Foster, A.B.; Carta, M.; Gorgojo, P.; Mckeown, N.B.; Budd, P.M. Mitigation of Physical Aging with Mixed Matrix Membranes Based on Cross-Linked PIM - 1 Fillers and PIM - 1. **2020**, doi:10.1021/acsami.0c13838.

50. Overview on Porous Inorganic Membranes for Gas Separation. **2017**, doi:10.13140/RG.2.2.35571.53287.

51. Kamble, A.R.; Patel, C.M.; Murthy, Z.V.P. A Review on the Recent Advances in Mixed Matrix Membranes for Gas Separation Processes. *Renew. Sustain. Energy Rev.* **2021**, *145*, 111062,

doi:10.1016/j.rser.2021.111062.

52. Ahmad, M.Z.; Pelletier, H.; Martin-Gil, V.; Castro-Muñoz, R.; Fila, V. Chemical Crosslinking of 6FDA-ODA and 6FDA-ODA:DABA for Improved CO2/CH4 Separation. *Membranes (Basel).* **2018**, *8*, doi:10.3390/membranes8030067.

53. Nematollahi, M.H.; Dehaghani, A.H.S.; Pirouzfar, V.; Akhondi, E. Mixed Matrix Membranes Comprising PMP Polymer with Dispersed Alumina Nanoparticle Fillers to Separate CO2/N2. *Macromol. Res.* **2016**, *24*, 782–792, doi:10.1007/s13233-016-4113-6.

54. Newton Augustus, E.; Nimibofa, A.; Azibaola Kesiye, I.; Donbebe, W. Metal-Organic Frameworks as Novel Adsorbents: A Preview. *Am. J. Environ. Prot.* **2017**, *5*, 61–67, doi:10.12691/env-5-2-5.

55. Nik, O.G.; Chen, X.Y.; Kaliaguine, S. Functionalized Metal Organic Framework-Polyimide Mixed Matrix Membranes for CO 2/CH 4 Separation. *J. Memb. Sci.* **2012**, *413–414*, 48–61, doi:10.1016/j.memsci.2012.04.003.

56. Bi, X.; Zhang, Y.; Zhang, F.; Zhang, S.; Wang, Z.; Jin, J. MOF Nanosheet-Based Mixed Matrix Membranes with Metal-Organic Coordination Interfacial Interaction for Gas Separation. *ACS Appl. Mater. Interfaces* **2020**, *12*, 49101–49110, doi:10.1021/acsami.0c14639.

57. Van der Bruggen, B. The Separation Power of Nanotubes in Membranes: A Review. *ISRN Nanotechnol.* **2012**, *2012*, 1–17, doi:10.5402/2012/693485.

58. Rao, R.; Pint, C.L.; Islam, A.E.; Weatherup, R.S.; Hofmann, S.; Meshot, E.R.; Wu, F.; Zhou, C.; Dee, N.; Amama, P.B.; et al. Carbon Nanotubes and Related Nanomaterials: Critical Advances and Challenges for Synthesis toward Mainstream Commercial Applications. *ACS Nano* **2018**, *12*, 11756–11784, doi:10.1021/acsnano.8b06511.

59. Ahmad, N.N.R.; Leo, C.P.; Mohammad, A.W. Enhancement on the CO2 Separation Performance of Mixed Matrix Membrane Using Ionic Liquid. *Mater. Lett.* **2021**, *304*, 130736, doi:10.1016/j.matlet.2021.130736.

60. Kamble, A.R.; Patel, C.M.; Murthy, Z.V.P. A Review on the Recent Advances in Mixed Matrix Membranes for Gas Separation Processes. *Renew. Sustain. Energy Rev.* 2021, *145*.

61. Skoulidas, A.I.; Ackerman, D.M.; Johnson, J.K.; Sholl, D.S. Rapid Transport of Gases in Carbon Nanotubes. *Phys. Rev. Lett.* **2002**, *89*, 13–16, doi:10.1103/PhysRevLett.89.185901.

62. Kim, S.; Pechar, T.W.; Marand, E. Poly(Imide Siloxane) and Carbon Nanotube Mixed Matrix Membranes for Gas Separation. *Desalination* **2006**, *192*, 330–339, doi:10.1016/j.desal.2005.03.098.

63. Khan, M.M.; Filiz, V.; Bengtson, G.; Shishatskiy, S.; Rahman, M.; Abetz, V. Erratum to: Functionalized Carbon Nanotubes Mixed Matrix Membranes of Polymers of Intrinsic Microporosity for Gas Separation. *Nanoscale Res. Lett.* **2014**, *9*, 1–12, doi:10.1186/1556-276X-9-698.

64. Jiang, L.; Meng, Y.; Tu, S.; Zhao, Y.; Cui, Q.; Zhang, W.; Yu, H.; Hou, X. Graphene Oxide/Single-Walled Carbon Nanotube Membranes for CO2 and N2 Separation from Blast Furnace Gas. *J. Nanomater.* **2020**, *2020*, doi:10.1155/2020/7140182.

65. Nabais, A.R.; Ahmed, S.; Younis, M.; Zhou, J.X.; Pereira, J.R.; Freitas, F.; Mecerreyes, D.; Crespo, J.G.; Huang, M.H.; Neves, L.A.; et al. Mixed Matrix Membranes Based on Ionic Liquids and Porous Organic Polymers for Selective CO2 Separation. *J. Memb. Sci.* **2022**, *660*, doi:10.1016/j.memsci.2022.120841.

66. Geim, A.K.; Novoselov, K.S. The Rise of Graphene. *Nanosci. Technol. A Collect. Rev. from Nat. Journals* **2009**, 11–19, doi:10.1142/9789814287005_0002.

67. Randviir, E.P.; Brownson, D.A.C.; Banks, C.E. A Decade of Graphene Research: Production, Applications and Outlook. *Mater. Today* **2014**, *17*, 426–432, doi:10.1016/j.mattod.2014.06.001.

68. Clancy, A.J.; Bayazit, M.K.; Hodge, S.A.; Skipper, N.T.; Howard, C.A.; Shaffer, M.S.P. Charged Carbon Nanomaterials: Redox Chemistries of Fullerenes, Carbon Nanotubes, and Graphenes. *Chem. Rev.* **2018**, *118*, 7363–7408, doi:10.1021/acs.chemrev.8b00128.

69. Bai, R.G.; Muthoosamy, K.; Manickam, S.; Hilal-Alnaqbi, A. Graphene-Based 3D Scaffolds in Tissue Engineering: Fabrication, Applications, and Future Scope in Liver Tissue Engineering. *Int. J. Nanomedicine* **2019**, *14*, 5753–5783, doi:10.2147/IJN.S192779.

70. Gao, W. *Graphene Oxide: Reduction Recipes, Spectroscopy, and Applications*; 2015; ISBN 9783319155005.

71. Dreyer, D.R.; Park, S.; Bielawski, C.W.; Ruoff, R.S. The Chemistry of Graphene Oxide. *Chem. Soc. Rev.* **2010**, *39*, 228–240, doi:10.1039/b917103g.

72. Parvez, K.; Wu, Z.S.; Li, R.; Liu, X.; Graf, R.; Feng, X.; Müllen, K. Exfoliation of Graphite into Graphene in Aqueous Solutions of Inorganic Salts. *J. Am. Chem. Soc.* **2014**, *136*, 6083–6091, doi:10.1021/ja5017156.

73. Yang, G.; Li, L.; Lee, W.B.; Ng, M.C. Structure of Graphene and Its Disorders: A Review. *Sci. Technol. Adv. Mater.* **2018**, *19*, 613–648, doi:10.1080/14686996.2018.1494493.

74. Yoon, H.W.; Lee, T.H.; Doherty, C.M.; Choi, T.H.; Roh, J.S.; Kim, H.W.; Cho, Y.H.; Do, S.H.; Freeman, B.D.; Park, H.B. Origin of CO2-Philic Sorption by Graphene Oxide Layered Nanosheets and Their Derivatives. *J. Phys. Chem. Lett.* **2020**, *11*, 2356–2362, doi:10.1021/acs.jpclett.0c00204.

75. Yousef, S.; Sarwar, Z.; Šereika, J.; Striugas, N.; Krugly, E.; Danilovas, P.P.; Martuzevicius, D. A New Industrial Technology for Mass Production of Graphene/Peba Membranes for CO2/CH4 Selectivity with High Dispersion, Thermal and Mechanical Performance. *Polymers (Basel).* **2020**, *12*, doi:10.3390/POLYM12040831.

76. Zhang, J.; Xin, Q.; Li, X.; Yun, M.; Xu, R.; Wang, S.; Li, Y.; Lin, L.; Ding, X.; Ye, H.; et al. Mixed Matrix Membranes Comprising Aminosilane-Functionalized Graphene Oxide for Enhanced CO2 Separation. *J. Memb. Sci.* **2019**, *570–571*, 343–354, doi:10.1016/j.memsci.2018.10.075.

77. Sainath, K.; Modi, A.; Bellare, J. CO2/CH4 Mixed Gas Separation Using Graphene Oxide Nanosheets Embedded Hollow Fiber Membranes: Evaluating Effect of Filler Concentration on Performance. *Chem. Eng. J. Adv.* **2021**, *5*, 100074, doi:10.1016/j.ceja.2020.100074.

78. Chen, M.; Soyekwo, F.; Zhang, Q.; Hu, C.; Zhu, A.; Liu, Q. Graphene Oxide Nanosheets to Improve Permeability and Selectivity of PIM-1 Membrane for Carbon Dioxide Separation. *J. Ind. Eng. Chem.* **2018**, *63*, 296–302, doi:10.1016/j.jiec.2018.02.030.

79. Althumayri, K.; Harrison, W.J.; Shin, Y.; Gardiner, J.M.; Casiraghi, C.; Budd, P.M.; Bernardo, P.; Clarizia, G.; Jansen, J.C. The Influence of Few-Layer Graphene on the Gas Permeability of the High-Free-Volume Polymer PIM-1. *Philos. Trans. R. Soc. A Math. Phys. Eng. Sci.* **2016**, *374*, doi:10.1098/rsta.2015.0031.

80. Gribble, G.W. Diels-Alder Cycloaddition. In *Indole Ring Synthesis*; 2016; pp. 437–463.

81. Sarkar, S.; Bekyarova, E.; Niyogi, S.; Haddon, R.C. Diels-Alder Chemistry of Graphite and Graphene: Graphene as Diene and Dienophile. *J. Am. Chem.*

Soc. **2011**, *133*, 3324–3327, doi:10.1021/ja200118b.

82. Sarkar, S.; Bekyarova, E.; Haddon, R.C. Chemistry at the Dirac Point: Diels-Alder Reactivity of Graphene. *Acc. Chem. Res.* **2012**, *45*, 673–682, doi:10.1021/ar200302g.

83. Denis, P.A. Organic Chemistry of Graphene: The Diels-Alder Reaction. *Chem. - A Eur. J.* **2013**, *19*, 15719–15725, doi:10.1002/chem.201302622.

84. Martis, A.; Fontana, M.; Serrapede, M.; Bianco, S.; Chiodoni, A.; Pirri, C.F.; Bocchini, S. Production of Graphene Stably Dispersible in Ethanol by Microwave Reaction. *Colloids and Interfaces* **2022**, *6*, doi:10.3390/colloids6040075.

85. Lotya, M.; Hernandez, Y.; King, P.J.; Smith, R.J.; Nicolosi, V.; Karlsson, L.S.; Blighe, F.M.; De, S.; Zhiming, W.; McGovern, I.T.; et al. Liquid Phase Production of Graphene by Exfoliation of Graphite in Surfactant/Water Solutions. *J. Am. Chem. Soc.* **2009**, *131*, 3611–3620, doi:10.1021/ja807449u.

86. Coleman, J.N. Liquid Exfoliation of Defect-Free Graphene. *Acc. Chem. Res.* **2013**, *46*, 14–22, doi:10.1021/ar300009f.

87. Budd, P.M.; Elabas, E.S.; Ghanem, B.S.; Makhseed, S.; McKeown, N.B.; Msayib, K.J.; Tattershall, C.E.; Wang, D. Solution-Processed, Organophilic Membrane Derived from a Polymer of Intrinsic Microporosity. *Adv. Mater.* **2004**, *16*, 456–459, doi:10.1002/adma.200306053.

88. Ferraro, G.; Astorino, C.; Bartoli, M.; Martis, A.; Lettieri, S.; Pirri, C.F.; Bocchini, S. Ionic Liquids-Polymer of Intrinsic Microporosity (PIMs) Blend Membranes for CO 2 Separation. **2022**.

89. Crank, J. *The Mathematics of Diffusion*; Clarendon Press, Ed.; 1979; ISBN 0198534116, 9780198534112.

90. Dasani, D.; Wang, Y.; Tsotsis, T.T.; Jessen, K. Laboratory-Scale Investigation of Sorption Kinetics of Methane/Ethane Mixtures in Shale. *Ind. Eng. Chem. Res.* **2017**, *56*, 9953–9963, doi:10.1021/acs.iecr.7b02431.

91. Yang, J.; Zhang, X.; Liu, Y.; Tai, Z.; Yan, X.; Ma, J. Understanding Oxygen Bubble-Triggered Exfoliation of Graphite Toward the Low-Defect Graphene. *Adv. Mater. Interfaces* **2021**, *8*, 1–8, doi:10.1002/admi.202001899.

92. Goldstein, M. *Infrared Characteristic Group Frequencies*; 1981; Vol. 5; ISBN 0471852988.

93. Mayo, D. et al. *Course Notes on the Interpretation of Infrared And*; 2003; ISBN 9786468600.

94. Wall, M. The Raman Spectroscopy of Graphene and the Determination of Layer Thickness. *Thermo Sci.* **2011**, 5.

95. Ferrari, A.C.; Meyer, J.C.; Scardaci, V.; Casiraghi, C.; Lazzeri, M.; Mauri, F.; Piscanec, S.; Jiang, D.; Novoselov, K.S.; Roth, S.; et al. Raman Spectrum of Graphene and Graphene Layers. *Phys. Rev. Lett.* **2006**, *97*, 1–4, doi:10.1103/PhysRevLett.97.187401.

96. Hodkiewicz, J.; Scientific, T.F. Characterizing Graphene With. 4.

97. Malard, L.M.; Pimenta, M.A.; Dresselhaus, G.; Dresselhaus, M.S. Raman Spectroscopy in Graphene. *Phys. Rep.* **2009**, *473*, 51–87, doi:10.1016/j.physrep.2009.02.003.

98. TUINSTRA F; KOENIG JL Raman Spectrum of Graphite. *J. Chem. Phys.* **1970**, *53*, 1126–1130, doi:10.1063/1.1674108.

99. Biscoe, J.; Warren, B.E. An X-Ray Study of Carbon Black. *J. Appl. Phys.* **1942**, *13*, 364–371, doi:10.1063/1.1714879.

100. Vacacela Gomez, C.; Guevara, M.; Tene, T.; Villamagua, L.; Usca, G.T.; Maldonado, F.; Tapia, C.; Cataldo, A.; Bellucci, S.; Caputi, L.S. The Liquid Exfoliation of Graphene in Polar Solvents. *Appl. Surf. Sci.* **2021**, *546*, 149046, doi:10.1016/j.apsusc.2021.149046.

101. Muhammad Sajid Hamid Akash & Kanwal Rehman Ultraviolet-Visible (UV-VIS) Spectroscopy. *Essentials Pharm. Anal.* **2019**, 29–56, doi:DOI: 10.1007/978-981-15-1547-7_3.

102. Jianqiang Zhao , Yue Zhang , Lihua Gan, G.W. Experimental and DFT Study of UV–Vis Absorption Spectra of Azobenzene Containing Ester Groups. *Comput. Theor. Chem.* **2021**, *1200*, 113244, doi:https://doi.org/10.1016/j.comptc.2021.113244.

103. Horst Kunkely and Arnd Vogler Absorption and Emission Spectrum of [Zn4O(Acetate)6]. *J. Chem. Soc. Chem. Commun.* **1990**, 1204–1205, doi:DOI https://doi.org/10.1039/C39900001204.

104. Rattana, T.; Chaiyakun, S.; Witit-Anun, N.; Nuntawong, N.; Chindaudom, P.; Oaew, S.; Kedkeaw, C.; Limsuwan, P. Preparation and Characterization of Graphene Oxide Nanosheets. *Procedia Eng.* **2012**, *32*, 759–764, doi:10.1016/j.proeng.2012.02.009.

105. Paredes, J.I.; Villar-Rodil, S.; Martínez-Alonso, A.; Tascón, J.M.D. Graphene Oxide Dispersions in Organic Solvents. *Langmuir* **2008**, *24*, 10560–10564, doi:10.1021/la801744a.

106. Zhang, X.; Coleman, A.C.; Katsonis, N.; Browne, W.R.; Van Wees, B.J.; Feringa, B.L. Dispersion of Graphene in Ethanol Using a Simple Solvent Exchange Method. *Chem. Commun.* **2010**, *46*, 7539–7541, doi:10.1039/c0cc02688c.

107. Hernandez, Y.; Nicolosi, V.; Lotya, M.; Blighe, F.M.; Sun, Z.; De, S.; McGovern, I.T.; Holland, B.; Byrne, M.; Gun'ko, Y.K.; et al. High-Yield Production of Graphene by Liquid-Phase Exfoliation of Graphite. *Nat. Nanotechnol.* **2008**, *3*, 563–568, doi:10.1038/nnano.2008.215.

108. Lotya, M.; King, P.J.; Khan, U.; De, S.; Coleman, J.N. High-Concentration, Surfactant-Stabilized Graphene Dispersions. *ACS Nano* **2010**, *4*, 3155–3162, doi:10.1021/nn1005304.

109. Kumar, A.; Dixit, C.K. Methods for Characterization of Nanoparticles. *Adv. Nanomedicine Deliv. Ther. Nucleic Acids* **2017**, 44–58, doi:10.1016/B978-0-08-100557-6.00003-1.

110. Chen, Y.; Zhang, X.; Yu, P.; Ma, Y. Stable Dispersions of Graphene and Highly Conducting Graphene Films: A New Approach to Creating Colloids of Graphene Monolayers. *Chem. Commun.* **2009**, 4527–4529, doi:10.1039/b907723e.

111. Perumal, S.; Perumal, S.; Lee, H.M.; Cheong, I.W. Dispersion Behavior of Graphene with Different Solvents and Surfactants. **2019**, *20*, 53–60.

112. Wajid, A.S.; Das, S.; Irin, F.; Ahmed, H.S.T.; Shelburne, J.L.; Parviz, D.; Fullerton, R.J.; Jankowski, A.F.; Hedden, R.C.; Green, M.J. Polymer-Stabilized Graphene Dispersions at High Concentrations in Organic Solvents for Composite Production. *Carbon N. Y.* **2012**, *50*, 526–534, doi:10.1016/j.carbon.2011.09.008.

113. Perumal, S.; Lee, H.M.; Cheong, I.W. High-Concentration Graphene Dispersion Stabilized by Block Copolymers in Ethanol. *J. Colloid Interface Sci.* **2017**, *497*, 359–367, doi:10.1016/j.jcis.2017.03.027.

114. Surekha, G.; Krishnaiah, K.V.; Ravi, N.; Padma Suvarna, R. FTIR, Raman and XRD Analysis of Graphene Oxide Films Prepared by Modified Hummers Method. *J. Phys. Conf. Ser.* **2020**, *1495*, doi:10.1088/1742-6596/1495/1/012012.

115. Kinoshita, K. *Carbon: Electrochemical and Physicochemical Properties*; Seiten, Ed.; Sons, Chichester, New York, Brisbane, Toronto, 1988;

116. Wongwilawan, S.; Nguyen, T.S.; Nguyen, T.P.N.; Alhaji, A.; Lim, W.; Hong, Y.; Park, J.S.; Atilhan, M.; Kim, B.J.; Eddaoudi, M.; et al. Non-Solvent Post-Modifications with Volatile Reagents for Remarkably Porous Ketone Functionalized Polymers of Intrinsic Microporosity. *Nat. Commun.* **2023**, *14*, 2096, doi:10.1038/s41467-023-37743-y.

117. Zagho, M.M.; Hassan, M.K.; Khraisheh, M.; Al-Maadeed, M.A.A.; Nazarenko, S. A Review on Recent Advances in CO2 Separation Using Zeolite and Zeolite-like Materials as Adsorbents and Fillers in Mixed Matrix Membranes (MMMs). *Chem. Eng. J. Adv.* **2021**, *6*, 100091, doi:10.1016/j.ceja.2021.100091.

118. Hao, L.; Liao, K.S.; Chung, T.S. Photo-Oxidative PIM-1 Based Mixed Matrix Membranes with Superior Gas Separation Performance. *J. Mater. Chem. A* **2015**, *3*, 17273–17281, doi:10.1039/c5ta03776j.

119. Cha, S.; Ao, M.; Sung, W.; Moon, B.; Ahlström, B.; Johansson, P.; Ouchi, Y.; Kim, D. Structures of Ionic Liquid-Water Mixtures Investigated by IR and NMR Spectroscopy. *Phys. Chem. Chem. Phys.* **2014**, *16*, 9591–9601, doi:10.1039/c4cp00589a.

120. Wang, H.; Zhu, J.; Tan, L.; Zhou, M.; Zhang, S. Encapsulated Ionic Liquids for CO2 Capture. *Mater. Chem. Phys.* **2020**, *251*, 122982, doi:10.1016/j.matchemphys.2020.122982.

121. Besnard, M.; Cabaço, M.I.; Chávez, F.V.; Pinaud, N.; Sebastião, P.J.; Coutinho, J.A.P.; Dantena, Y. On the Spontaneous Carboxylation of 1-Butyl-3-Methylimidazolium Acetate by Carbon Dioxide. *Chem. Commun.* **2012**, *48*, 1245–1247, doi:10.1039/c1cc16702b.

122. Budd, P.M.; Msayib, K.J.; Tattershall, C.E.; Ghanem, B.S.; Reynolds, K.J.; McKeown, N.B.; Fritsch, D. Gas Separation Membranes from Polymers of Intrinsic Microporosity. *J. Memb. Sci.* **2005**, *251*, 263–269, doi:10.1016/j.memsci.2005.01.009.

123. Shiflett, M.B.; Drew, D.W.; Cantini, R.A.; Yokozeki, A. Carbon Dioxide Capture Using Ionic Liquid 1-Butyl-3-Methylimidazolium Acetate. *Energy and Fuels* **2010**, *24*, 5781–5789, doi:10.1021/ef100868a.